DATA ACQUISITION SYSTEM FOR LORENTZ FORCE ELECTRICAL IMPEDANCE TOMOGRAPHY USING MAGNETIC FIELD MEASUREMENTS

A THESIS SUBMITTED TO
THE GRADUATE SCHOOL OF NATURAL AND APPLIED SCIENCES
OF
MIDDLE EAST TECHNICAL UNIVERSITY

BY
KEIVAN KABOUTARI

IN PARTIAL FULFILLMENT OF THE REQUIREMENTS
FOR
THE DEGREE OF MASTER OF SCIENCE
IN
ELECTRICAL AND ELECTRONICS ENGINEERING

FEBRUARY 2017

Approval of the thesis:

DATA ACQUISITION SYSTEM FOR LORENTZ FORCE ELECTRICAL IMPEDANCE TOMOGRAPHY USING MAGNETIC FIELD MEASUREMENTS

submitted by **KEIVAN KABOUTARI** in partial fulfillment of the requirements for the degree of **Master of Science in Electrical and Electronics Engineering Department, Middle East Technical University** by,

Prof. Dr. Gülbin Dural Ünver
Dean, Graduate School of **Natural and Applied Sciences** ________________

Prof. Dr. Tolga Çiloğlu
Head of Department, **Electrical and Electronics Engineering** ________________

Prof. Dr. Nevzat Güneri Gençer
Supervisor, **Electrical and Electronics Eng. Dept., METU** ________________

Examining Committee Members:

Prof. Dr. Murat Eyüboğlu
Electrical and Electronics Eng. Dep., METU ________________

Prof. Dr. Nevzat Güneri Gençer
Electrical and Electronics Eng. Dep., METU ________________

Prof. Dr. Mustafa Kuzuoğlu
Electrical and Electronics Eng. Dep., METU ________________

Assoc. Prof. Dr. Yeşim Serinağaoğlu Doğrusöz
Electrical and Electronics Eng. Dep., METU ________________

Assist. Prof. Dr. Özlem Birgül
Biomedical Eng. Dep., Ankara University ________________

Date: ***17.02.2017***

I hereby declare that all information in this document has been obtained and presented in accordance with academic rules and ethical conduct. I also declare that, as required by these rules and conduct, I have fully cited and referenced all material and results that are not original to this work.

Name, Last Name: KEIVAN KABOUTARI

Signature :

ABSTRACT

DATA ACQUISITION SYSTEM FOR LORENTZ FORCE ELECTRICAL IMPEDANCE TOMOGRAPHY USING MAGNETIC FIELD MEASUREMENTS

Kaboutari, Keivan
M.S., Department of Electrical and Electronics Engineering
Supervisor : Prof. Dr. Nevzat Güneri Gençer

February 2017, 121 pages

Lorentz Force Electrical Impedance Tomography (LFEIT) is a novel imaging modality to image electrical conductivity properties of biological tissues. This modality is recently proposed for early stage diagnosis of cancerous tissues. The main aim of this thesis study is to develop a data acquisition system for LFEIT. Design of contactless receiver sensor, static magnetic field generation (0.56 T is generated by permanent neodymium magnets), amplification of received signals and experimental studies using various phantoms are in the scope of this thesis.

Measurement of the AC magnetic fields generated by the induced Lorentz currents using coil sensors at the resonance frequency is the aim of this thesis. In this study, disk multiple layer receiver coil sensors are used in both numerical simulations and experiments. Physical and electrical characteristics of the sensors are evaluated. A design tool is developed using MATLAB, where the physical properties of the coil sensors are defined as inputs of the design tool. The electrical properties such as DC and AC resistance, resonance frequency and quality factor of the coil sensors are obtained as

outputs. One of the coil sensors designed by this tool is used in the experimental studies. Sensitivity, signal to noise ratio, thermal noise and quality factor of the realized coil are about 392.72 $n\frac{V}{Hz\frac{A}{m}}$, 39.32 dB, 33.83 nV and 29, respectively. Minimum detectable AC magnetic field by the realized coil is about 0.17 pT. A custom made two stage amplifier is designed and utilized in the receiving system. The gain and upper $3dB$ frequency of the cascaded amplifiers are 100 dB and 1.02 MHz frequency, respectively. Pre-stage amplifier's gain, input RMS voltage noise and minimum RMS detectable signal are 52 dB, 5.09 and 7.19 μV. By connecting the realized coil to the pre-stage amplifier, input RMS voltage noise and minimum RMS detectable signal are increased to 6.28 and 8.87 μV. Then, pre-stage amplifier output is about 3.55 mV. Second stage amplifier's gain and minimum RMS detectable signal are 48 dB and 0.84 μV (-121.52 dB), respectively. Note that, the pre-stage amplifier output is greater than the minimum RMS detectable signal of the second stage.

For experimental studies, four phantoms with inhomogeneities in electrical conductivity are developed (70, 800-3000 and 8×10^6 S/m). The prepared phantoms are utilized in the LFEIT experimental system and generated signals are measured by the designed coil sensor. Signals originating from conductivity inhomogeneities reveal the location of inhomogeneities. Acquired signals are also used in order to generate fast LFEIT images of the phantoms.

Keywords: Lorentz Force Electrical Impedance Tomography, Magneto-Acousto Electrical Tomography, Breast cancer detection, Electrical Impedance Tomography, Ultrasound transducer

ÖZ

MANYETIK ALAN ÖLÇÜMLERİ İLE LORENTZ KUVVET ELEKTRİK EMPEDANS TOMOGRAFİSİ İÇİN VERİ TOPLAMA SİSTEMİ

Kaboutari, Keivan
Yüksek Lisans, Elektrik ve Elektronik Mühendisliği Bölümü
Tez Yöneticisi : Prof. Dr. Nevzat Güneri Gençer

Şubat 2017, 121 sayfa

Lorentz Kuvvetleri ile Elektriksel Empedans Tomografisi (LKEET) biyolojik dokuların elektriksel iletkenliklerini görüntülemek için önerilen yeni bir yöntemdir. Bu yöntem, erken evre kanser dokularının tanısı için son zamanlarda önerilmiştir. Bu tezin ana hedefi LKEET için veri toplama sisteminin geliştirilmesidir. Temassız alıcı sensörü geliştirme, statik manyetik alan oluşturma (sabit mıknatıslar ile 0.56 T üretilmiştir), sinyallerin yükseltilmesi ve farklı fantomlarla deneysel çalışmalar yapılması bu tezin kapsamındadır.

Bu tezin amacı rezonans frekansındaki bobin sensörlerini kullanarak endüklenmiş Lorentz akımların meydana getirdiği AC manyetik alanlarının ölçülmesidir. Bu çalışmada, nümerik benzetim ve deneysel çalışmalar için yuvarlak çok katmanlı alıcı bobin sensörleri kullanılmıştır. Sensörlerin fiziksel ve elektriksel özellikleri değerlendirilmiştir. MATLAB kullanılarak giriş parametreleri bobin sensörlerinin fiziksel özellikleri olan bir tasarım aracı geliştirilmiştir. DC ve AC dirençleri, rezonans fre-

kansı ve bobin sensörlerinin nitelik oranı (quality factor) gibi elektriksel özellikler çıkış parametreleridir. Bu tasarım aracı ile tasarlanan bir bobin sensörü deneysel çalışmalarda kullanılmıştır. Bobinin duyarlılık, sinyal gürültü oranı, ısıl gürültü ve nitelik oranı sırasıyla yaklaşık 392.72 $n\frac{V}{Hz\frac{A}{m}}$, 39.32 dB, 33.83 nV ve 29'dur. Bobin ile algılanabilen minimum AC manyetik alanı yaklaşık 0.17 pT'dir. İki aşamalı bir yükselteç geliştirilmiş ve ölçüm sisteminde kullanılmıştır. Kademeli yükseltecin kazancı ve üst bant genişliğinin frekansı sırasıyla 100 dB ve 1.02 MHz'dir. İlk aşama yükseltecin kazancı, giriş RMS voltaj gürültüsü ve algılanabilen minimum RMS sinyali sırasıyla 52 dB, 5.09 ve 7.19 μV'dir. İlk aşama yükselteç bobine bağlandığında giriş RMS voltaj gürültüsü ve algılanabilen minimum RMS sinyali 6.28 ve 8.87 μV değerlerine artmıştır. İlk aşama yükseltecin çıkışı yaklaşık 3.55 mV'dir. İkinci aşama yükseltecin kazancı ve algılabilen minimum RMS sinyali sırasıyla yaklaşık 48 dB ve 0.84 μV (-121.52 dB)'dir. Belirtildiği üzere ilk aşama yükseltecin çıkışı, ikinci aşamanın algılanabilen minimum RMS sinyalinden daha büyüktür.

Deneysel çalışmalar için elektriksel iletkenlik değerleri homojen olmayan dört fantom yapılmıştır (70, 800-3000 ve $8{\times}10^6$ $\frac{S}{m}$). Hazırlanan fantomlar LKEET deneysel sisteminde kullanılmış ve elde edilen sinyaller tasarlanan bobin sensörleri ile ölçülmüştür. Homojen olmayan bölgelerden alınan sinyaller farklı iletkenlikli bölgelerin yerini göstermektedir. Elde edilen sinyaller, fantomların hızlı LKEET görüntülerinin oluşturulması için kullanılmıştır.

Anahtar Kelimeler: Lorentz Kuvvetleri ile Elektriksel Empedans Tomografisi, manyeto akusto elektriksel tomografi, Meme Kanseri Algılama, Elektrik İletkenlik Görüntülemesi, Ultrasonik Dönüştürücü

To the four pillars of my life: God, my spouse, and my parents. Without you, my life would fall apart. I might not know where the life's road will take me, but walking with You, God, through this journey has given me strength. Farnaz, you are everything for me, without your love and understanding, I would not be able to make it. Mom, you have given me so much, thanks for your faith in me, and for teaching me that I should never surrender. Daddy, you always told me to "reach for the stars." I think I got my first one. Thanks for inspiring my love for transportation. We made it...

ACKNOWLEDGMENTS

It is my great pleasure to take this opportunity to thank everyone who made this dissertation possible. There are no proper words to convey my deepest sincere gratitude and respect for my thesis and research advisor Professor Dr. Nevzat Güneri Gençer for his unfailing and invaluable guidance and continuous support, without which I would have not been able to finalize my thesis. I have benefited especially from his constructive comments and invaluable suggestions throughout this thesis. I would also like to thank him for endowing our teamwork at the laboratory with such a kind, devoted and trustworthy family environment. I could not have imagined having a better advisor and mentor for my M.Sc. study.

A special gratitude goes to Dr. Reyhan Zengin who in spite of living different city I never felt her absence here. I sincerely appreciate her dedications and I am forever indebted to her inspiring discussions, suggestions, and unrelenting guidance. My sincere thanks also goes to my friend and colleague Ahmet Önder Tetik, who provided me stimulating discussions, for the sleepless nights we were working together before deadlines, and for all the fun we have had in the last two years. Without his precious support it would not be possible to conduct this research. I would like to thank my friends and colleagues in Brain Research Laboratory at METU, Elyar Ghalichi, Mehmet Soner Gözü, Dr. Azadeh Kamali Tafreshi and Amin Soltani for lending me their invaluable experiences in technical studies.

I would also like to express my deep thanks to my dear friend Hamed Asadi, who blessed me like a very kind brother with his priceless and unforgettable supports throughout all my M.Sc. studies. I never forget how he cheered me up through accomplishing my goals.

Last but not least; I would like to heartfully thank my family for their unconditional trust, patience, and love. I have always felt their generous love and encouragements despite the various difficulties of their own. Without them, I would not have been able to achieve my present academic standing and moreover, I owe all my lifetime achievements to them.

This research was generously supported by Scientific and Technical Research Council of Turkey (TÜBITAK) under the 114E184 (Cost Action BM1309 (EMF-MED)).

TABLE OF CONTENTS

LIST OF TABLES

TABLES

LIST OF FIGURES

FIGURES

LIST OF ABBREVIATIONS

LFEIT	Lorentz Force Electrical Impedance Tomography
US	Ultrasound
FUS	Focused Ultrasound
METU	Middle East Technical University
SNR	Signal to Noise Ratio
BW	Bandwidth
NE	Negative Edge of the coil
PE	Positive Edge of the coil
Len	Length
TN	Numbers of Turns
LN	Numbers of Layers
PF	Packing Factor
WIT	Wire Insulator Thickness
MD	Mean Diameter
WD	Winding Depth
TNL	Turn Number per Layer
WL	Wire Length
CA	Conductor Cross Section Area
SE	Skin Effect
Wd	Wire diameter
Cd	Conductor diameter
TF	Transfer Function
VDF	Voltage Divider Factor
DF	Damping Factor
AF	Amplification Factor
S	Sensitivity
GBWP	Gain Bandwidth Product
RMS	Root Mean Squared
PSD	Power Spectrum Density
CF	Correction Factor
TGC	Time Gain Compensation
MAET	Magneto-Acousto Electrical Tomography

EIT	Electrical Impedance Tomography
MAT-MI	Magneto-Acoustic Tomography with Magnetic Induction
ICEIT	Induced Current Electrical Impedance Tomography
MIT	Magnetic Induction Tomography (MIT)
AET	Acousto-Electric Tomography
SQID	Superconducting Quantum Interference Device

CHAPTER 1

INTRODUCTION

Breast cancer is the most common cancer among women in the world (25 % of all cancers) and it has been ranked fifth among overall cancerous causes of death [4]. Therefore, early stage diagnosis of breast cancer is important for increasing survival rate. Diagnosis of the breast cancer is done by several imaging methods such as mammography, MRI, ultrasound, EIT, MAT-MI, etc. Mammography uses x-rays which is harmful for the biological tissues (invasive method). It is normally used only once in a determined period. Moreover, it is mostly combined with an ultrasound examination for differential diagnosis [5]. MRI is an expensive method for breast cancer diagnosis but nevertheless it is noninvasive. However, MRI is not available everywhere. Ultrasound does not produce a high quality images for soft tissues [6].

Several methods use electrical properties of the biological tissues to produce medical images. Electrical properties of biological tissues are non-linear functions of frequency. In addition, if the frequency of electromagnetic field changes, the interaction between the field and the tissue also changes [7]. In the Electrical Impedance Tomography method (EIT), several equidistantly placed surfaced electrodes are used. Two of them inject current to the tissue, and others measure the differential voltages. However, spatial resolution of this non-invasive method is poor [8]. In the Induced Current Electrical Impedance Tomography (ICEIT) method, induction method is used instead of applying currents to the body. A sinusoidal current is applied to the coil encircling body. Then the resultant voltages due to induced currents (generated by time-varying magnetic field) are measured by using the surface electrodes [9]. In the Magnetic Induction Tomography (MIT) method, transmitter and receiver coils are placed around the body. Eddy currents are induced inside the body by applying electrical currents to the transmitter coils [10–12]. Secondary magnetic flux density is sensed by the receiver coils and used for image reconstruction. However, its spatial resolution is low.

In hybrid methods, advantages of electromagnetic waves (good penetration depth due to their large wavelength) and acoustic imaging methods (provide higher spatial resolution with reasonable penetration depth) are combined. Note that electromagnetic waves and acoustic imaging methods suffer from lower spatial resolution for soft tissues if applied independently. In the Acousto-Electric Tomography (AET) method, ultrasound excitation is added to EIT [13]. Data is collected similar to the EIT but an ultrasound wave is applied to the object while data is acquired. In the Magneto-Acoustic Tomography with Magnetic Induction (MAT-MI) method, body is placed inside the static magnetic field and eddy currents are induced by applying time varying magnetic field using transmitter coils [14]. Interaction between magnetic fields and eddy currents causes Lorentz forces on the conductive body. The acoustic vibrations are sensed by ultrasound transducers placed around the object.

Lorentz Force Electrical Impedance Tomography (LFEIT) is based on the reported results of Hall effect Imaging [15]. In this method, the body is placed inside a strong static magnetic field and is excited by acoustic pressure wave. As a consequence, Lorentz currents are induced inside the body. Induced Lorentz currents generate electric potential and magnetic field distribution which can be used to obtain data from the body (Figure 1.1). Theoretical principles and basic assumptions of LFEIT was presented in [7, 16] and [17]. LFEIT studies using boundary voltage measurements were reported in [15, 18–20] and [21]. Contributions on the theory of LFEIT using magnetic field measurements were reported in [7, 16, 17, 22].

In an experimental study for LFEIT using magnetic field measurements, a simple set up was established and experiments were conducted using a simple phantom [22]. A low amplitude burst sinusoidal signal (5 cycle, 1 MHz) with repetition period of 1 ms was applied to an ultrasound transducer (Olympus A-303-SU) yielding a pressure level of 0.6 MPa in the body. A custom made Neodymium magnet configuration was used to apply a static magnetic field of 0.2 T. A multilayer (70 turns) air coil

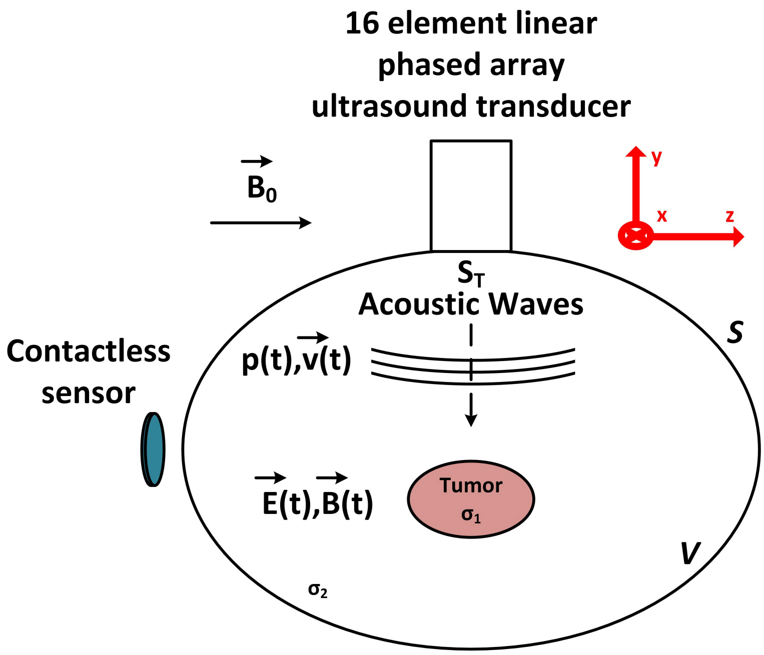

Figure 1.1: Lorentz Force Electrical Impedance Tomography (LFEIT).

sensor of diameter 2 cm was employed for measurements. However, measurements from an oil ($(2-10) \times 10^{-9}$ S/m)-saline water (2-4 S/m) phantom did not show any evidence of LFEIT signals.

In a recent study [17], by increasing the ultrasound pressure strength, images of high conductivity (10-30 S/m) phantoms were presented. Voltage pulses of 80 ns duration, 2 kHz repetition frequency and 1200 V amplitude were applied to the ultrasound transducer (500 kHz). A static field of 0.3 T was applied on the phantoms (salinity gel and graphite powder composition). LFEIT experiments at the center frequency of 500 kHz and a bandwidth of 300 kHz were presented. Two series connected 150 turn coil with 3 cm mean radius and 6 cm distance between coil sensors were employed in the measurements.

In this thesis study, a new experimental system is developed for LFEIT signal measurements using receiver coil sensors. To the author's knowledge, this is the third attempt to observe LFEIT signals using coil sensors. The block diagram of the LFEIT system is shown in Figure 1.2. An ultrasound operating frequency of 1 MHz is chosen for excitation. This is based on two facts: 1) acoustic wave penetration decreases with increasing frequency, 2) there is significant conductivity difference between healthy and cancerous tissue at low frequencies [23]. A new permanent magnet configuration is used to obtain a stronger magnetic field. Instead of a single element ultrasound transducer, a linear phased array (LPA) is used to steer the ultrasound waves. Basic properties of coil sensors is explored and coils are designed to enhance the sensitivity in measurements. Different phantoms are realized to increase the electrical conductivity and signal-to-noise ratio (SNR) in measurements. A two-stage amplifier and a digitizer board (GaGe Oscar 4327 14-bit PCIe) is utilized in the receiver side of the data acquisition system.

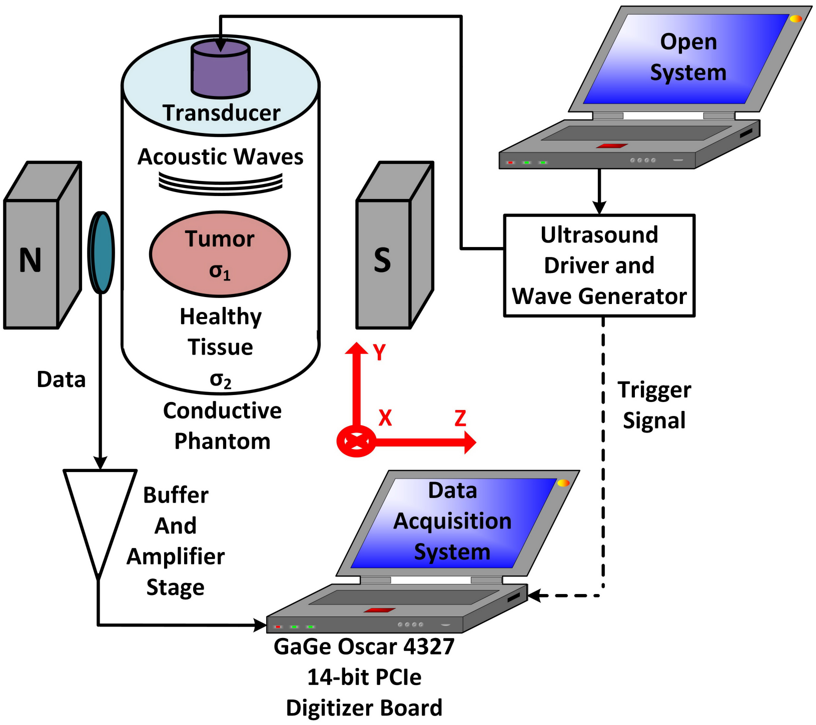

Figure 1.2: Block diagram of LFEIT experimental setup.

1.1 Scope of the Thesis Study

In this thesis study, a data acquisition system will be realized for LFEIT using magnetic measurements. Experiments will be conducted to understand the feasibility of this imaging modality. Therefore, the scope of this thesis can be itemized as follows:

- To design coil sensors for magnetic field measurements.
- To develop a simulation environment for design purposes.
- To develop a calibration set up for the implemented coil sensors.
- To develop a low noise, high gain amplifier for coil sensor.
- To prepare phantoms having inhomogeneous conductivity distributions.
- To develop static magnetic field for LFEIT measurements.
- To conduct experimental studies for LFEIT measurements.

1.2 Thesis Organization

In Chapter 2, design parameters of disk multiple-layer coil sensors are introduced. The physical parameters of the coil are used to define its electrical parameters. Then a coil model is introduced based on these parameters. From the coil model the transfer function, impedance, quality factor, sensitivity, SNR, etc. of the coil are derived.

In Chapter 3, simulation results for different disk multiple-layer coil sensor designs are presented. These simulations are performed in MATLAB and LTspice to estimate the electrical properties.

In Chapter 4, based on the simulations of chapter 3, several disk multiple layer receiver coils are wound. A transmitter coil is used to determine the distance and frequency dependent characteristics of the receiver coil. The simulated and measured results are compared.

In Chapter 5, LFEIT experiments are investigated by four phantoms with inhomogeneities in electrical conductivity. Static magnetic field of 0.56 T is generated by Neodymium permanent magnets. The air gap between these magnets is 6.4 cm. At the middle plane of the air gap, the profile of static magnetic field is measured. Real time imaging of measured LFEIT signals are obtained and compared to the B-scan ultrasound image.

CHAPTER 2

COIL SENSOR DESIGN PARAMETERS

Magnetic sensors are devices that measure the magnetic field variations in a medium. Several types of sensors measure the strength of AC magnetic fields. By considering the wavelength of the LFEIT experiments, using even a monopole antenna is not possible. Therefore, other sensors that measure the low strength magnetic field variations should be utilized in the measurements. The superconducting quantum interference device (SQUID) that has the highest sensitivity among the magnetometer sensors, can be utilized in the LFEIT experiments. However, they are low temperature sensors and are more expensive than other types of magnetometer sensors [24,25]. Other low cost high preformance sensors are search coils (induction coils) [26]. Sensitivity and resolution of search coils are adjustable and they can be utilized in various applications. Working principle of induction coils is based on Faraday's law of induction [27,28]. Two types of induction coils are core-less (air-cored) and cored (ferromagnetic cored) coils. Linearity factor, sensor's output performance and homogeneity of the measured magnetic fields are defected if a core is employed in the coil sensors. Typically, cores in the induction coils are a source for noise, even though they increase the measurement sensitivity.

Induction coils are classified by their geometry and shapes. Typical induction coil sensors are rectangular multiple layer coils, disk multiple layer coils, flat spiral coils (spiral planar coils) and etc. Sensitivity of induction coils, especially when their size is small, are quite low. Due to disadvantages of cored coils, air-cored induction coils are selected to be implemented in the LFEIT experiments. Among the air-cored sensors, disk multiple layer coils have better performance in comparison with the rectangular multiple layer and spiral planar coils. Consequently, in this thesis study properties of air-cored disk multiple layer coils are investigated.

The aim of this chapter is to formulate and define a procedure to design disk multiple layer coil sensors. The proposed coil sensors should be able to measure low amplitude LFEIT signals at 1 MHz. As a first step, physical properties of the disk multiple layer coils will be defined. Next, their electrical characteristic will be formulated by using the specified physical properties.

2.1 Design of Disk Multiple Layer Coil Sensors

In the LFEIT experiments, linearity and sensitivity of the contactless sensors are two important factors. As mentioned previously, the LFEIT experiments are done at 1 MHz frequency. In addition, as mentioned before, a strong static magnetic field is required for these experiments. Therefore, ferromagnetic cores can not be used in the sensor coils to increase sensitivity of the receiver coils. Consequently, air-cored induction coil sensors (search coil sensors) are chosen for magnetic field measurements.

There are several types of air cored coils such as flat spiral, rectangular multilayer, disk multiple layer coils. By investigating comparing their performance, like sensitivity and SNR, disk multiple layer coil sensors are selected. Coil sensor frequency can be adjusted by a tuning circuit (subsection 2.1.12). The measured signals are then filtered and amplified. Finally, the amplified signals will be saved by a data acquisition card (Figure 2.1).

2.1.1 Geometric Parameters

In this subsection, parameters of disk multiple layer coil sensors (packing factor, wire insulator thickness, mean diameter, winding depth and etc.) are introduced.

Packing Factor (PF):

Two different winding types for disk multiple layer coil sensors are presented in Fig-

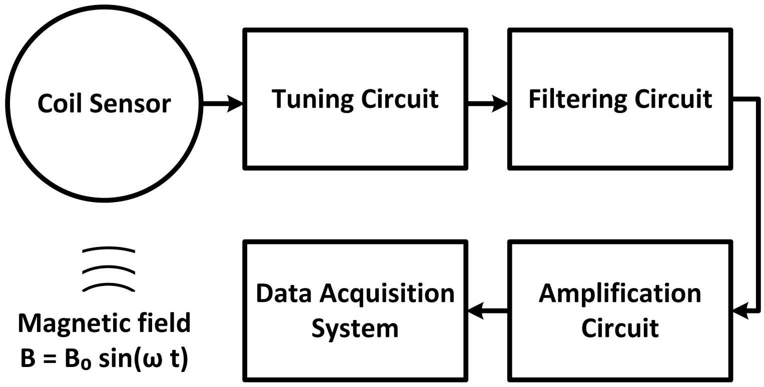

Figure 2.1: Block diagram of the LFEIT receiver system.

ure 2.2. Packing factor PF determines the ratio of coil surface occupied by wound wire [27].

Wire Insulator Thickness (m):

The material and thickness of the wire insulator effect the coil sensor's capacitance [27]:

$$WIT = \frac{Wd - Cd}{2} \tag{2.1}$$

where Wd and Cd are wire and conductor diameters (m) of coil sensor respectively.

Mean Diameter (m):

Mean diameter MD is the average of the outer and inner diameters of the disk multiple layer sensor coil [26]:

$$MD = \frac{D + D_i}{2} \tag{2.2}$$

where D and D_i are outer and inner diameter (m) of the coil sensor respectively.

Winding (Coil) Depth (m):

Winding depth WD is half of coil sensor area that is wound by the wire [26]:

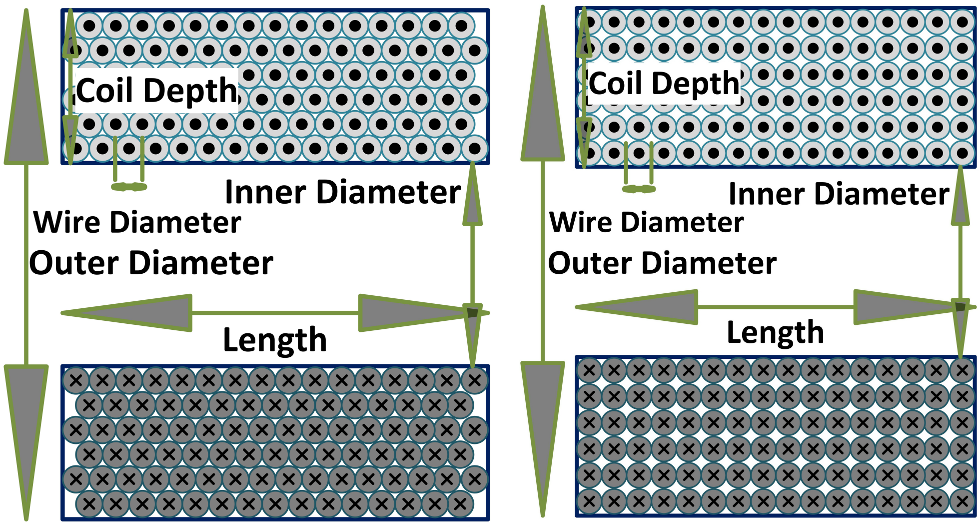

Figure 2.2: Two different winding methods of disk multiple layer coils. (a) Disk multiple layer coil with $\frac{\pi}{2\sqrt{3}}$ packing factor. (b) Disk multiple layer coil with $\frac{\pi}{4}$ packing factor.

$$WD = \frac{D - D_i}{2} \tag{2.3}$$

Turn Number:

Turn number TN represents the number of wire turns which are wound on the coil sensor [26]:

$$TN = PF \cdot Len \cdot \frac{WD}{\frac{\pi}{4} Wd^2} \tag{2.4}$$

where Len (m) is the length of coil sensor.

Layer Number:

Number of layers LN is determined by considering dimensions of the coil sensor. Number of layers is expressed as:

$$LN = \frac{\pi}{4}\frac{TN}{PF}\frac{Wd}{Len} \tag{2.5}$$

Turn Number per Layer:

Turn number per layer TNL represents the number of turns over each layer for multiple layer coil sensor:

$$TNL = \frac{TN}{LN} \tag{2.6}$$

Wire Length (m):

In order to evaluate some electrical properties of the coil sensor, calculation of the wire length WL used in coil winding is important:

$$WL = \pi MD \cdot TN \tag{2.7}$$

Conductor Cross Section Area (m^2):

Conductor cross section area CA is another important factor to calculate coil sensor's DC resistance. It is expressed as:

$$CA = \pi\left(\frac{Cd}{2}\right)^2 \tag{2.8}$$

2.1.2 Electrical Parameters

In this section, electrical parameters (capacitance, inductance, and AC resistance, etc.) are determined by physical properties of the coil sensor are introduced.

Capacitance:

Disk multiple layer coil sensor composed of insulated wires acts like capacitance at high frequencies. This lumped capacitance presents adjacent turn to turn and layer to layer capacitance of the coil sensor. Lumped self-capacitance due to magnetic stray effect in the winding and voltage distribution within the coil, changes with frequency. In most cases, because of negligible changes of lumped capacitance, a constant capacitance can be assumed. Normally, the smallest possible value is desired (in order to set self resonance frequency of the coil at high frequencies). In addition, dielectric losses are kept minimum by this way. Capacitance of the coils are dependent on the physical dimensions and internal winding properties. Thus, estimating the coil capacitance is difficult and is not accurate. The capacitance is calculated by two methods:

- Capacitance (pF) [27]:

$$C = \frac{0.37\epsilon_r MD}{2WIT}\frac{Len}{LN} \tag{2.9}$$

  where ϵ_r is the relative permittivity of the insulator. All length dimensions are in (cm).

- Capacitance (F) of a single layer core-less coil with TN turn numbers is [29]:

$$C = \frac{C_{tt}}{TN - 1} \tag{2.10}$$

  where C_{tt} is calculated by:

$$C_{tt} = \epsilon_0 TL \int_0^{\frac{\pi}{6}} \frac{d\theta}{1 + \frac{1}{\epsilon_r}\ln(\frac{Wd}{Cd}) - \cos\theta} \tag{2.11}$$

  or:

$$C_{tt} = \epsilon_0 TL \left(\frac{\epsilon_r \theta^\star}{\ln(\frac{Wd}{Cd})} + \cot(\frac{\theta^\star}{2}) - \cot(\frac{\pi}{12}) \right) \tag{2.12}$$

$$\theta^\star = \sin^{-1}(1 - \frac{1}{\epsilon_r}\ln(\frac{Wd}{Cd})) \tag{2.13}$$

  TL, Wd and Cd are the turn length, wire and conductor diameter respectively. For a disk multiple layer coil without a core, equation (2.10) becomes:

$$C = \begin{cases} 1.618C_{tt}, & \text{with two layers that TN>10} \\ 0.5733C_{tt}, & \text{with three layers that TN>10} \end{cases}$$

DC Resistance (Ω):

DC resistance R_{DC} is equal to [26]:

$$R_{DC} = \rho \frac{WL}{CA} \tag{2.14}$$

where ρ (Ωm) is the resistivity of the conductor (material dependent) at reference temperature ($T = T_0 = 293.15°K$). R_{DC} of the coil regarding the geometry of the coil sensor can be determined as:

$$R_{DC} = \frac{4}{\pi} \rho PF \frac{Len}{Wd^2 \cdot Cd^2} (D - D_i)(D + D_i) \tag{2.15}$$

where resistivity of a conductor is temperature dependent:

$$\rho = \rho_0 (1 + \beta (T - T_0)) \tag{2.16}$$

ρ_0 is the resistivity of the conductor at T_0 ($°K$) and β ($\frac{1}{°K}$) is the resistance temperature coefficient, respectively. From equation 2.16, resistance will increase with temperature. Therefore, equation 2.15 at temperature T ($°K$) becomes:

$$R_{DC} = \frac{4}{\pi} \rho_0 (1 + \beta (T - T_0)) PF \frac{Len}{Wd^2 \cdot Cd^2} (D^2 - D_i^2) \tag{2.17}$$

To simplify equation 2.17, Cd is assumed approximately equal to Wd:

$$R_{DC} \approx \frac{4}{\pi} \rho_0 (1 + \beta (T - T_0)) PF \frac{Len}{Wd^4} (D^2 - D_i^2) \tag{2.18}$$

The resistance temperature coefficient of aluminium and copper are 15.71 and 14.74 $\mu/°K$ [30], respectively.

Skin Effect:

Tendency of the AC current to be distributed within a conductor such that the major portion of current density passes near the surface is called skin effect. Skin and proximity effects increase winding resistance approximately with $\sqrt{f}$ and decrease inductance of the coil slightly with f [31, 32]. Skin effect SE is expressed as:

$$SE = \sqrt{\frac{\rho}{\pi \mu_0 \mu_r f}} \tag{2.19}$$

where μ_0, μ_r and f are the free space permeability (H/m), relative permeability ($\mu_r \approx 0.999994$) and frequency (Hz) respectively.

AC Resistance (Ω):

This type of resistance is produced when the coil sensor with specific resonance frequency is located inside a dynamic magnetic field. Disk multiple layer coil sensor's layer number is an important factor for the estimation of AC resistance.

- Disk Multiple Layer Coils with less than Three Number of Layers

  The experiments show that if the winding contains less than three layers, the method proposed by Dowell predicts the AC resistance accurately [33]:

$$R_{AC} = R_{DC}(CF \cdot [G_1(CF) + \frac{2}{3}(LN^2 - 1)(G_1(CF) - 2G_2(CF))]) \quad (2.20)$$

  where CF is the correction factor of the disk multiple layer coil sensor:

$$CF = \frac{\sqrt{\pi} \cdot Cd}{2 \cdot SE}$$

  $G_1(CF)$ and $G_2(CF)$ are equations which express the geometry of conducting coil:

$$G_1(CF) = \frac{\sinh(2 \cdot CF) + \sin(2 \cdot CF)}{\cosh(2 \cdot CF) - \cos(2 \cdot CF)}$$

$$G_2(CF) = \frac{\sinh(CF) \cdot \cos(CF) + \cosh(CF) \cdot \sin(CF)}{\cosh(2 \cdot CF) - \cos(2 \cdot CF)}$$

- Disk Multiple Layer Coils with more than Three Number of Layers

  For the windings that contain more than three layers, the method which is proposed by Jan A. Ferreira predicts the AC resistance accurately [34]. This method uses Kelvin's functions [35] which are special case of Bessel's functions.

$$
\begin{aligned}
R_{AC} = R_{DC}\frac{\gamma}{2}(\frac{ber(\gamma)bei'(\gamma) - bei(\gamma)ber'(\gamma)}{ber'^2(\gamma) + bei'^2(\gamma)} \\
-2\pi\eta^2(\frac{4(LN^2-1)}{3} + 1)\frac{ber_2(\gamma)ber'(\gamma) + bei_2(\gamma)bei'(\gamma)}{ber^2(\gamma) + bei^(\gamma)})
\end{aligned}
\tag{2.21}
$$

$$
\gamma = \frac{Cd}{\sqrt{2} \cdot SE}
$$

η is the porosity factor:

$$
\eta = \frac{\sqrt{\pi}}{2}\frac{Cd}{Wd} \tag{2.22}
$$

Inductance (μH):

The inductance of the disk multiple layer induction coil sensor is calculated by two different methods.

- Inductance of the coil sensor approximately is equal to [36]:

$$
L = \frac{0.8(\frac{MD}{2})^2 TN^2}{3MD + 9Len + 10WD} \tag{2.23}
$$

  where all length dimensions are in inches.

- Overall inductance of the coil sensor is equal to the sum of self and mutual inductance [29]:

$$
L = \sum_{i=1}^{LN}\sum_{j=1}^{TNL}\sum_{h=1}^{LN}\sum_{k=1}^{TNL} M_{(i,j)(h,k)} \tag{2.24}
$$

  where (i, j) and (h, k) present j_{th} turn of the i_{th} layer and k_{th} turn of the h_{th} layer of the coil sensor, respectively. LN and TNL present number of layers and number of turns per layer, respectively.

  – Self Inductance:

    In this case, i is equal to h and j is equal to k.

$$
M_{(i,j)(h,k)} = \mu_0 R_i(\ln(\frac{16R_i}{Cd}) - \frac{7}{4}) \tag{2.25}
$$

    where Cd and R_i are the conductor diameter and turn radius that is in the i_{th} layer.

– Mutual Inductance:

In this case, $i \neq h$ and $j \neq k$.

$$M_{(i,j)(h,k)} = \mu_0 \sqrt{R_i R_h}((\frac{2}{c} - c)I_1(c) - \frac{2}{c}I_2(c)) \tag{2.26}$$

where I_1 and I_2 are Legendre's elliptic integrals of first and second kinds, respectively. However, R_i and R_h present the turn radius that are in the i_{th} and j_{th} layers, respectively.

$$I_1(c) = \int_0^{\frac{\pi}{2}} \frac{d\psi}{\sqrt{1 - c^2 sin^2\psi}} \tag{2.27}$$

$$I_2(c) = \int_0^{\frac{\pi}{2}} \sqrt{1 - c^2 sin^2\psi} d\psi \tag{2.28}$$

$$c^2 = \frac{4R_i R_h}{d_{j,k}^2 + (R_i + R_h)^2} \tag{2.29}$$

where $d_{j,k}$ is the distance between planes that are contain j_{th} and k_{th} turn, respectively.

Thermal Noise (V):

Thermal noise V_{Th} is expressed as [26]:

$$V_{Th} = \sqrt{4k_B \cdot T \cdot R_{DC} \cdot BW} \tag{2.30}$$

where k_B, T and BW are the Boltzmann constant, temperature ($^\circ K$) and bandwidth (Hz), respectively.

2.1.3 Induced Voltage (V):

The induced voltage on the coil sensor is proportional to the rate of change of flux with respect to time [27]:

$$V = -TN\frac{d\Phi}{dt} \tag{2.31}$$

Φ is the magnetic flux through the cross section of the coil ($\Phi = AB\cos(\alpha)$ where $B = B_0\cos(\omega t)$). α is the angle between the magnetic field and coil axis. From equation (2.31), one can obtain:

$$V = -TN \cdot A\cos(\alpha)\frac{dB}{dt} = TN \cdot A \cdot B_0\omega\cos(\alpha)\sin(\omega_0 t) \tag{2.32}$$

$$A = \pi\left(\frac{MD}{2}\right)^2$$

$$V_{Ind.} = \frac{\pi^2}{2}TN \cdot MD^2 \cdot fB_0\cos(\alpha)\sin(\omega t) \tag{2.33}$$

2.1.4 Electrical Model:

To investigate the behaviour of disk multiple layer coil theoretically, it is necessary to find the resonance frequency and transfer function of the coil sensor. Figure 2.3 shows an electrical model for disk multiple layer coil sensor [26, 27, 33].

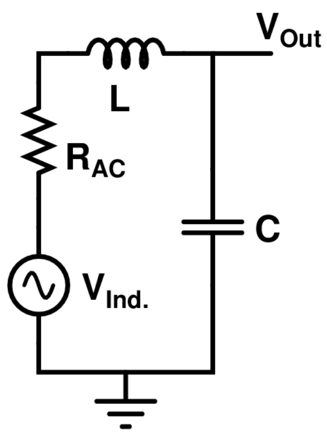

Figure 2.3: Electrical disk multiple layer receiver coil sensor model.

$V_{Ind.}$, R_{AC}, L, C and V_{Out} are induced voltage, AC resistance, inductance, capacitance and voltage at the output of coil sensor, respectively.

By considering the skin effect of AC currents, resistance (R_{AC}) of the coil is frequency dependent. Inductance and capacitance of the coil are approximately constant over the operation frequency (frequency independent).

2.1.5 Transfer Function:

Transfer function of the coil sensor is the ratio V_{Out} to $V_{Ind.}$ (Figure 2.4):

$$TF(s) = \frac{V_{Out}(s)}{V_{Ind.}(s)} = \frac{1}{LCs^2 + R_{AC}Cs + 1} \tag{2.34}$$

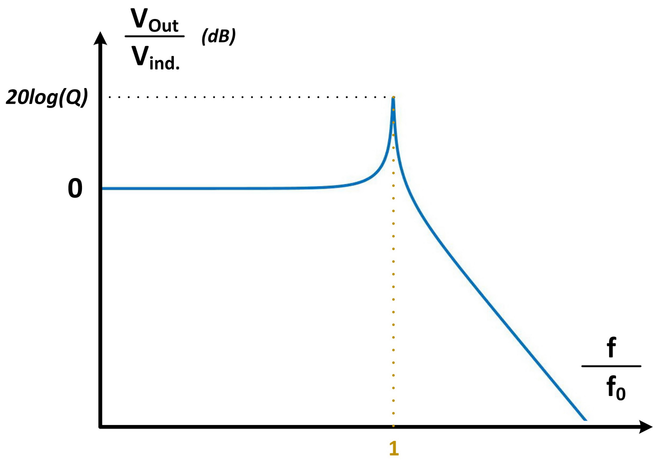

Figure 2.4: Frequency characteristic of coil sensor.

The electrical model of the coil represents a second order system with a damping factor α (or time constant τ (equation 2.35)) dependent on the resistance and inductance of the coil sensor.

$$\alpha = \frac{1}{\tau} = \frac{R_{AC}}{2L} \tag{2.35}$$

When induced voltage $V_{Ind.}$ is applied to the coil sensor it starts to charge with a specific time constant τ.

2.1.6 Impedance (Ω):

The coil impedance can be expressed as (Figure 2.5):

$$Z = \frac{R_{AC} + Ls}{LCs^2 + R_{AC}Cs + 1} \tag{2.36}$$

since $s = j\omega$, equation (2.36) becomes:

$$Z(\omega) = \frac{R_{AC}}{(1 - LC\omega^2)^2 + (R_{AC}C\omega)^2} + j\frac{\omega(L - R_{AC}^2 C - L^2 C\omega^2)}{(1 - LC\omega^2)^2 + (R_{AC}C\omega)^2} = R_s + j\omega L_s \tag{2.37}$$

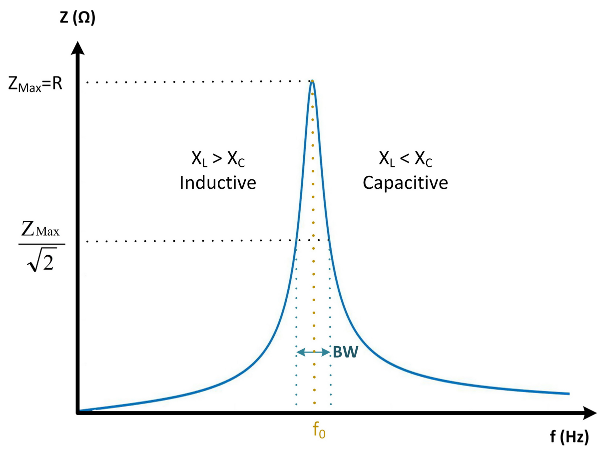

Figure 2.5: Impedance of disk multiple layer receiver coil vs. frequency ($Z_{Max} = R$ is the impedance at resonance frequency f_0, BW is the bandwidth and $X = X_L - X_C$ is the reactance of the coil sensor).

However, measurement devices (like LCR meter) can measure only two components of the coil sensor L_s and R_s that are shown in Figure 2.6 (by supposing measurement at or near the resonance frequency in the inductance region). Both of these terms are frequency dependent and are functions of R_{AC}, L and C of the electrical coil model. Therefore, measured impedance is equal to:

$$Z = R_s + L_s s = R_s + j\omega L_s \tag{2.38}$$

Consequently, R_s and L_s are equal to:

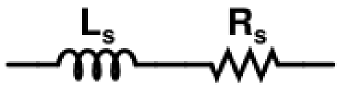

Figure 2.6: Experimental disk multiple layer receiver coil sensor model.

$$R_s = \frac{R_{AC}}{(1 - LC\omega^2)^2 + (R_{AC}C\omega)^2} \tag{2.39}$$

$$L_s = \frac{L - R_{AC}^2 C - L^2 C\omega^2}{(1 - LC\omega^2)^2 + (R_{AC}C\omega)^2} \tag{2.40}$$

2.1.7 Quality Factor:

Quality factor Q of the coil sensor is used to define performance of the electrical coil model. The quality factor Q of the coil sensor is expressed as:

$$Q = \frac{f_0}{\Delta f} = \frac{w_0}{\Delta w} \tag{2.41}$$

The quality factor can also be found using the following expression:

$$Q = \frac{w_0 L}{R_{AC}} = \frac{1}{R_{AC} C w_0} \tag{2.42}$$

where f_0 or ω_0 and Δf or Δw are resonance frequency and bandwidth of the coil, respectively. Bandwidth is the frequency range where the magnitude of the coil impedance is greater than or equal to $\frac{|Z|_{Max}}{\sqrt{2}}$.

2.1.8 Self-Resonance Frequency:

The self resonance frequency is dependent on R_{AC}, L and C (R_{AC} is also dependent on the frequency) of the electrical model (Figure 2.3). It can be found in three ways:

- It is the frequency that makes imaginary part of impedance or admittance become zero [37].

The self-resonance frequency is expressed as:

$$f_p = \frac{1}{2\pi}\sqrt{\frac{1}{LC} - (\frac{R_{AC}}{L})^2} \tag{2.43}$$

This expression can be rewritten as follows:

$$f_p = f_0\sqrt{1 - \frac{1}{Q^2}} \tag{2.44}$$

where:

$$f_0 = \frac{1}{2\pi}\frac{1}{\sqrt{LC}} \tag{2.45}$$

since the quality factor of the sensor is:

$$Q = \frac{\omega_0 L}{R_{AC}} \tag{2.46}$$

At all cases in these experiments:

$$(\frac{R_{AC}}{L})^2 << \frac{1}{LC}$$

then Equation 2.43 can be approximated by:

$$f_p \approx \frac{1}{2\pi}\frac{1}{\sqrt{LC}} \tag{2.47}$$

- For frequencies that maximum magnitude of the impedance is achieved (by regarding coil sensor electrical model) [37]:

At this condition self-resonance frequency of the coil sensor becomes:

$$f_m = f_0\sqrt{\frac{-1}{Q^2} + \sqrt{(\frac{2}{Q^2}) + 1}} \tag{2.48}$$

at all cases in these experiments:

$$\sqrt{\frac{-1}{Q^2} + \sqrt{(\frac{2}{Q^2}) + 1}} \approx 1$$

then equation 2.48 can be approximated by:

$$f_m \approx \frac{1}{2\pi} \frac{1}{\sqrt{LC}} \tag{2.49}$$

- Considering the simulation and experimental results (sections 3.4 and 4.3), quality factor of the wound coils will be bigger than 25. Then, damping ratio (equation 2.52) will be $0 < \xi < 1$. Therefore, this system is in the under-damped state. Consequently, the resonance frequency of the system is equal to [38]:

$$f_d = f_0\sqrt{1 - \xi^2} = f_0\sqrt{1 - \frac{1}{4Q^2}} \tag{2.50}$$

for this case:

$$\frac{1}{4Q^2} \approx 0$$

therefore, the equation 2.50 will become:

$$f_d \approx \frac{1}{2\pi} \frac{1}{\sqrt{LC}} \tag{2.51}$$

The damping ratio of the second order system is equal to:

$$\xi = \frac{1}{2Q} = \frac{R_{AC}}{2}\sqrt{\frac{C}{L}} \tag{2.52}$$

2.1.9 AC Resistance (R_{AC}), Capacitance (C) and Inductance (L) Measurements at Self-Resonance Frequency of the Coil Sensor

The values of R_{AC}, L and C in the electrical circuit model of the coil (Figure 2.3) can be estimated by utilizing electrical measurement devices like LCR meter (Agilent E4980A) and network analyzer (KEYSIGHT N9915A).

- Measurements using LCR Meter at Self Resonance Frequency

At self resonance frequency of the coil sensor, the impedance of the coil has only real part and is maximum (equation 2.37):

$$|Z_{Max}(w_r)| = \frac{R_{AC}}{(1 - LC\omega_r^2)^2 + (R_{AC}C\omega_r)^2} \tag{2.53}$$

Also self resonance frequency of the coil sensor is:

$$f_r \approx \frac{1}{2\pi}\frac{1}{\sqrt{LC}}$$

Therefore $(1 - LC\omega_r^2)$ is approximately zero. Then:

$$|Z_{Max}(w_r)| = \frac{R_{AC}}{(R_{AC}C\omega_r)^2} = Q^2 R_{AC} \tag{2.54}$$

If one measures $|Z_{Max}(w_r)|$ and Q for the coil sensor, R_{AC} can be obtained.

LCR meter measures f_r, $|Z_{Max}(w_r)|$ and $\angle Z_{Max}(w_r)$ (at resonance/self resonance frequency). Also $|Z|$ at 3 dB, f_L, f_H can be measured by the LCR meter. Then quality factor (Q) of the coil sensor can be calculated by equation 2.41 ($BW = f_H - f_L$). From equation 2.54, R_{AC} can be calculated. Finally from equation 2.42, L and C values of the coil sensor can be obtained.

- Measurements using Network Analyzer at Self Resonance Frequency

By using S_{21} parameter of the coil sensor which is measured by a network analyzer, one can calculate the R_{AC}, L and C of the coil electrical model. S_{21} is the forward transmission coefficient (gain) (Figure 2.7). The receiver coil sensor is connected to the network analyzer like a two port device (Figure 2.8). The frequency for minimum point of S_{21} parameter presents the resonance frequency of the coil sensor.

S_{21} parameter is (Figures 2.7 and 2.8):

$$S_{21} = \frac{b_2}{a_1} \tag{2.55}$$

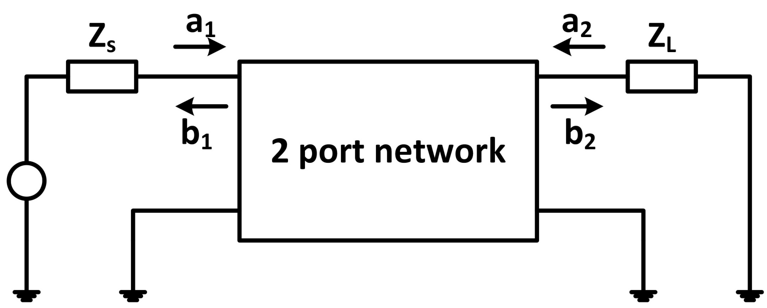

Figure 2.7: S_{21} parameter measurement circuit model (general case).

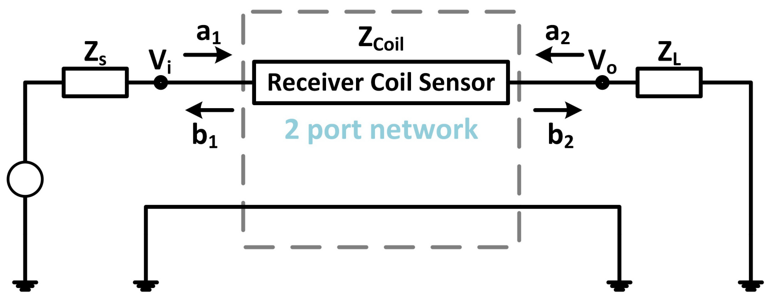

Figure 2.8: S_{21} parameter measurement of a coil.

where b_2 is the reflected signal from port two and a_1 is the incident signal to the port one.

At this configuration, $Z_s = Z_L = 50\ \Omega$ (the source and load resistance of the network analyzer).

S_{21} (equation 2.55) relation with V_i, V_o and $|Z_{Coil}|$ is (Figure 2.8) [39]:

$$S_{21} = 20\log(\frac{2V_o}{V_i}) = 20\log(\frac{2\times 50}{|Z_{Coil}| + (50+50)})$$

Then:

$$S_{21} = 20\log(\frac{100}{|Z_{Coil}| + 100}) \tag{2.56}$$

S_{21} parameter is measured by the network analyzer at the resonance frequency. Then from equation 2.56 one can calculate the Z_{Coil}. As mentioned before, at the resonance frequency one know (Figure 2.6):

$$|Z_{Coil}| \approx R_s$$

Also $|S_{21}|$ at 3 dB, f_L, f_H can be measured by the network analyzer. Then quality factor (Q) of the coil sensor can be calculated by equation 2.41 ($BW = f_H - f_L$). From equation 2.54, R_{AC} can be calculated. Finally from equation 2.42, L and C values of the coil sensor can be calculated.

2.1.10 Induced ($V_{Ind.}$) versus Output Voltage (V_{Out}) of the Receiver Coil

From the transfer function of the coil sensor (equation 2.34), the output voltage of the coil sensor is determined by:

$$V_{Out}(s) = TF(s)V_{Ind.}(s)$$

The produced magnetic field by the tumor in the object is combination of several sinusoidal pulses. Then, let $V_{Ind.}(t)$ be a sinusoidal signal with several periods (Figure 2.9):

$$V_{Ind.}(t) = V_0(u(t) - u(t - T)) \sin(\omega t) \tag{2.57}$$

where V_0 is amplitude of the sinusoidal signal. $u(t)$ is the unit step function. $u(t-T)$ is the unit step function shifted to the T time.

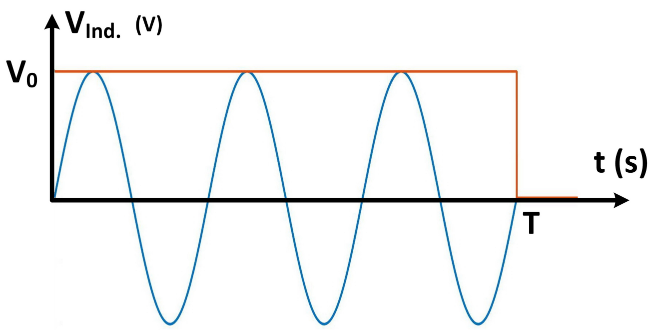

Figure 2.9: Applied $V_{Ind.}$ to the coil sensor.

Then, in the frequency domain it can be expressed as:

$$V_{Ind.}(s) = \frac{V_0}{s^2 + \omega^2}(\omega + V_0 e^{-Ts}(\omega \cos(\omega t) + s \sin(\omega t)))$$

Finally $V_{Out}(s)$ will be:

$$V_{Out}(s) = \frac{1}{LCs^2 + R_{AC}Cs + 1} \frac{V_0}{s^2 + \omega^2}(\omega + V_0 e^{-Ts}(\omega \cos(\omega t) + s \sin(\omega t))) \quad (2.58)$$

Equation 2.58, presents the coil output signal behavior in the frequency domain. Therefore, by taking inverse Laplace from equation 2.58, the time domain behavior (transient behavior) can be evaluated.

From transfer function of coil sensor (equation 2.34) one can conclude that if the frequency of the induced voltage ($V_{Ind.}$) is the self resonance frequency of the coil. Then, the output voltage will be the quality factor times the induced voltage:

$$TF(\omega_0) = \frac{V_{Out}(\omega_0)}{V_{Ind.}(\omega_0)} = \frac{-j}{R_{AC}C\omega_0} = -jQ \quad (2.59)$$

where j is the unit imaginary number. If the magnitude of both sides are calculated:

$$\left| \frac{V_{Out}(\omega_0)}{V_{Ind.}(\omega_0)} \right| = Q \quad (2.60)$$

the magnitude of V_{Out} can be expressed as:

$$|V_{Out}(\omega_0)| = Q \, |V_{Ind.}(\omega_0)| \quad (2.61)$$

Equation 2.61 proves that if one uses the coil at the self resonance frequency (or resonance frequency), output voltage will be increased by coil quality factor which is quite useful for low amplitude signal measurements by the coil sensors (Figure 2.10).

Note that, as it is shown in the equation 2.59, there will be a 90 ° phase difference between the output and induced voltages.

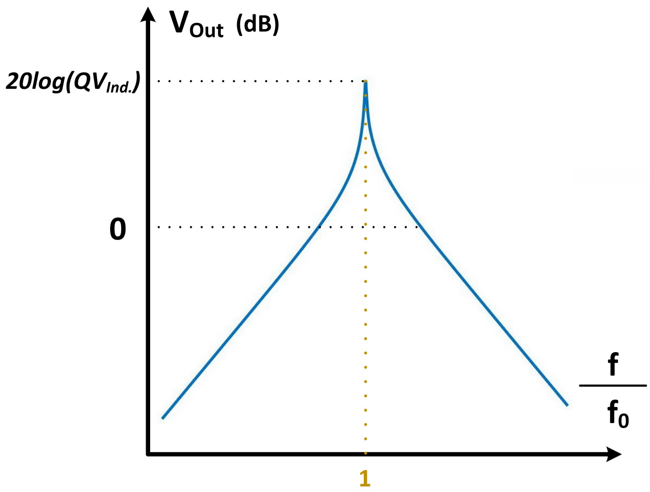

Figure 2.10: V_{Out} of the receiver coil sensor vs. normalized frequency.

2.1.11 Ringing Effect:

When the applied magnetic field ceases, the pick-up voltage, i.e., the output voltage of the receiver coil, does not drop to zero instantaneously. The oscillations at the resonance frequency continues depending on the damping factor of the coil transfer function. This is known as the "ringing effect" of the coil sensor. It is obvious that, the ringing duration can be decreased by increasing the damping factor. This can be achieved by decreasing the inductance of the coil sensor. However, to keep the self resonance frequency fixed, the capacitance must be increased yielding a decrease in the quality factor, which is not desired. Also, from equation 2.35 one can increase the damping factor by increasing the resistance of the coil. In this case, the internal noise of the coil sensor will be increased which is not a desirable phenomenon. In addition, the self resonance frequency of the coil will also be changed (equations 2.43, 2.48 and 2.42). Consequently, there is a trade off between the ringing effect and quality factor of the coil sensor.

2.1.12 Tuning Circuit:

To adjust the resonance frequency of the coil sensor one can add a capacitance (C_{II}) parallel to the coil sensor's terminals. However, by adding a resistance (R_{II}) parallel to the coil output, coil sensor's output voltage V_{Out} exhibits frequency characteristic with a plateau (Figures 2.11 and 2.12). In this case the lower and upper corners of the bandwidth are determined by [26, 27]:

$$f_l = \frac{R_{AC} + R_{II}}{2\pi L} \tag{2.62}$$

$$f_h = \frac{1}{2\pi R_{II} C} \tag{2.63}$$

The plateau of the system is defined by ζ:

$$\zeta = \frac{R_{AC}}{R_{II}} \tag{2.64}$$

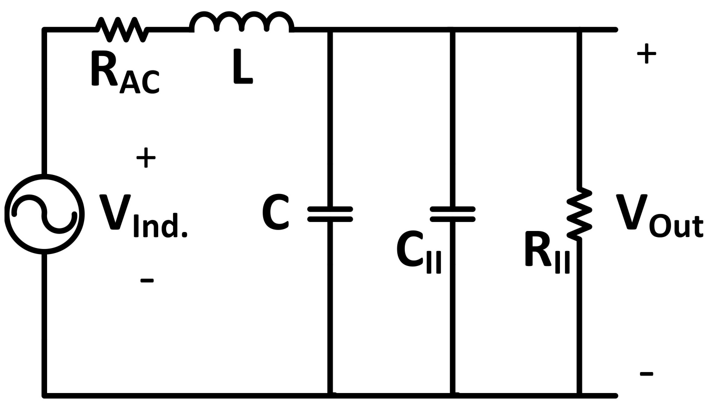

Figure 2.11: Tuning Circuit of Receiver Coil Sensor.

Therefore in order to determine new transfer function of the coil sensor, it is necessary to define new parameters based on the circuit model given in Figure 2.12:

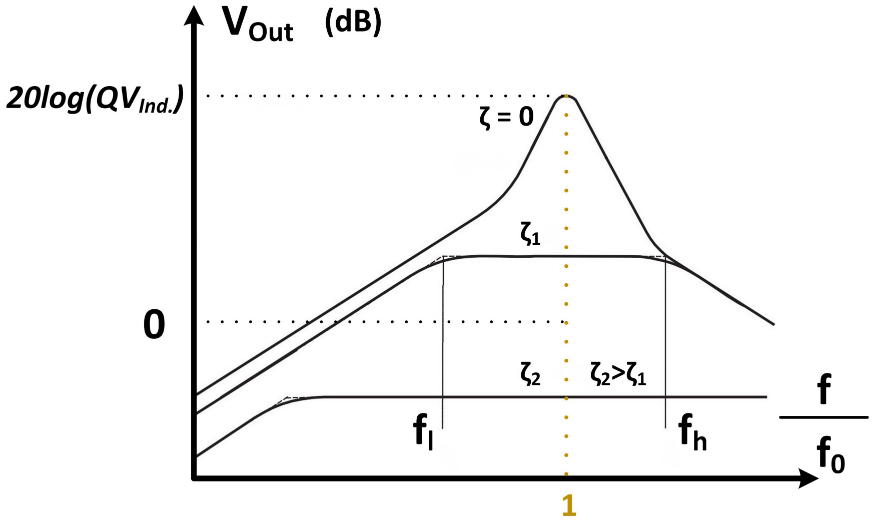

Figure 2.12: Output voltage of the tuned coil sensor with plateau at desired frequency.

- Voltage Division Factor

$$VDF = \frac{R_{II}}{R_{AC} + R_{II}}$$

- Equivalent Capacitance

$$C_{Total} = C + C_{II}$$

- Impedance of the Coil

$$Z_1(s) = R_{AC} + Ls$$

$$Z_2(s) = \frac{R_{II}\left(\frac{1}{C_{Total}s}\right)}{R_{II} + \left(\frac{1}{C_{Total}s}\right)}$$

- Resonant Frequency

$$\omega_r = \frac{1}{\sqrt{VDF \cdot L \cdot C_{Total}}} \tag{2.65}$$

$$f_r = \frac{1}{2\pi\sqrt{VDF \cdot L \cdot C_{Total}}}$$

- Damping Factor

  The damping factor is the amount by which the oscillation of a circuit gradually decrease over time.

$$DF = \frac{\sqrt{VDF}}{2}[\frac{\sqrt{L/C_{Total}}}{R_{II}} + \frac{R_{AC}}{\sqrt{L/C_{Total}}}]$$

- Output Voltage of the Coil Sensor

$$V_{Out}(s) = \frac{Z_2(s)}{Z_1(s) + Z_2(s)} V_{Ind.}(s)$$

  by substituting $Z_1(s)$, $Z_2(s)$ expressions, $V_{Out}(s)$ becomes:

$$V_{Out}(s) = \frac{R_{II}}{R_{II}LC_{Total}s^2 + (L + R_{AC}R_{II}C_{Total})s + R_{II} + R_{AC}} V_{Ind.}(s)$$

Transfer function of the coil sensor is then expressed as:

$$TF(s) = \frac{V_{Out}(s)}{V_{Ind.}(s)} = \frac{R_{II}}{R_{II}LC_{Total}s^2 + (L + R_{AC}R_{II}C_{Total})s + R_{II} + R_{AC}}$$

or:

$$TF(s) = \frac{VDF}{VDF \cdot LC_{Total}s^2 + 2DF\sqrt{VDF \cdot LC_{Total}}s + 1} \tag{2.66}$$

By setting $s = j\omega$ in the transfer function (and substituting 2.65):

$$TF(\omega) = \frac{VDF}{1 - (\frac{\omega}{\omega_r})^2 + 2j \cdot DF\frac{\omega}{\omega_r}} \tag{2.67}$$

Thus, the magnitude of $TF(\omega)$ will be:

$$|TF(\omega)| = \frac{VDF}{\sqrt{(1-(\frac{\omega}{\omega_0})^2)^2 + (2DF\frac{\omega}{\omega_0})^2}} \tag{2.68}$$

Therefore, the magnitude of the output voltage can be expressed as:

$$|V_{Out}(\omega)| = |TF(\omega)|\,|V_{Ind.}(\omega)| \tag{2.69}$$

Notes:

- Coefficient of s^2 is equal to the $\left(\frac{1}{\omega_r}\right)^2$.
- Coefficient of the s is equal to the $\frac{1}{Q\omega_r} = \frac{2DF}{\omega_r} = 2DF\sqrt{VDF \cdot LC_{Total}}$.
- DF should be determined $0.5 < DF < 0.7$ (by trade off between R_{II} and C_{Total}).
- VDF is $0 < VDF < 1$.

When an oscilloscope or amplifier is connected to the coil sensor output along with tuning circuit (Figure 2.13), capacitance and resistance of these devices will modify the receiver circuit. In such a case:

$$C_{II} = C_{II} + C_{Device}$$

$$R_{II} = \frac{R_{II}R_{Device}}{R_{II} + R_{Device}}$$

2.1.13 Sensitivity ($\frac{V}{Hz\frac{A}{m}}$):

The noise equivalent magnetic field can be obtained using the relationship between the sensitivity and induced voltage [27]:

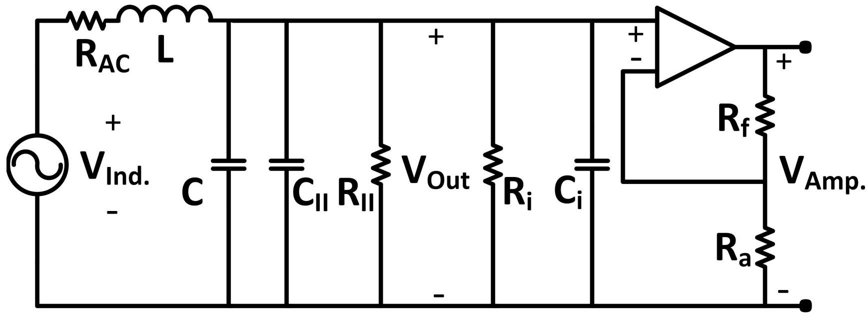

Figure 2.13: Coil sensor, tuning circuit and amplifier (R_i and C_i) are input resistance and capacitance of the amplifier.

$$S = \frac{V_{Ind.}}{f \cdot H} \tag{2.70}$$

where $H = \dfrac{B_0}{\mu_0}$ is the magnetic field strength (A/m).

Using equation 2.33, sensitivity of the coil sensor can be expressed as: :

$$S = \frac{\mu_0 \pi^2}{2} TN \cdot MD^2 \tag{2.71}$$

where TN denotes the number of turns, and MD is the mean diameter of the coil. Using equations 2.2, 2.3 and 2.4, sensitivity can also be expressed as follows::

$$S = \frac{\pi}{4} \mu_0 PF \cdot Len \frac{(D - D_i)(D + D_i)^2}{Wd^2} \tag{2.72}$$

where μ_0 is free space permeability. PF, Len, D and D_i are packing factor, length, outer and inner diameter of the coil, respectively. Wd is the wire diameter.

Following are useful comments about the sensitivity of coil sensors:

- Sensitivity is proportional to the cube of outer diameter (D^3).
- Sensitivity is proportional to the coil length (Len).
- If outer and inner diameters of the coil sensor are kept fixed (i.e., winding

depth is fixed), sensitivity will be increased by decreasing the wire diameter. However, turn number of the coil sensor will be increased in that case.

2.1.14 Signal to Noise Ratio (SNR):

SNR is the ratio of the signal that carries information to the unwanted interference [26]. In the case of sole thermal noise Vth, SNR an be expressed as:

$$SNR = \frac{V_{Ind.}}{V_{Th}} \tag{2.73}$$

Using equations 2.30 and 2.31, it is possible to obtain the following SNR expression:

$$SNR = \frac{\pi^2}{2} TN \cdot MD^2 \frac{f}{\sqrt{\Delta f}} \frac{B_0}{\sqrt{4k_B \cdot T \cdot R_{DC}}} \tag{2.74}$$

An alternative SNR expression can be obtained using equations 2.2, 2.3 and 2.4:

$$SNR = \frac{\pi}{4} PF \cdot Len \cdot \frac{f}{\sqrt{\Delta f}} \frac{(D - D_i)(D + D_i)^2}{Wd^2 \sqrt{4k_B \cdot T \cdot R_{DC}}} B_0 \tag{2.75}$$

If one substitutes the R_{DC} expression (equation 2.18) in equation 2.75, the SNR at temperature $T\,^\circ K$ can be expressed as:

$$SNR = \frac{\pi^{\frac{3}{2}}}{16} \sqrt{PF} \sqrt{Len} \frac{f}{\sqrt{\Delta f}} \frac{(D + D_i)\sqrt{D^2 - D_i^2}}{\sqrt{k_B \cdot T \cdot \rho_0 (1 + \beta(T - T_0))}} B_0 \tag{2.76}$$

Following are comments about the SNR of a coil sensor:

- SNR increases linearly by increasing frequency.
- SNR is approximately proportional to the square of the outer diameter (D^2).
- SNR increases by the square root of coil sensor length ($\sqrt{Len}$).
- SNR is not dependent on the wire diameter (Wd).
- SNR has a non-linear relation with temperature ($\frac{1}{\sqrt{T^2 - TT_0}}$).

- SNR has a non-linear relation with the resistivity and resistance temperature coefficient ($\frac{1}{\sqrt{\rho_0}}$ and $\frac{1}{\sqrt{\beta}}$) of the conductor (coil wire).

Investigations show an optimum relation between the outer diameter and length of the coil sensor.Following are important consideration that can be used in coil sensor design [26]:

Then:

- $\frac{Len}{D} = 0.67 \sim 0.866$ ($\frac{D_i}{D} = 0$ for 0.67 and $\frac{D_i}{D} = 1$ for 0.866) are the most suitable ratios for one and multilayer coils, respectively.
- It is better to keep ratio of $\frac{D_i}{D}$ less than 0.3.

CHAPTER 3

NUMERICAL STUDIES FOR COIL SENSOR DESIGN

3.1 Introduction

To design a coil sensor with desired characteristics, one must determine its physical geometry and electrical properties previously. In addition, to calibrate the receiver coil, a transmitter coil must be designed to generate magnetic fields of predetermined magnitude and frequency. Finally, before winding the coil it is necessary to analyze the characteristics of the designed sensor. In this thesis study, several simulation programs are prepared to analyze the characteristics of disk multiple layer coil sensor and to design the transmitter coil for calibration. All simulation programs are written in the 64 bit version of MATLAB edition R2015b. Also, circuit simulations are done by LTspice version $XVII(x64)$ (Linear Technology free simulation software).

3.2 Simulation of Disk Multiple Layer Transmitter Coil

To calibrate the designed coil sensors, one must also design a transmitter coil that generates the specified field characteristics. As it discussed in the previous chapter, the impedance of coil becomes high at the self-resonance frequency. Then if the self-resonance frequency of the transmitter coil is adjusted to 1 MHz (operating frequency of experiments), it will be difficult to design a driver circuit and apply high currents to the transmitter coil. Consequently, self-resonance frequency of the transmitter coil must be adjusted at higher frequencies (more than 1 MHz). In this condition, the transmitter coil will work at its inductance region where its input impedance is fairly small. In this study, a disk multiple layer coil (geometry) with predetermined physical properties (Table 3.1) is assumed. The electrical characteristics of the transmitter coil at 1 MHz are presented in Table 4.4. The transmitter coil generates a position dependent magnetic field at 1 MHz.

Table 3.1: Physical properties of the transmitter coil.

Inner Diameter (cm)	Outer Diameter (cm)	Length (cm)	Wire Diameter (cm)	Turn Number	Layer Number	Conductor Resistivity (Ωm)
3.28	3.63	2.18	0.95	45	2	16.78e-9

Inputs of the simulation program are the physical properties of assumed transmitter coil. Output is the position dependent magnitude of the magnetic field produced by the transmitter coil. This magnetic field calculated on the axis of transmitter coil depends on the distance from transmitter coil center. In addition, the magnetic field magnitude is calculated inside a volume (volume of receiver coil sensor) on the axis of the transmitter coil at a specific distance from transmitter center. Other outputs of this simulation program are the induced (equation 2.31) and output voltage (equation 2.61) of an specific receiver coil sensor ($V_{Ind.}$ and V_{Out}). Finally, from the induced or output voltage of the receiver coil sensor one can estimate the mean magnetic field strength that is measured by the coil sensor (equations (2.31), (2.33), and (2.61)).

Magnetic field distribution on the axis of the designed transmitter coil is shown in Figure 3.1 (by assuming 35 mA RMS current flowing in the transmitter coil).

A receiver coil Sensor II is designed and assumed to be placed at different locations. Its physical and electrical characteristics are shown in Tables 3.2, 3.3 and 3.4. The simulated mean magnetic field strengths are shown in Table 3.6.

* In Table 3.3, capacitance of the coil sensor is estimated as 68 pF by the simulator. However, when the same coil is realized, the capacitance value is measured as 108 pF. In this case, all parameters that depend on the capacitance value will be incorrectly

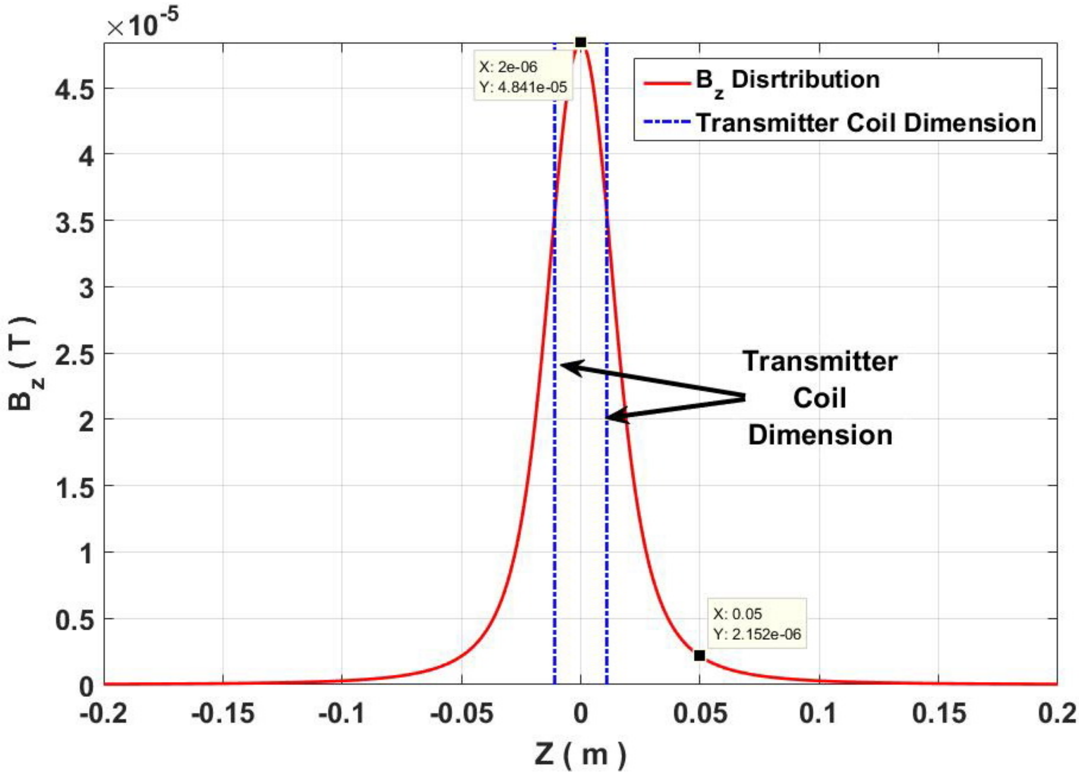

Figure 3.1: Transmitter coil magnetic field distribution on the z axis.

Table 3.2: Simulated physical properties of the receiver coil Sensor II.

Inner Diameter (cm)	Outer Diameter (cm)	Length (cm)	Wire Diameter (cm)	Turn Number	Layer Number	Conductor Resistivity (Ωm)
4.1	4.21	0.527	0.31	33	2	16.78e-9

Table 3.3: Simulated electrical properties of the receiver coil Sensor II.

R_{DC} (Ω)	C (pF)	L (μH) (eq. 2.23)	L (μH) (eq. 2.24)	R_{AC} (Ω) (eq. 2.20)	R_{AC} (Ω) (eq. 2.21)
1.13	108*	83.30	82.16	17.25	29.6

estimated. Therefore, measured capacitance is used. Despite of implementing several methods to estimate the capacitance of disk multiple layer coil sensors accurately, estimated capacitances were not acceptable. One reason in this discrepancy may be winding the coil sensors by hand. In addition, the exact material of wire's insulator coating were not clear (unknown permittivity).

Table 3.4: Calculated electrical properties of the receiver coil Sensor II by using different formulas for the self-resonance frequency.

f_r (kHz) (eq. 2.43)	f_r (kHz) (eq. 2.48)	f_r (kHz) (eq. 2.50)	f_{3dB} (kHz)	Quality Factor (eq. 2.41)
1688.54	1689.51	1689.28	55.50	30.42

When the receiver coil Sensor II is connected to the SMA cable, electrical characteristics of the sensor changes. By connecting 200 pF capacitance paralleled to the coil with SMA cable, the desired electrical parameters of the coil are obtained and presented in the Table 3.5. The resonance frequency (not the self-resonance frequency) of coil is be adjusted to be about 1 MHz.

Table 3.5: Measured electrical properties of the receiver coil Sensor II at resonance frequency SMA cable and 200 pF parallel capacitance is connected.

R_{DC} (Ω)	C (pF)	L (μH)	R_{AC} (Ω)	f_r (kHz)	Quality Factor	f_{3dB} (kHz)
1.13	318*	82	13.65	984.60	37.28	26.25

Magnitude of magnetic field is estimated using the simulation program for receiver coil Sensor II. Consequently, by winding and adjusting resonance frequency of such a receiver coil, one expects to measure approximately the same values for the magnetic field at that locations.

Table 3.6: Simulated mean magnetic field versus distance for the receiver coil Sensor II

Distance (cm)	Transmitter Current (mA)	Simulated Mean Magnetic Field (μT)
10	34.89	0.2394
12	35.40	0.1464
13	35.83	0.1183
14	34.77	0.0931
15	35.12	0.0772

3.3 Simulating the Driver Circuit

To apply the desired currents to the transmitter coil, a power amplifier that works at 1 MHz must be designed. For this case, a class E power amplifier is simulated (Figure 3.2) [40]. The IRF540n is a power MOSFET transistor in the power amplifier circuit.

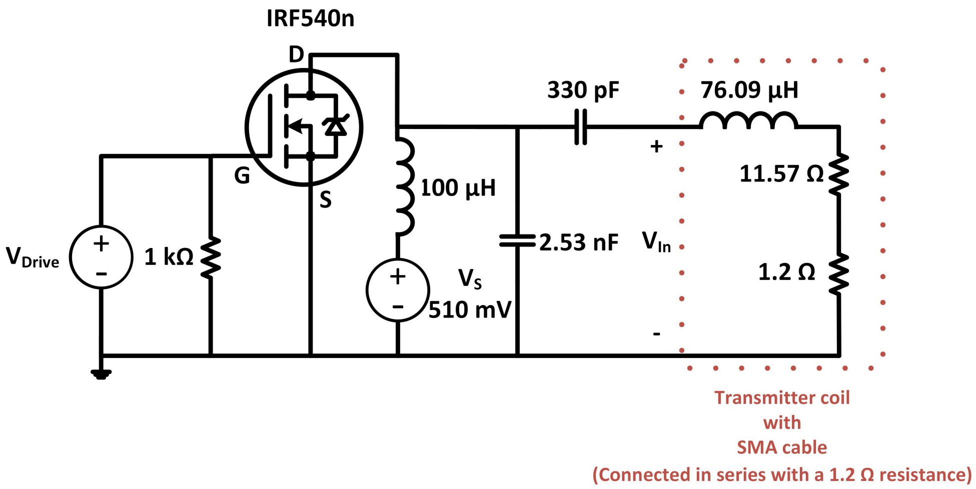

Figure 3.2: Transmitter coil driver.

In the simulation program (LTspice (version XVII(x64))), V_{Driver} is a train pulse with 4 V amplitude, 1 MHz frequency, 2 V offset and 50% duty cycle (rise and fall time are set to the 5 ns). A 1.2 Ω resistance is connected in series with the transmitter coil to estimate amplitude of the current which is flowing on the transmitter coil (Figure 3.2).

One can adjust the applied voltage to the transmitter coil by adjusting the amplitude of the input voltage, offset voltage and V_s.

3.4 Simulation of Disk Multiple Layer Coil Sensor

To estimate the electrical characteristics from the geometry and physical properties of coil sensors, several programs are prepared. Using these programs, one can predict R_{DC}, frequency dependent R_{AC}, inductance, capacitance and resonance frequency of the coil. The purpose of this part of the thesis study is to develop a simulator that determines sensor parameters affecting the sensitivity and SNR. The final aim is to estimate the induced voltage on the coil sensor. One can try to obtain the higher amplitudes at 1 MHz by adjusting parameters like coil outer and inner diameters, coil length and diameter of the winding wire.

In this thesis study, the designed coil has a specific self-resonance frequency. To adjust the resonance frequency of a coil sensor at desired frequency, one can add capacitance C_{II} parallel to the coil output. In addition, coil sensor's output voltage V_{Out} (and seen impedance from output of the coil) exhibits frequency characteristic with a plateau by adding a resistance R_{II} parallel to the coil output. In fact, by adjusting these parameters one tries to set the resonance frequency of the coil at 1 (MHz) same as the ultrasonic transducer.

3.4.1 Estimating the Electrical Characteristics from the Geometry and Physical Properties of the Coil Sensor

In this part of the simulations, relation between the electrical characteristics and different physical parameters of the coil sensor are calculated and demonstrated. The simulator program uses the outer and inner diameter, coil length and wire diameter of the wire employed in coil winding. In addition, the packing factor, experiment temperature, conductor resistivity and permeability, wire insulator permittivity should be specified. For receiver coil Sensor I (simulated physical parameters are shown in the Table 3.7), the simulated winding is shown in Table 3.8. Estimated electrical characteristics of Sensor I are presented in Tables 3.9, 3.10.

Table 3.7: Simulated physical properties of the receiver coil Sensor I.

Inner Diameter (cm)	Outer Diameter (cm)	Length (cm)	Wire Diameter (cm)	Conductor Resistivity (Ωm)
3.514	3.62	0.868	0.31	16.78e-9

Table 3.8: Simulated winding properties of the receiver coil Sensor I.

Layer Number	Turn per Odd Layers	Turn per Even Layers	Number of Turns	Packing Factor
2	28	27	55	$\frac{\pi}{2\sqrt{3}}$

Table 3.9: Simulated electrical properties of the receiver coil Sensor I.

R_{DC} (Ω)	C (pF)	L (μH) (eq. 2.23)	L (μH) (eq. 2.24)	R_{AC} (Ω) (eq. 2.20)	R_{AC} (Ω) (eq. 2.21)
1.63	184*	159.05	157.72	19.1	29.33

* In Table 3.9, capacitance of the coil is estimated about 56 pF. In estimating the coil's capacitance, none of the implemented formulations published in the literature yielded values close to the measured ones. The simulation results are exactly matched with the paper results, but practical measurement of the capacitance approaches to different values. As a result, R_{AC}, f_r, quality factor and f_{3dB} of the coil that depend on the capacitance value, are estimated wrongly. Therefore, only measured capac-

itance are employed. Some of the electrical properties of the coil sensors such as inductance, R_{AC} and f_r (f_p, f_m and f_d) are estimated by more than one methods. All methods except capacitance estimations, provide acceptable results. In Table 3.10, inductance and AC resistance values that are calculated by equations 2.24 and 2.21, are used to calculate the resonance frequency and quality factor. Both methods of inductor estimation, give values that have an acceptable discrepancy. By regarding experiment data, AC resistance value that is calculated by equation (2.21) gives a better estimation.

Table 3.10: Calculated electrical properties of the receiver coil Sensor I by using of simulated data.

f_r (kHz) (eq. 2.43)	f_r (kHz) (eq. 2.48)	f_r (kHz) (eq. 2.50)	f_{3dB} (kHz)	Quality Factor (eq. 2.41)
942.786	943.27	943.16	28.9	32.35

3.4.2 Electrical Characteristics of Coil while Sweeping One of the Physical Parameters

In the simulation programs, all physical properties except one of them are kept fixed and the relation between the varying parameter and electrical characteristics is investigated. In addition, this simulation program determines optimum values of outer, inner diameters, coil length, wire diameter, turn number and number of layers for the receiver coil. Optimum values for parameters are where the output voltage is maximized and the resonance frequency is about 1 MHz. Output voltage, SNR, sensitivity, R_{DC}, R_{AC}, capacitance, inductance and self-resonance frequency versus outer diameter changes (physical properties are shown in the Table 3.11), are presented in Figures 3.3, 3.4, 3.5, 3.6, 3.7, 3.8, 3.9 and 3.10, respectively. The following are the list of assumptions used in the simulations:

- The coil packing factor is $\frac{\pi}{2\sqrt{3}}$.
- Temperature $T = 300\ ^\circ K$.

- Magnetic flux density (1 MHz) to be measured is about 10 pT.
- The resistivity of the wire conductor is 16.78 $n\Omega m$.
- The wire insulator relative permittivity is 3.5.
- The wire conductor permeability is 1.256629 $\mu H/m$.
- Bandwidth is 200 kHz.

Table 3.11: Physical properties of a receiver coil sensor.

Inner Diameter (cm)	Outer Diameter (cm)	Length (cm)	Wire Diameter (cm)	Conductor Resistivity (Ωm)
1	1.06∼8	0.868	0.31	16.78e-9

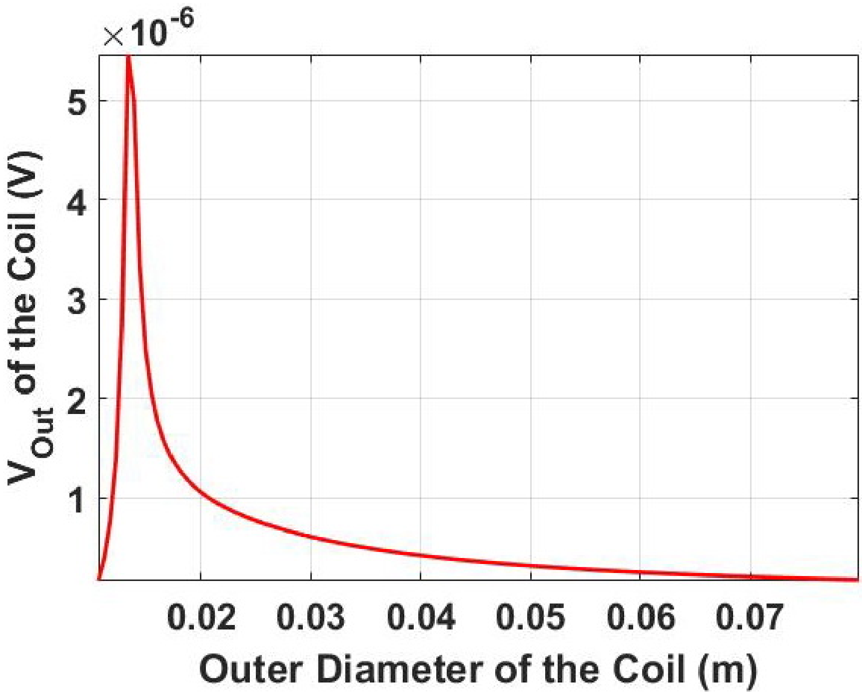

Figure 3.3: V_{Out} versus outer diameter changes.

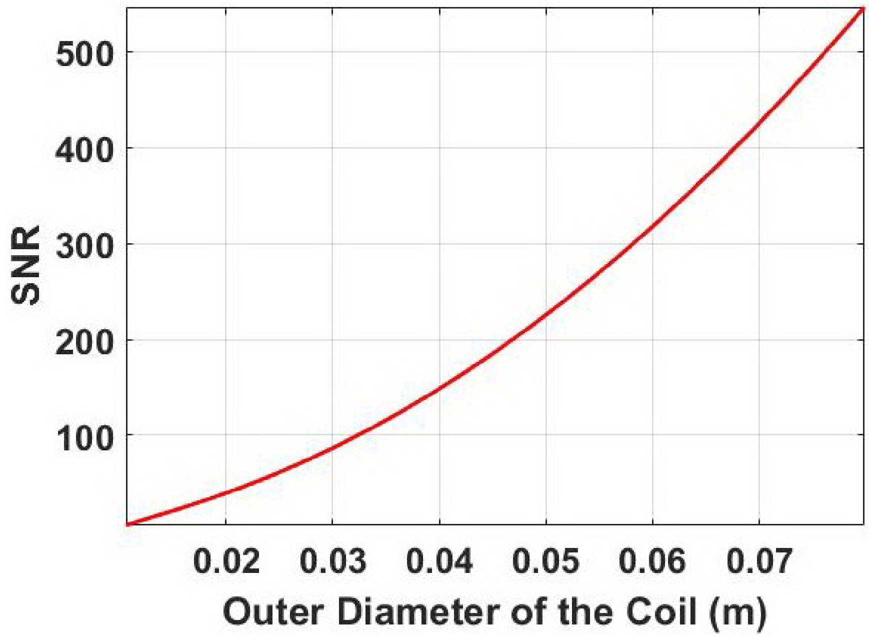

Figure 3.4: SNR versus outer diameter changes.

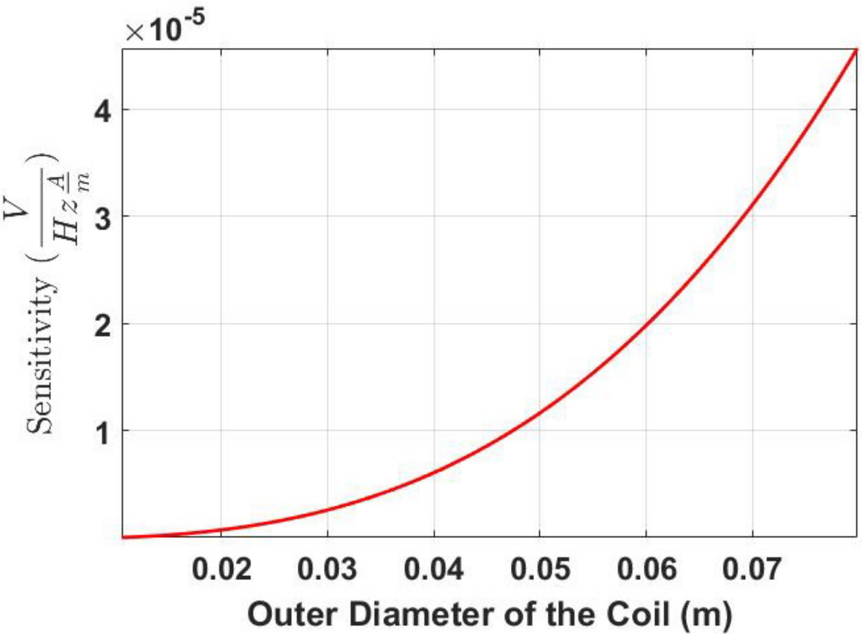

Figure 3.5: Sensitivity versus outer diameter changes.

Figure 3.3, shows that the maximum output voltage is produced when the outer diameter of the coil sensor is about 1.33 cm. As it presented in Figures 3.4 and 3.5, the SNR and sensitivity increases as the outer diameter increases. Figure 3.6 shows that by increasing outer diameter of the coil, R_{DC} increases because of increasing turn number and wire length. Figure 3.7 shows that by increasing outer diameter of the coil, R_{AC} increases because of increasing R_{DC}.

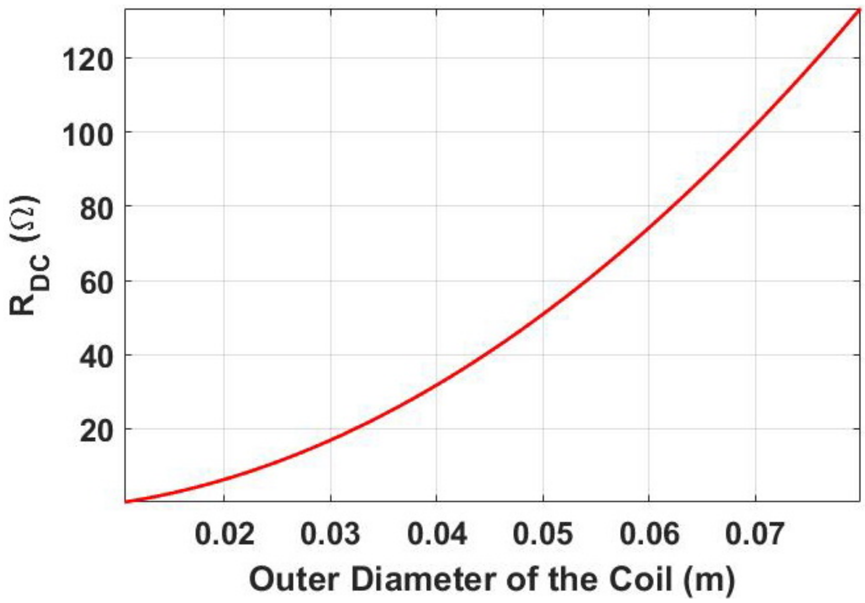

Figure 3.6: R_{DC} versus outer diameter changes.

By increasing the outer diameter of the coil sensor, i.e. increasing turn number of the coil, capacitance decreases (Fig. 3.8).

By increasing the outer diameter of the coil sensor, i.e. increasing the turn number of the coil, inductance increases (Figure 3.9). By increasing the outer diameter of the coil sensor, i.e. increasing turn number of the coil, resonance frequency of the sensor decreases (Figure 3.10).

Same analysis can be done for every receiver coil sensor by assuming one of the parameters (inner diameter, coil length or wire diameter) variable while the other parameters are fixed.

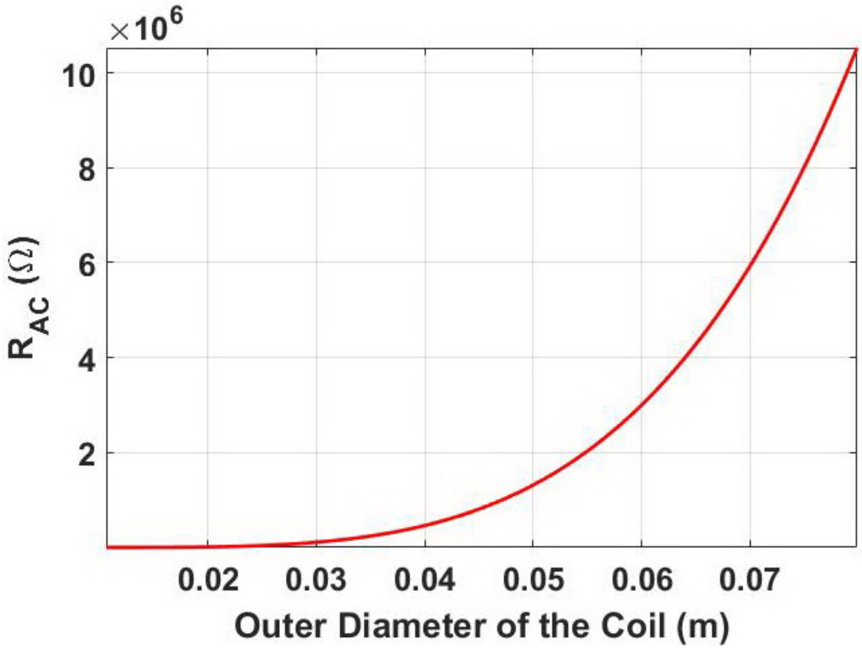

Figure 3.7: R_{AC} versus outer diameter changes.

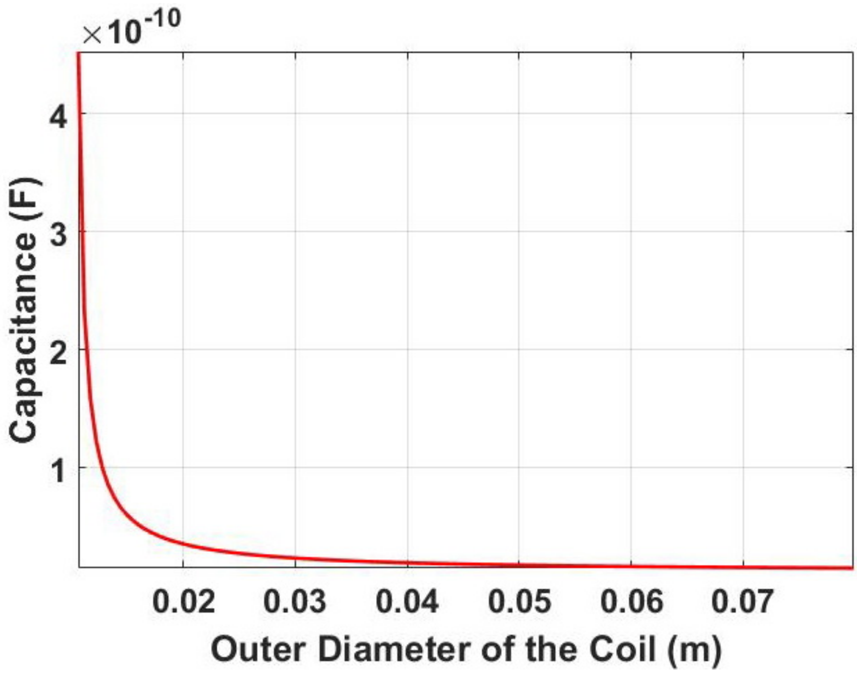

Figure 3.8: Capacitance versus outer diameter changes.

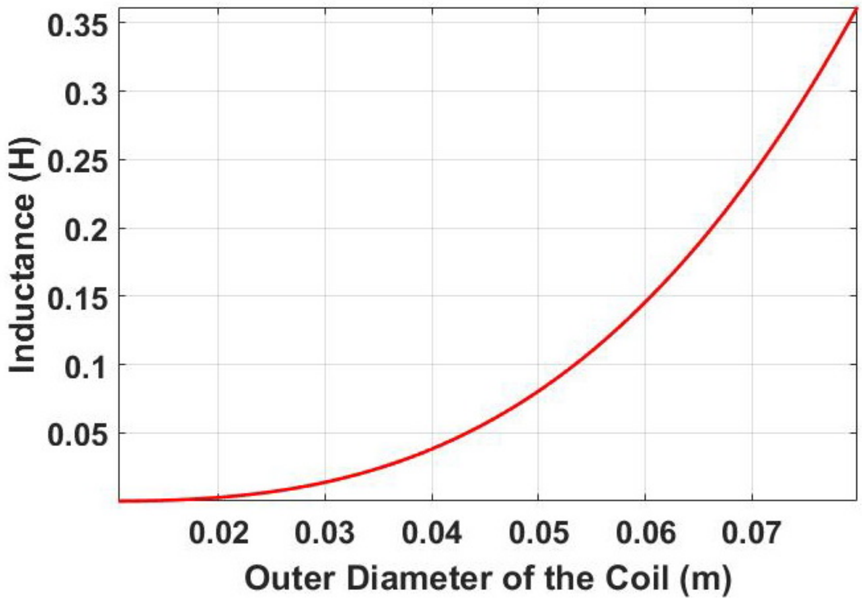

Figure 3.9: Inductance versus outer diameter changes.

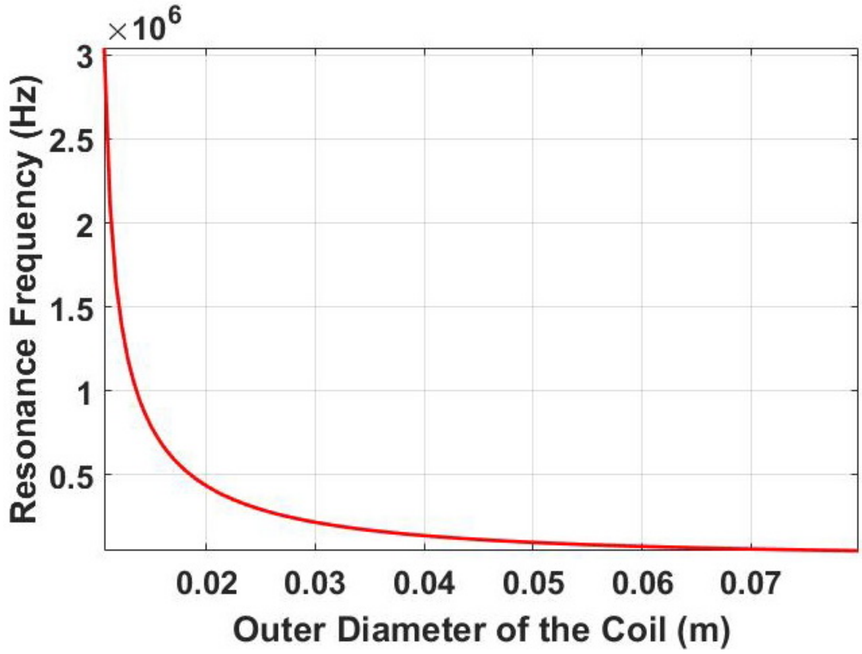

Figure 3.10: Resonance frequency versus outer diameter changes.

If one compares the effectiveness of coil sensor parameters on the output voltage, the effects of wire diameter changes is considerably larger than the other parameters.

Final aim of this section is to adjust the resonance frequency of the coil sensor at 1 MHz. Note that, at this frequency, maximum SNR and sensitivity for the coil sensor can be obtained. From the simulation results shown in the next section, one can conclude that the maximum output signal on the coil sensor can be produced at 1 MHz.

3.4.3 Impedance Characteristics of a Coil Sensor

In this part of simulations, changes in coil impedance and R_{AC} as a function of frequency are investigated. In this part, characteristics of Sensor II is analyzed. Figure 3.11 and Figure 3.12 show the magnitude and phase plot of the coil impedance, respectively. Figure 3.13 and Figure 3.14 show the real and imaginary parts of the coil impedance as a function of frequency. Figure 3.15 presents the change in R_{AC} as a function of frequency.

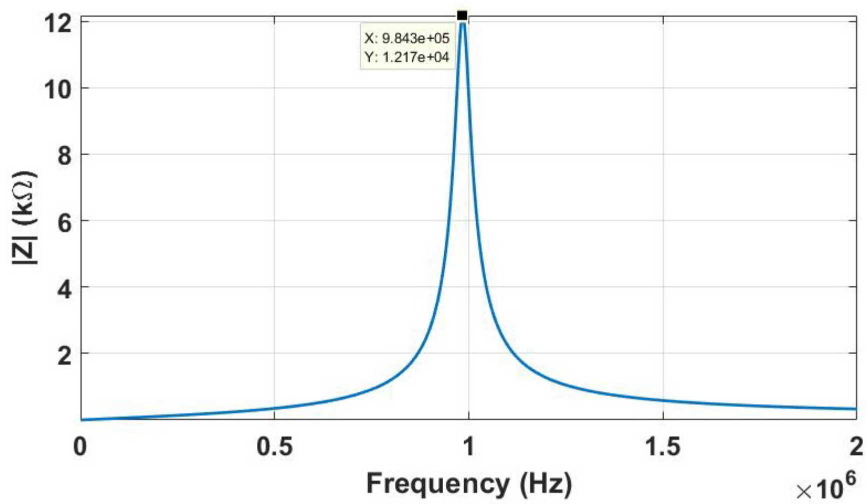

Figure 3.11: Magnitude plot of coil impedance as a function of frequency.

As it shown in Figure 3.15, the R_{AC} resistance is increasing by increasing the fre-

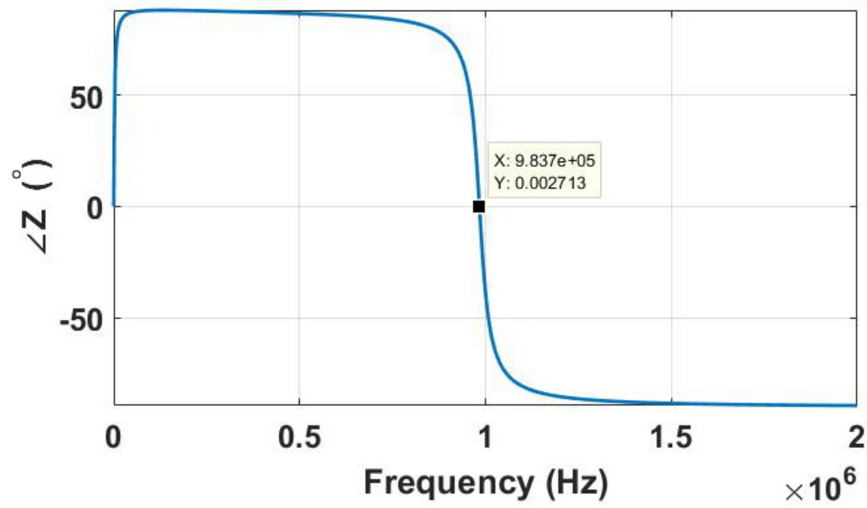

Figure 3.12: Phase plot of coil impedance as a function of frequency.

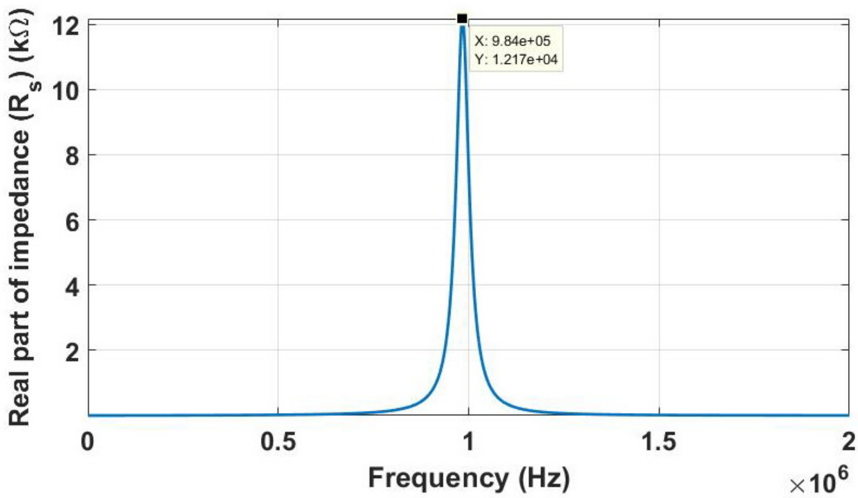

Figure 3.13: Characteristic of real part of impedance ($k\Omega$) versus frequency (Hz).

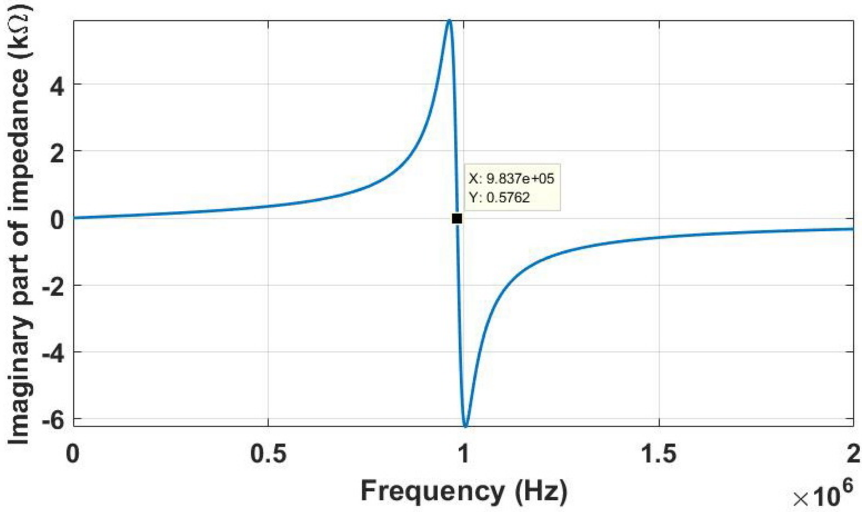

Figure 3.14: Characteristic of imaginary part of impedance ($k\Omega$) versus frequency (Hz).

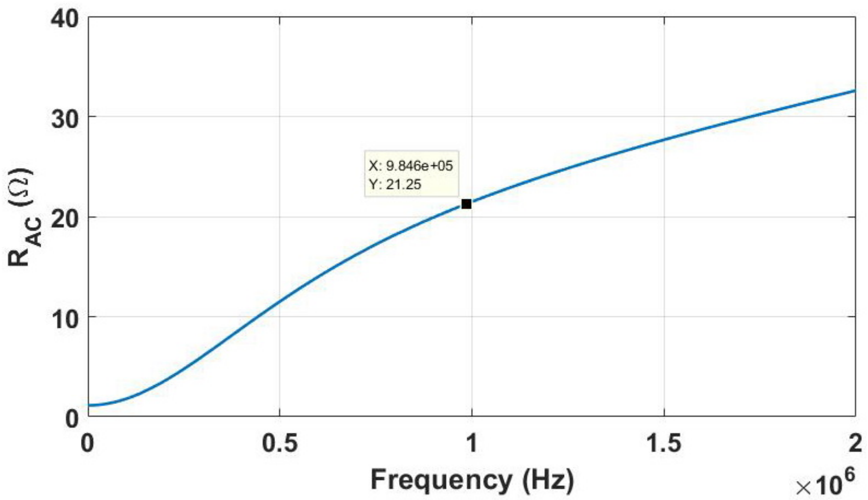

Figure 3.15: Characteristic of R_{AC} (Ω) versus frequency (Hz).

quency. The simulated resonance frequencies by equations (2.43), (2.48) and (2.50) are 984.246 kHz, 984.601 kHz and 1.014 MHz, respectively. The estimated resonance frequencies by three mentioned methods present an acceptable discrepancy.

3.4.4 Induced versus Measured Voltage on the Receiver Coil Sensor

In this part, the effect of damping factor on the induced and output voltage of the receiver coil sensor is investigated using simulation studies. In the first step of the simulation, a signal at the resonance frequency of the receiver coil is applied to the coil sensor (about 1 MHz). In this part of simulation, three 1 (V) sinusoidal signals with 3, 10 and 60 periods are applied (induced) to coil Sensor II and output voltages are observed as a function of time (Figures 3.16, 3.17 and 3.18).

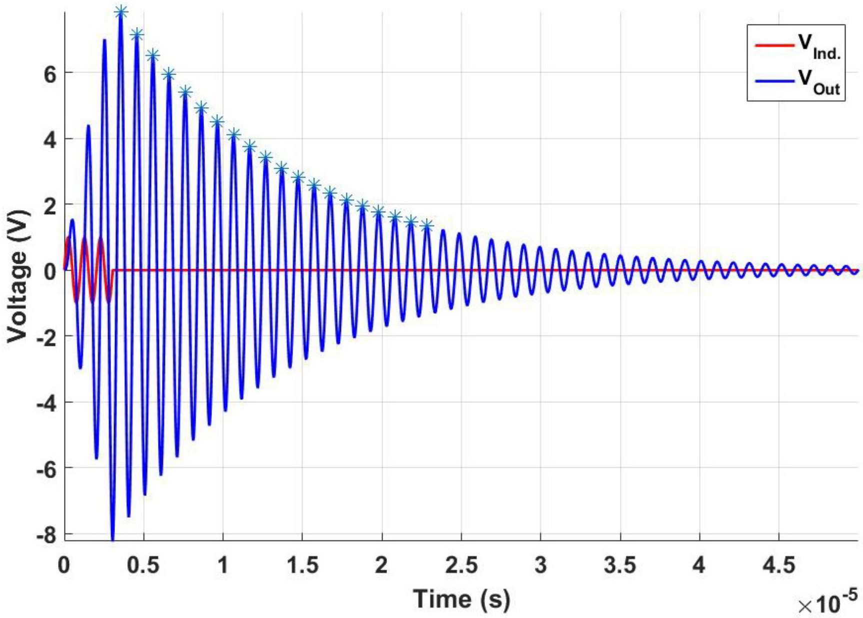

Figure 3.16: Induced sinusoidal signal (1(MHz), 3 priods and 1 (V) amplitude) versus output voltage.

The time constant of the receiver coil evaluated equation 2.35 is 10.933 (μs). The same value is also confirmed by fitting the peak values to an exponentially decaying function (Figure 3.16).

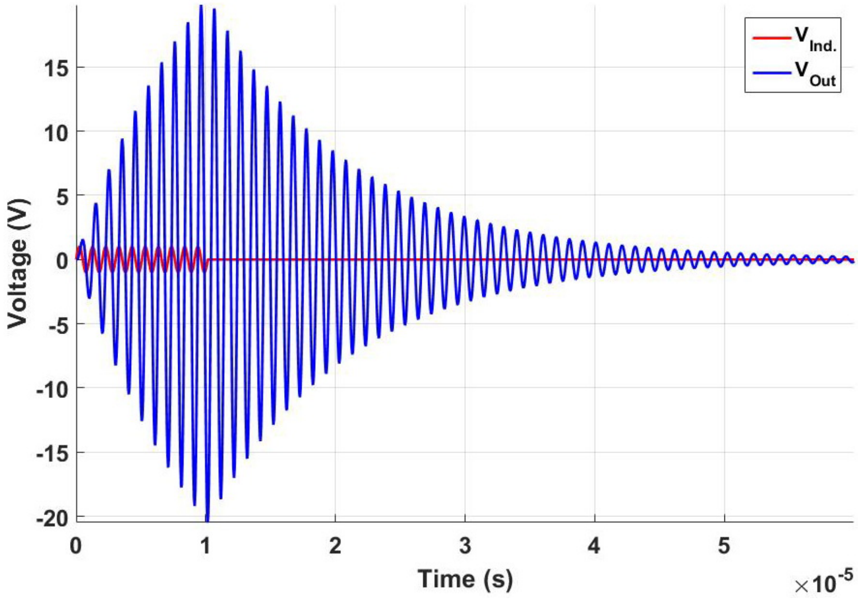

Figure 3.17: Induced sinusoidal signal (1(MHz), 10 periods and 1 (V) amplitude) versus output voltage.

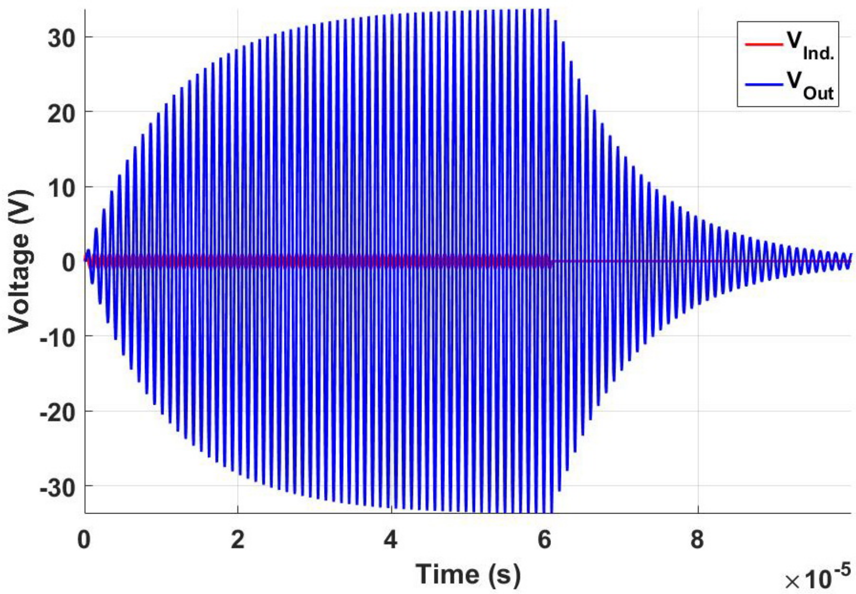

Figure 3.18: Induced sinusoidal signal (1(MHz), 60 periods and 1 (V) amplitude) versus output voltage.

From Figures 3.16, 3.17 and 3.18, one can conclude:

- To reach the steady state output voltage, $5\tau\ (s)$ is required.
- Discharging the coil takes 5τ (s).
- The output voltage at steady state is approximately equal to:

$$V_{Out}(w_0) \approx QV_{Ind.}(w_0)$$

  Thus, to increase the detectability of LFEIT signal signal, in spite of increasing ringing effects, resonance frequency of the coil sensor can matched to the LFEIT signal frequency.

- Time constant of the receiver coil sensor can effect the spatial resolution. Therefore, it's important to decrease the time constant of the receiver coil as much as possible. For this purpose, one may adjust the time constant of the sensor by the increasing resistance or/and decreasing the inductance of the receiver coil. However, these methods cause changes in the resonance frequency of the sensor and decrease the coil quality factor (undesirable).
- Response of the proposed coil sensors to the induced voltage variation at the transient period about 1.035 μs.

In the second step of simulation, resonance frequency of the coil Sensor II (its electrical properties are shown in the Table 3.12), is adjusted to 1.358 (MHz) in order to decrease ringing effect. Three 1 (V) induced sinusoidal voltage signals with 3, 10 and 60 periods are applied to the coil sensor (Figures 3.19, 3.20 and 3.21).

Table 3.12: Simulated electrical properties of the receiver coil Sensor II with SMA cable and 120 pF paralleled capacitance at resonance frequency.

R_{DC} (Ω)	C (pF)	L (μH)	R_{AC} (Ω)	f_r (MHz)	Quality Factor
1.2	178*	77	25	1.35	26.32

* Experimental data for capacitance is used. In addition, R_{AC} at 1 MHz for coil Sensor II is equal to 15 Ω.

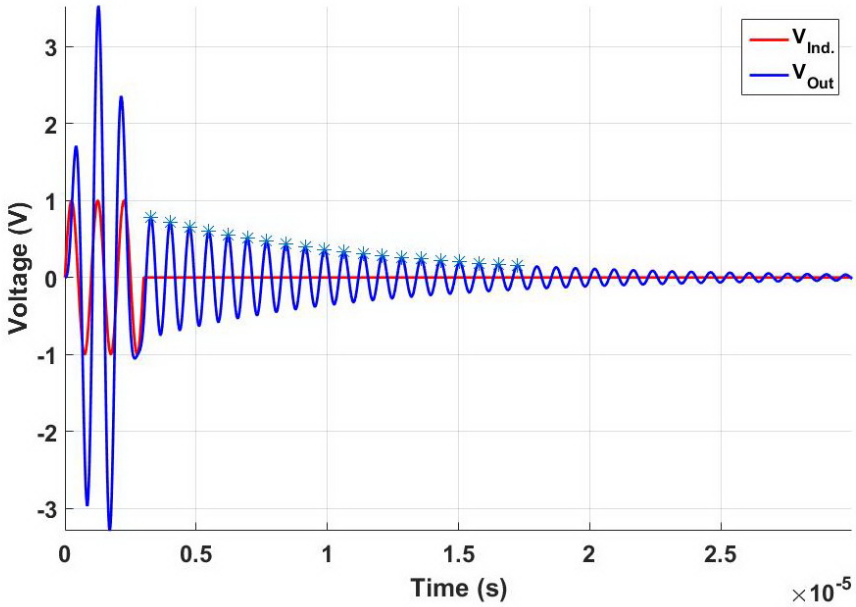

Figure 3.19: Induced sinusoidal signal (1(MHz), 3 periods and 1 (V) amplitude) versus output voltage (coil resonance frequency 1.358 is (MHz)).

As presented in Figures 3.19, 3.20 and 3.21, when the resonance frequency of the receiver coil is adjusted to 1.358 (MHz), the ringing effects decreases. But the amplitude of the output voltage signal is about 30 times (about quality factor of the coil sensor) less than previous simulation at the same condition. Therefore, the chance of LFEIT signal measurement is decreased. Consequently, this method is not a suitable technique for decreasing the ringing effect.

Conclusions:

- The measured LFEIT signal produced by applying an n periodic sinusoidal stimulus to the body, will have more than n pluses because of ringing effect.
- The LFEIT signal measurement, should be done in the resonance frequency of the receiver coil sensor.

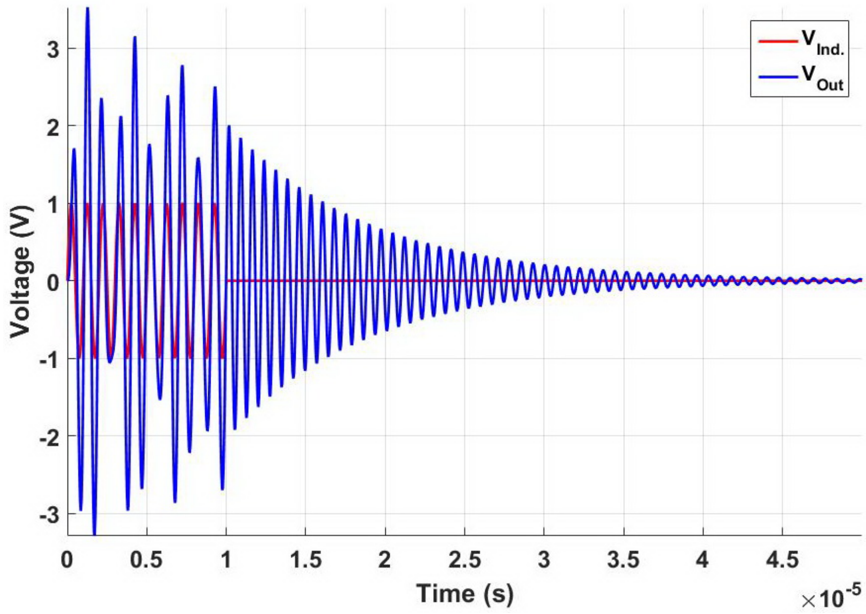

Figure 3.20: Induced sinusoidal signal (1(MHz), 10 periods and 1 (V) amplitude) versus output voltage (coil resonance frequency 1.358 is (MHz)).

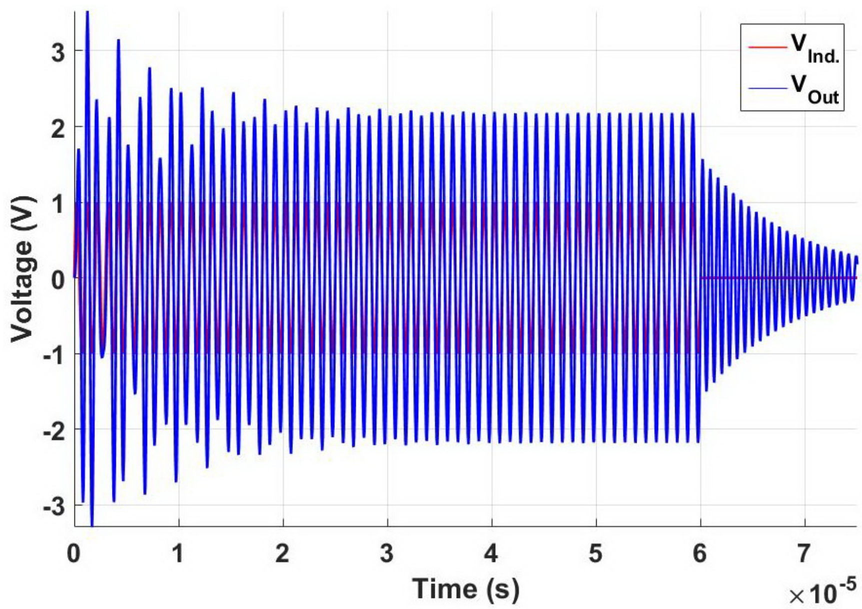

Figure 3.21: Induced sinusoidal signal (1(MHz), 60 periods and 1 (V) amplitude) versus output voltage (coil resonance frequency 1.358 is (MHz)).

3.4.5 Output Voltage versus Frequency on the Receiver Coil Sensor

Output voltage of the coil sensor is frequency dependent. At the resonance frequency of the coil sensor there is a peak at the output voltage. At the resonance frequency, induced voltage is multiplied by the quality factor of coil. To observe this behavior, output voltage of coil Sensor II is calculated from 800 kHz to 1.2 MHz in the simulation program (Figure 3.22).

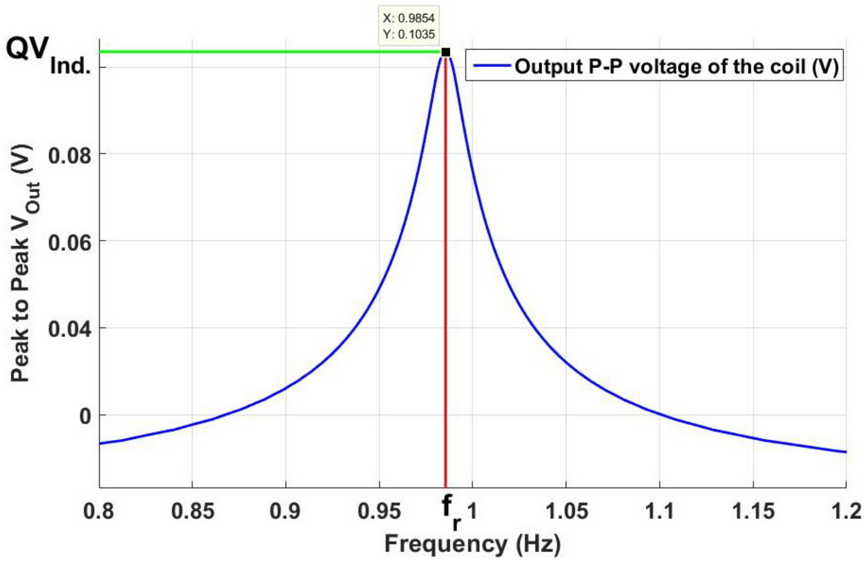

Figure 3.22: Output voltage V_{Out} versus frequency (Hz).

Quality factor and output voltage of the coil sensor at the resonance frequency is about 37.28 and 103.5 mV, respectively. Thus, the induced voltage on the receiver coil at the resonance frequency is about 2.77 mV.

CHAPTER 4

REALIZATION AND ASSESSMENT OF COIL SENSORS

4.1 Introduction

In this chapter, experiments are conducted to assess the performance of the designed receiver coil. A transmitter coil is designed to generate magnetic fields at the resonance frequency of the receiver coil. A measurement set up is constructed to position the transmitter and receiver coils coaxially. The magnetic fields generated at different distances are measured by the receiver coil. Electrical properties of the wound receiver coil sensors are measured. Finally, the effect of resistance R_{II} in the tuning circuit, on the quality factor of the designed coil is presented.

4.2 Realization of Disk Multiple Layer Transmitter Coil

As it mentioned in the section 3.2, it is necessary to design a transmitter coil to generate a calibration signal for the receiver coil. For this purpose, first the physical dimensions of this coil are set by the simulation program (Table 3.1). The physical dimensions of the realized (wound) coil sensor (Figure 4.1), are presented in Table 4.1. The electrical characteristics of the transmitter coil are also presented in Table 4.2. Transmitter coil is connected by an SMA cable to the driver circuit of transmitter. This cable, however, changes the electrical characteristics of the transmitter coil, since SMA cable has its own resistance, capacitance and inductance values. The electrical characteristics after this modification is shown in Table 4.3.

Figure 4.1: Wound transmitter coil.

Table 4.1: Physical properties of the transmitter coil.

Inner Diameter (cm)	Outer Diameter (cm)	Length (cm)	Wire Diameter (cm)	Turn Number	Layer Number	Conductor Resistivity (Ωm)
3.28	3.65	2.25	0.95	45	2	16.78e-9

Table 4.2: Electrical properties of the transmitter coil at resonance frequency.

R_{DC} (Ω)	C (pF)	L (μH)	R_{AC} (Ω)	f_r (kHz)	Quality Factor	f_{3dB} (kHz)
0.13	138	51.5	18	1880	34.5	54

Table 4.3: Electrical properties of the transmitter coil with SMA cable at resonance frequency.

R_{DC} (Ω)	C (pF)	L (μH)	R_{AC} (Ω)	f_r (kHz)	Quality Factor	f_{3dB} (kHz)
0.15	214	62.19	13.28	1378.96	40.55	34

From Tables 4.2, 4.3 and phase of coil impedance at 1 MHz (Table 4.4), one can conclude that the transmitter coil is operating at the inductance region.

In order to drive the transmitter coil, a driver (an electronic power amplifier) circuit is designed (Figure 4.3) as mentioned in Section 3.3. At 1 MHz, the transmitter coil has electrical characteristics (measured by an LCR meter Agilent E4980A) as shown in Table 4.4. Driving current (1 MHz) of 35 mA RMS is applied to the transmitter coil. The resultant magnetic field is measured by the receiver coil Sensor II (Figure 4.2) at different distances.

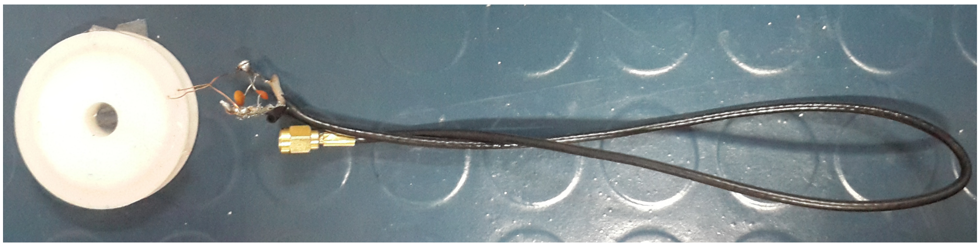

Figure 4.2: Receiver Coil II.

Figure 4.4 shows the measurement set up constructed for this purpose. The position of the receiver coil can be changed coaxially. For each position of the coil, digital oscilloscope output (obtained by averaging 128 measurements) is recorded. The measured and calculated mean magnetic flux density along the transmitter/receiver coil axis are shown in Figure 4.5. The percentage errors between the calculated and measured magnetic field are presented in Figure 4.6. The percentage error between the measured and simulated data is evaluated by:

$$\%Error = \frac{|Measured - Calculated|}{Calculated} \times 100$$

At distances that transmitter and receiver coils are nearby to each other, the measured data are affected by mutual coupling. But when the distance increases, mutual coupling decreases and then the error becomes less than 10%. Eventually, as the distance increases magnetic field decreases, and error increases due to noise in the measure-

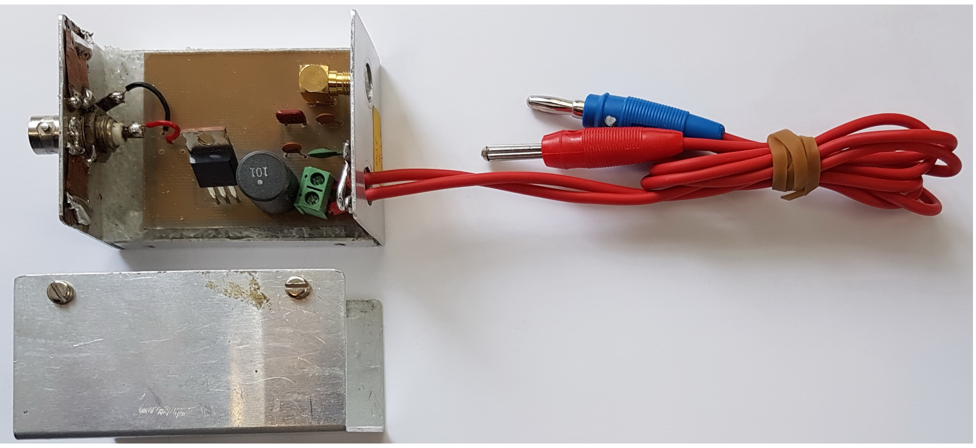

Figure 4.3: Transmitter driver circuit (circuit diagram is presented in Figure 3.2).

Table 4.4: Electrical Characteristics of transmitter coil with SMA cable at 1 MHz.

R_s (Ω)	L_s (μH)	$\|Z\|$ at 1 MHz (Ω)	$\angle Z$ at 1 MHz ($^\circ$)
11.57	76.09	478.3	88.62

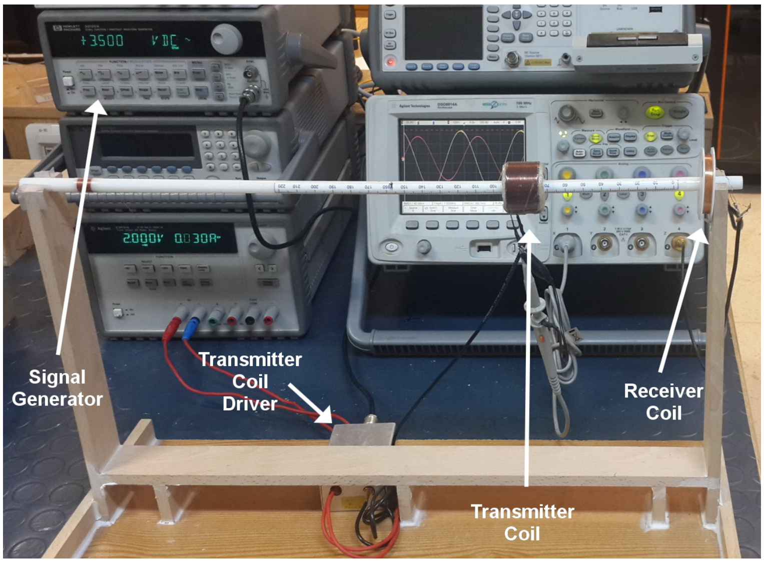

Figure 4.4: Magnetic field versus distance measurement setup.

ments.

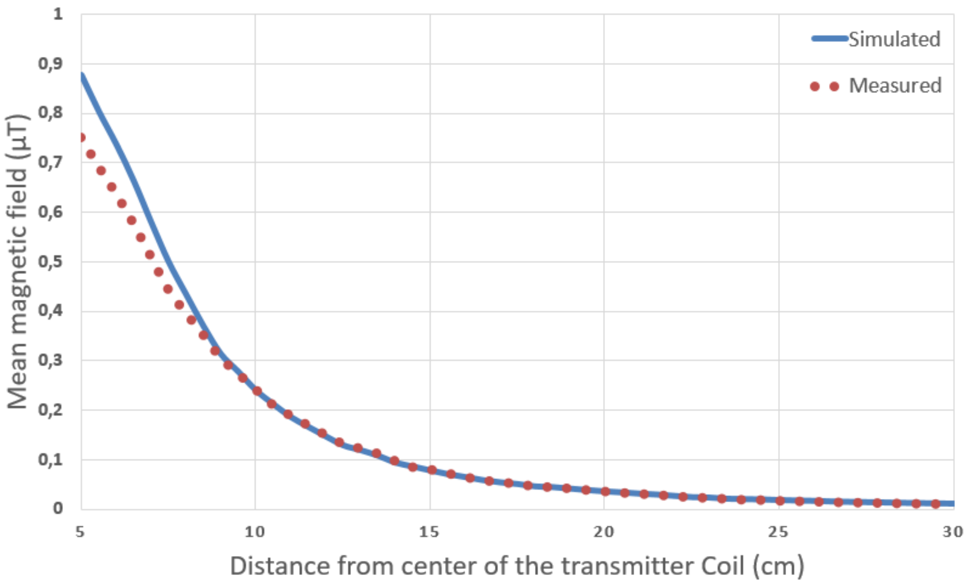

Figure 4.5: Simulated and measured magnetic field versus distance (by receiver coil Sensor II).

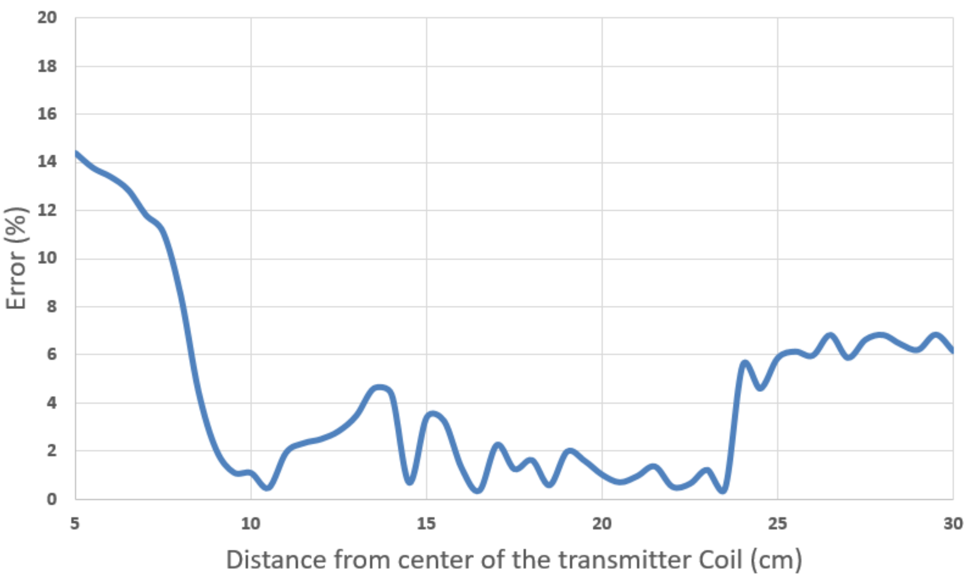

Figure 4.6: Error between simulated and measured magnetic field versus distance (by receiver coil Sensor II).

4.3 Characteristics of the Designed Disk Multiple Layer Coil Sensors

Due to experimental conditions, such as operating frequency and space consideration between the magnets, several restrictions for coil sensor design should be considered (Figure 4.7):

- Air cored search coils are implemented since there is a strong static magnetic field.
- The resonance frequency of the coil sensors are adjusted to match the operating frequency (1 MHz) of the ultrasound transducer.
- Coil dimensions are restricted by the permanent magnet configuration.
- Coil dimensions are also adjusted to measure LFEIT signals originating from a region where the static magnetic field is fairly homogeneous.

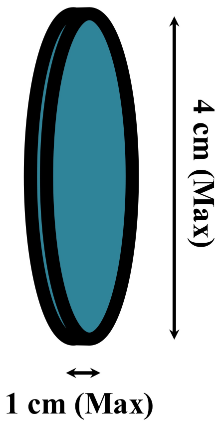

Figure 4.7: Dimensional restrictions for coil sensor design.

To measure low-frequency and low intensity magnetic fields, several receiver coils are wound and tested by network analyzer (Keysight Field Fox N9915A), LCR meter (Agilent E4980A), oscilloscope (Agilent DSO6014A), data acquisition card (GaGe Oscar 4327) and digital multimeter (Agilent 34410A). The digital multimeter is used to measure the R_{DC} of the receiver coils. Physical dimensions of coils are measured by the Wert calliper. The receiver coil sensor's output voltage after amplification is measured by the oscilloscope and data acquisition card. The electrical properties of two coils are found suitable for LFEIT experiments (coil Sensor I and II). In this section, the electrical characteristics of these coils are presented.

Coil Sensor I:

The physical and winding properties of the receiver coil obtained by the design tool are presented in Table 3.7 and Table 3.8, respectively. The physical properties of the coil after winding is shown in Table 4.5. The percentage error in the coil outer diameter is found less than 0.01 %, whereas there is about 17 % error in the coil length. Coil sensor I is presented in Figure 4.8.

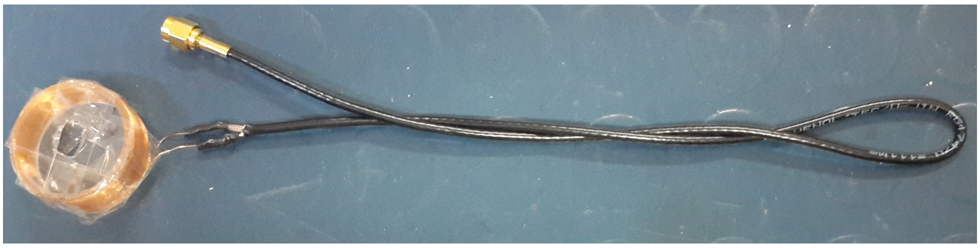

Figure 4.8: Receiver Coil I.

Table 4.5: Measured physical properties of the wound receiver coil Sensor I.

Inner Diameter (cm)	Outer Diameter (cm)	Length (cm)	Wire Diameter (cm)	Turn Number
3.51	3.63	1.05	0.31	55

The R_{DC} of coil Sensor I is measured as 1.73 Ω by using a digital multimeter. The error between the measured and simulated DC resistance is about 6.12 $\%$. Induced voltage $V_{Ind.}$, output voltage V_{Out}, thermal noise V_{Th}, sensitivity S and SNR of the coil Sensor I are presented in Table 4.6:

Table 4.6: Induced and output voltages, thermal noise, sensitivity and SNR of receiver coil Sensor I.

Magnetic Field (pT)	Bandwidth (kHz)	$V_{Ind.}$ (μV)	Q	V_{Out} (μV)	V_{Th} (nV)	S $n\frac{V}{Hz\frac{A}{m}}$	SNR dB
10	34.5	3.46	29	100.42	44.42	477.35	41.64

If the thermal noise V_{Th} is assumed to be the only noise source for coil Sensor I, the minimum detectable magnetic field by Sensor I will be about 0.128 pT. Electrical properties of the coils can be measured by network analyzer or LCR meter by methods that are mentioned previously (section 2.1.9). The results of the measured electrical characteristics obtained by these two devices should confirm each other.

- **Measurement by Network Analyzer**:

  Electrical properties of coil Sensor I measured by using the network analyzer is presented in Table 4.7.

Table 4.7: Measured electrical properties of the receiver coil Sensor I by network analyzer.

C (pF)	L (μH)	R_{AC} (Ω)	f_r (kHz)	Quality Factor
182.01	132.68	29.13	1024.13	29.30

The measured AC resistance R_{AC} and inductance L values are compared with the calculated values (Table 4.8). Since the calculations can be obtained using two different formulations, it is also possible to check the accuracy in these formulations. It is observed that equation (2.21) provides better estimates for the AC resistance, and equation (2.24) provides better estimates for the inductance value. The differences between the measured and calculated values for the resonance frequency and quality factor are given in Table 4.9.

Table 4.8: The percentage error between the measured and calculated electrical properties of coil Sensor I. Measurements are obtained using network analyzer.

$\% E_L$ (eq. 2.23)	$\% E_L$ (eq. 2.24)	$\% E_{R_{AC}}$ (eq. 2.20)	$\% E_{R_{AC}}$ (eq. 2.21)
16.58	15.87	52.55	0.65

Table 4.9: The percentage error between the measured and calculated properties of coil Sensor I. Resonance frequencies and quality factors are compared. Measurements are obtained using network analyzer.

$\% E_{f_r}$ (eq. 2.43)	$\% E_{f_r}$ (eq. 2.48)	$\% E_{f_r}$ (eq. 2.50)	$\% E_Q$ (eq. 2.41)
8.62	8.57	8.58	9.42

- **Measurement by LCR Meter**:

The electrical properties of coil Sensor I measured by the LCR meter are presented in Table 4.10. These values, have good agreement with the measured data obtained by the network analyzer. The error between the simulated and measured data are presented in the Tables 4.11 and 4.12.

Table 4.10: The electrical properties of the receiver coil Sensor I measured by LCR meter.

C (pF)	L (μH)	R_{AC} (Ω)	f_r (kHz)	Quality Factor
185.68	132.15	28.89	1016	29.19

Table 4.11: Percentage error the between the measured and simulated electrical properties of coil Sensor I. Measurements are obtained using LCR meter.

% E_L (eq. 2.23)	% E_L (eq. 2.24)	% $E_{R_{AC}}$ (eq. 2.20)	% $E_{R_{AC}}$ (eq. 2.21)
16.91	16.21	51.29	1.47

Table 4.12: The percentage error between the measured and calculated properties of coil Sensor I. Resonance frequencies and quality factors are compared. Measurements are obtained using the LCR meter.

% E_{f_r} (eq. 2.43)	% E_{f_r} (eq. 2.48)	% E_{f_r} (eq. 2.50)	% E_Q (eq. 2.41)
7.76	7.71	7.72	9.75

Receiver Coil Sensor II:

The physical properties of the receiver coil obtained by the design tool are presented in Table 3.2. The physical properties of the coil after winding is shown in Table 4.13. The percentage error in the coil outer diameter is found less than 0.4 %, whereas there is about 12.9 % error in the coil length. Measured winding properties shown in Table 4.14 exactly match to the simulated properties.

Table 4.13: Measured physical properties of the realized coil Sensor II.

Inner Diameter (cm)	Outer Diameter (cm)	Length (cm)	Wire Diameter (cm)	Conductor Resistivity (Ωm)
4.1	4.23	0.595	0.31	16.78e-9

The resistance R_{DC} of coil Sensor II is measured as 1.12 Ω by the digital multimeter. The error between the measured and simulated DC resistance is about 1.37 $\%$.

Table 4.14: Winding properties of the realized coil Sensor II.

Layer Number	Turn per Odd Layers	Turn per Even Layers	Number of Turns	Pacing Factor
2	17	16	33	$\frac{\pi}{2\sqrt{3}}$

Induced voltage $V_{Ind.}$, output voltage V_{Out}, thermal noise V_{Th}, sensitivity S and SNR of the coil Sensor II are presented in Table 4.15:

Table 4.15: Induced and output voltages, thermal noise, sensitivity and SNR of receiver coil Sensor II.

Magnetic Field (pT)	Bandwidth (kHz)	$V_{Ind.}$ (μV)	Q	V_{Out} (μV)	V_{Th} (nV)	S $n\frac{V}{Hz\frac{A}{m}}$	SNR dB
10	61.5	2.82	28.9	81.14	33.83	392.72	39.32

If the thermal noise V_{Th} is assumed to be the only noise source for coil Sensor II, the minimum detectable magnetic field by Sensor II will be about 0.17 pT. Electrical properties of coil Sensor II are measured by both network analyzer and LCR meter.

- **Measurement by Network Analyzer**:

  The electrical properties of coil Sensor II measured by the network analyzer is presented in Table 4.16.

  The AC resistance R_{AC} and inductance L values measured by the network analyzer are compared with the calculated values (Table 4.17). Since the calculations can be obtained using two different formulations, it is also possible

Table 4.16: Electrical properties of coil Sensor II measured by network analyzer.

C (pF)	L (μH)	R_{AC} (Ω)	f_r (kHz)	Quality Factor
106.51	75.96	29.31	1769.35	28.77

to check the accuracy in these formulations. It is observed that equation (2.21) provides better estimates for the AC resistance, and equation (2.24) provides better estimates for the inductance value. The differences between the measured and calculated values for the resonance frequency and quality factor are given in Table 4.18.

Table 4.17: The percentage error between the measured and calculated electrical properties of coil Sensor II. Measurements are obtained using network analyzer.

% E_L (eq. 2.23)	% E_L (eq. 2.24)	% $E_{R_{AC}}$ (eq. 2.20)	% $E_{R_{AC}}$ (eq. 2.21)
8.81	7.55	69.82	1.01

Table 4.18: The percentage error between the measured and calculated properties of coil Sensor II. Resonance frequencies and quality factors are compared. Measurements are obtained using network analyzer.

% E_{f_r} (eq. 2.43)	% E_{f_r} (eq. 2.48)	% E_{f_r} (eq. 2.50)	% E_Q (eq. 2.41)
4.78	4.72	4.73	5.42

- **Measurement by LCR Meter**:

The electrical properties of coil Sensor II measured by LCR meter are presented in Table 4.19. These values, have good agreement with the measured data obtained by the network analyzer.

Table 4.19: The electrical properties of coil Sensor II measured by LCR meter.

C (pF)	L (μH)	R_{AC} (Ω)	f_r (kHz)	Quality Factor
108.93	74.81	28.67	1763	28.91

The error between the simulated and measured data are presented in the Tables 4.20 and 4.21.

Table 4.20: Percentage error between the measured and simulated electrical properties of coil Sensor II. Measurements are obtained using the LCR meter.

$\%\ E_L$ (eq. 2.23)	$\%\ E_L$ (eq. 2.24)	$\%\ E_{R_{AC}}$ (eq. 2.20)	$\%\ E_{R_{AC}}$ (eq. 2.21)
10.19	8.95	66.13	3.15

Table 4.21: The percentage error between the measured and calculated properties of coil Sensor II. Resonance frequencies and quality factors are compared. Measurements are obtained using the LCR meter.

$\%\ E_{f_r}$ (eq. 2.43)	$\%\ E_{f_r}$ (eq. 2.48)	$\%\ E_{f_r}$ (eq. 2.50)	$\%\ E_Q$ (eq. 2.41)
4.41	4.34	4.36	5.01

Measured electrical properties of the coil Sensor II have discrepancy with the estimated electrical characteristics due to the discrepancy in physical properties, approximations at the analytic formulation, parasitic signals, error of measurement devices and etc. However, electrical characteristics of coil Sensor II are adjusted by adding SMA cable and a parallel connected 200 pF capacitance to the sensor. The adjusted electrical properties are shown in Table 3.5.

4.4 Output Voltage versus Frequency on the Receiver Coil Sensor

Resonance frequency of coil Sensor II (physical, winding and electrical characteristics are shown in the Tables 4.13, 4.14 and 3.5), is adjusted to 994.31 kHz. As it mentioned previously, the measured output voltage on the receiver coil (from Phantom II) at the resonance frequency is quality factor times the induced voltage. To investigate the above property, the signal's frequency on the transmitter coil is swept from 800 to 1200 kHz. The parameters related to the coil configuration of this measurement is given in Table 4.22. The measured voltage at the output of receiver coil is shown in Figure 4.9. As it presented in figure, at the resonance frequency of the receiver coil, there is a peak in the measured output voltage. The output peak to peak voltage at the resonance frequency is about 106.1 mV. Then, the induced voltage at the receiver coil is about 3.1 mV (since quality factor is 34.5).

Table 4.22: The transmitter/receiver coil set up to obtain the frequency response of the receiver coil Sensor II.

Center to Center Distance (cm)	Resonance Frequency of the Transmitter Coil (MHz)	Transmitter Peak to Peak Voltage (mV)	Quality Factor of the Receiver Coil
10	1.37	500	34.52

4.5 Tuning Circuit of Receiver Coil Sensor

In the previous sections 3.2 and 3.4.4, effect of paralleled capacitance on the self resonance frequency manipulation are presented. From the results, can conclude that only coil sensor's resonance frequency decreasing is possible by adding paralleled capacitance to the output of receiver coil. In this section, receiver coil IV that it's physical, winding and electrical characteristics are presented in the Tables 4.23, 4.24, 4.25 respectively, in order to investigate paralleled resistance R_{II} plateau effect on the S_{21} parameter (then on the coil sensor's output voltage V_{Out} and output impedance of

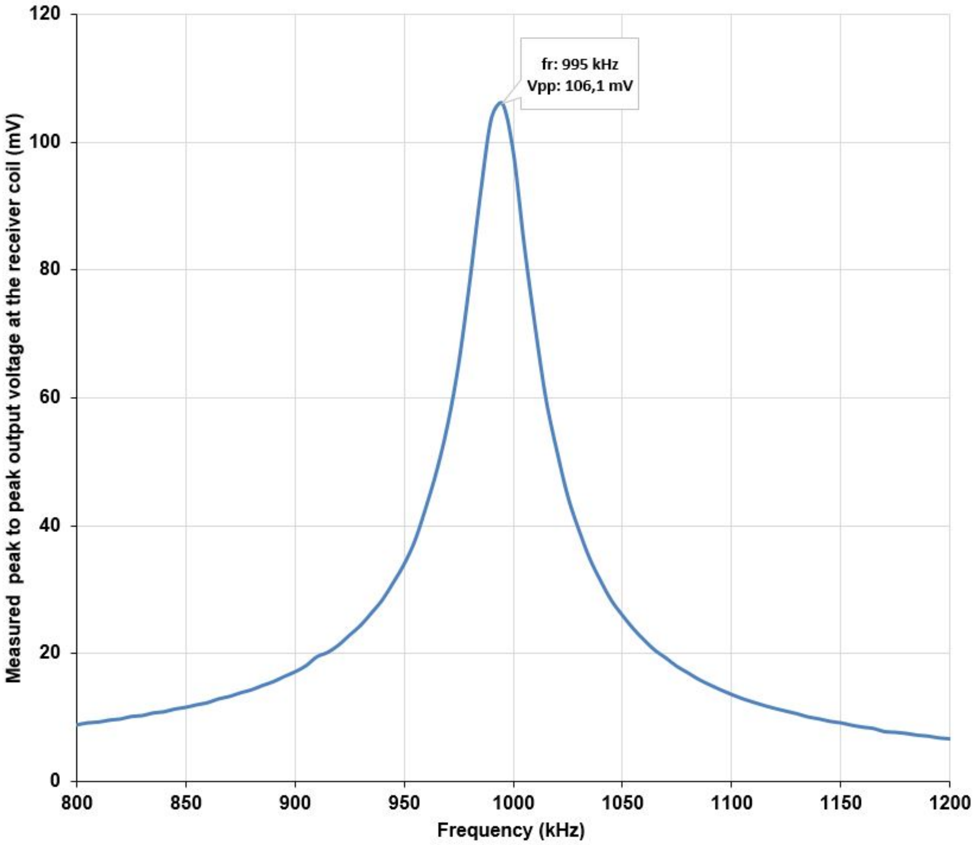

Figure 4.9: Measured peak to peak V_{Out} (mV) of the receiver coil versus frequency (kHz)

the coil) is selected.

Table 4.23: Measured physical properties of the receiver coil Sensor IV.

Inner Diameter (cm)	Outer Diameter (cm)	Length (cm)	Wire Diameter (cm)	Conductor Resistivity (Ωm)
4.1	4.32	0.53	0.31	16.78e-9

Table 4.24: Winding properties of the wound receiver coil Sensor IV.

Layer Number	Turn per Odd Layers	Turn per Even Layers	Number of Turns
4	17	16	66

Table 4.25: Measured electrical properties of the receiver coil Sensor IV.

Measurement Device	C (pF)	L (μH)	R_{AC} (Ω)	f_r (kHz)	Quality factor	S_{21} (dB)
Network analyzer	73.78	302.45	81.01	1065.39	24.99	-54.06
LCR meter	74.83	304.71	80.41	1054	25.09	-

A resistance R_{II} that is equal to 1.199 $k\Omega$ is paralleled to receiver coil IV. The lower and upper corners of the bandwidth are 671.23 and 1793.78 kHz (equations 2.62 and 2.63), respectively. In addition, the ζ is equal to 0.067556 (equation 2.64). As it presented in Figures 4.10(a) and 4.10(b), by adding R_{II} paralleled to the receiver coil a plateau is generated at the S_{21} parameter. In that case, the electrical characteristic of the receiver coil IV are presented in the Table 4.26.

The S_{21} parameter at the narrowband case is measured more accurately by the network analyzer.

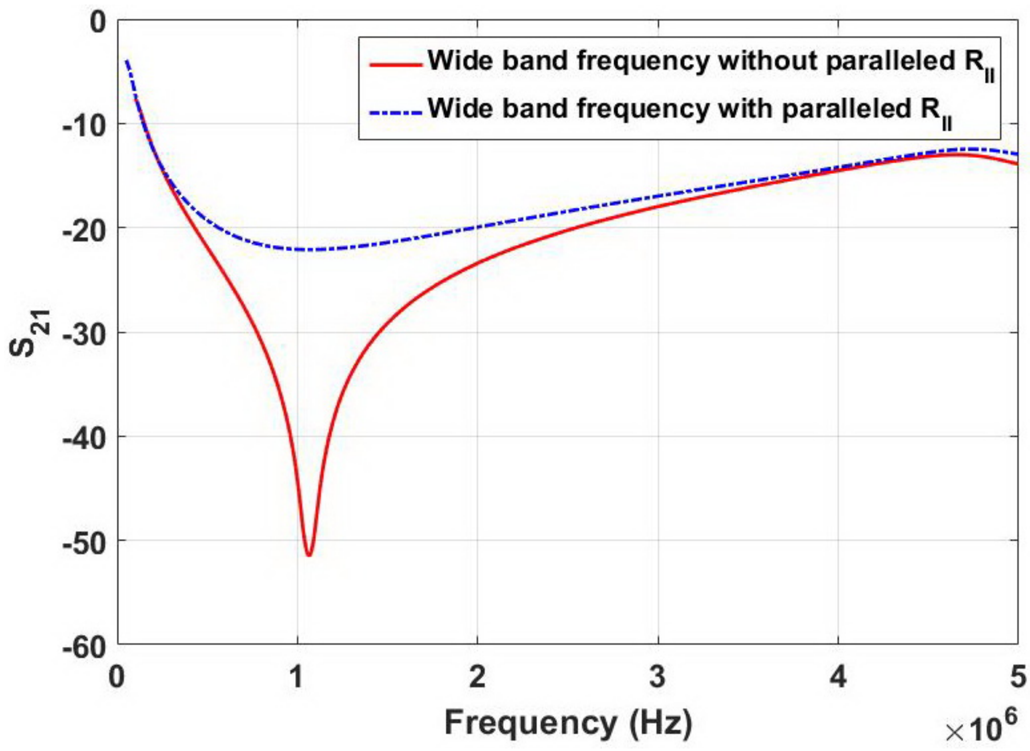

(a) Wideband of the S_{21} parameter.

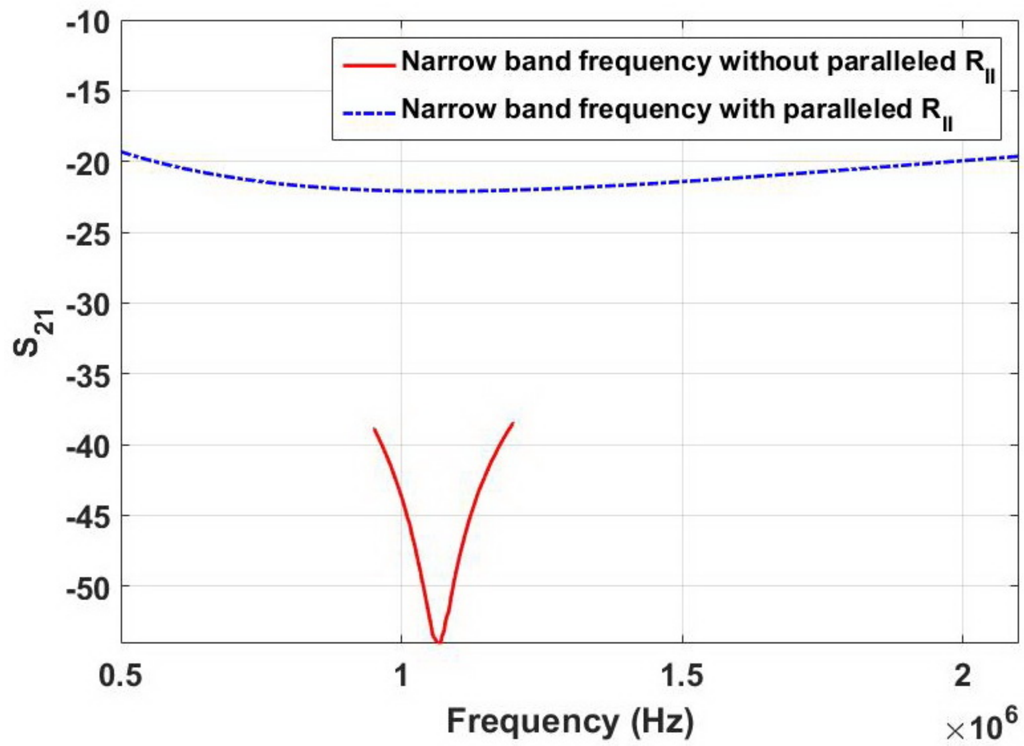

(b) Narrowband of the S_{21} parameter.

Figure 4.10: S_{21} parameter versus frequency.

Table 4.26: Measured electrical properties of the receiver coil Sensor IV.

Measurement Device	f_r (kHz)	f_{3dB} (kHz)	Quality factor	S_{21} (dB)
Network analyzer	1064.54	822.55	0.95	-22.11

From Table 4.26, one can conclude that by adding R_{II} resistance parallel to the receiver coil, it's quality factor decreases tremendously (disadvantage of this scenario). But, bandwidth of the receiver coil increases. At the bandwidth range, S_{21} parameter is approximately fixed and have stable behaviour.

CHAPTER 5

EXPERIMENTS FOR LFEIT SIGNAL ACQUISITION

5.1 Introduction

In this chapter, first the permanent magnet configuration used for static magnetic field generation is introduced. Next, the properties of the custom made two stage amplifier are presented. Various phantoms used for LFEIT experimental studies are then introduced. Figure 5.1 shows the experiment setup used the experimental studies. In this set up, coil Sensor II is employed to measure the magnetic fields. The LFEIT signals measured from Phantoms I, II, III and IV are displayed. Finally, LFEIT images generated from Phantom IV are presented together with B-scan ultrasound images.

5.2 Static Magnetic Field Generation for LFEIT Experiments

LFEIT experiments are conducted by placing phantoms inside a static magnetic field. To increase the LFEIT signal amplitude, the magnitude of the generated magnetic field should be maximized. For this case, 6 neodymium magnets with N45 grade (Figure 5.2) are used with a U-shape iron core. Iron core concentrates the magnetic field and make it fairly homogeneous between the magnets (Figure 5.3). The measured inhomogeneous magnetic field at the center of magnets (distance between magnets is 6.4 cm, then measurement of magnetic field is done at 3.2 cm) is presented in Figure 5.4 (measured by 5180 Gauss/Tesla meter). This figure presents that magnetic field nearby the center of magnets is approximately homogeneous. The maximum

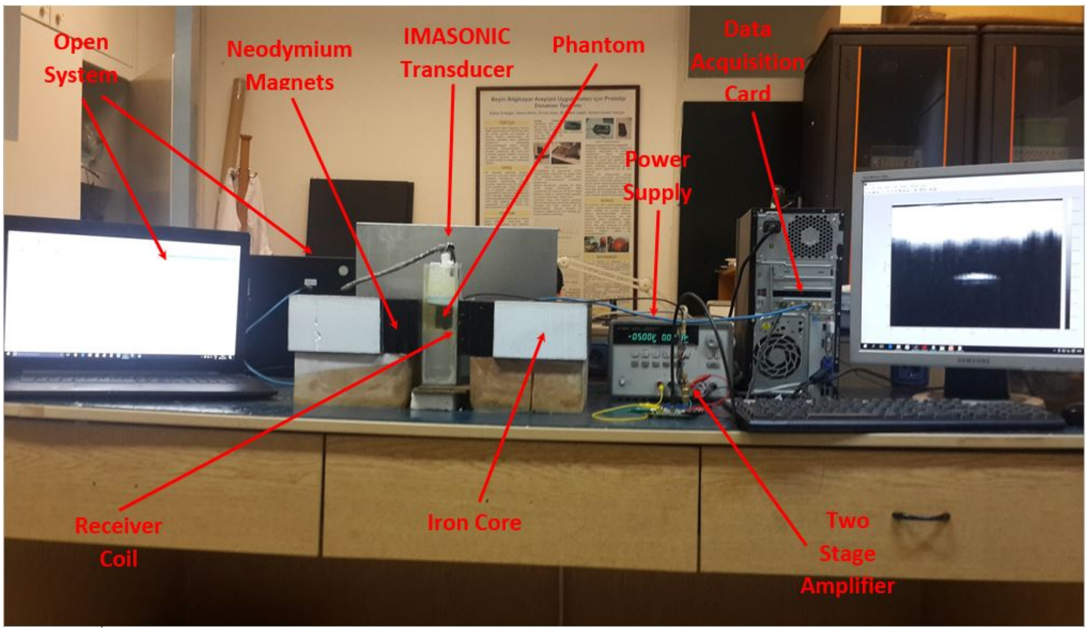

Figure 5.1: LFEIT experiment setup.

magnetic field at the center of magnets is measured as 0.56 T (Figure 5.4) [1].

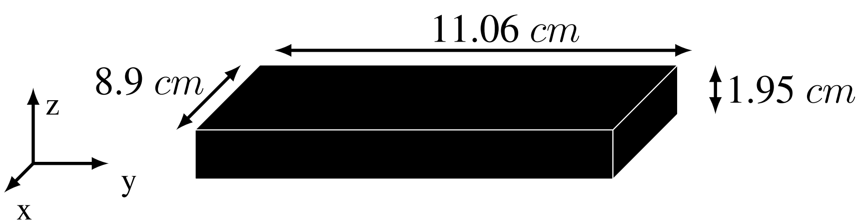

Figure 5.2: Neodymium magnets' dimensions

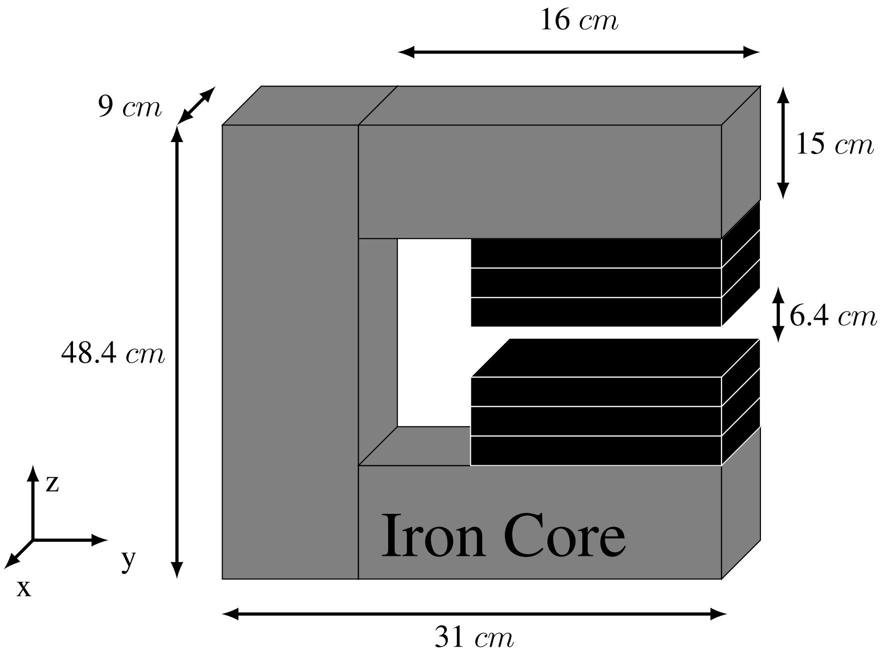

Figure 5.3: Magnets setup with iron core.

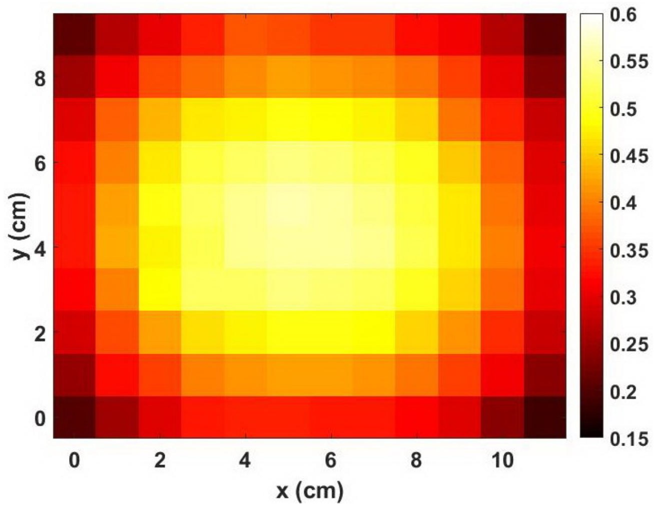

Figure 5.4: Generated magnetic field distribution in the central plane. Neodymium magnets (grade N45) are used for magnetic field generation [1].

5.3 LFEIT Signal Amplification

LFEIT signal's amplitude is quite low (nV-μV). A high gain, low noise amplifier should be used for signal amplification. Since the signal frequency is 1 MHz, the amplifier's bandwidth should be large enough to provide a gain at 1 MHz. Moreover, by considering use of coil sensors at the resonance frequency, it is preferable to utilize voltage amplifiers which have high input impedance.

5.3.1 The Voltage Amplifier Used in LFEIT Experiments

To obtain high gain, one can employ cascaded amplifiers. The total gain of the two-stage cascaded amplifier is adjusted to be 100 dB. The gain of the pre-stage and second stage amplifiers are set to be 52 and 48 dB, respectively.

5.3.1.1 Pre-Stage Amplifier

Pre-stage amplifier should have ultra low input referred noise and high input impedance. In addition, it should have higher gain compared to the second stage amplifier. For the pre-stage amplification, OP27 is used a buffer [41] and ADA4817 Op-Amp is used [42] as a simple non-inverting amplifier (Figure 5.5).

The OP27 Op-Amp has the following characteristics:

- Low input referred noise: 3 $nV/\sqrt{Hz}$.
- High input impedance: more than 4 $M\Omega$ at 1 MHz ($Z_{in} \gg Z_{Coil}$).
- 8 MHz gain bandwidth product.
- Low offset voltage at the output of Op-Amp: 10 μV.

It is concluded that for LFEIT experiments OP27 is suitable as a buffer.

The operational amplifier ADA4817 used for the gain stage has the following characteristics:

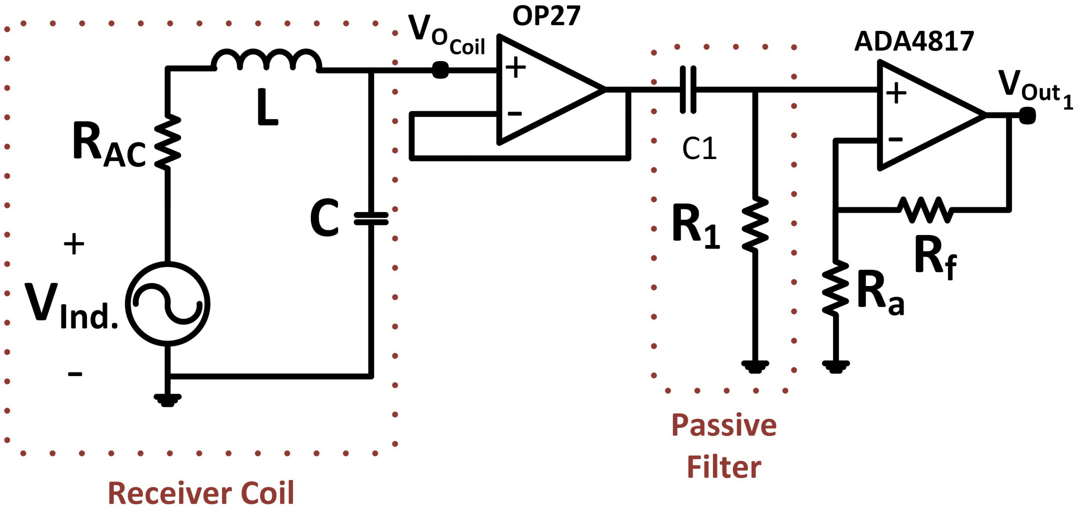

Figure 5.5: Pre-stage amplifier (buffer (OP27), filter and non-inverting amplifier (ADA4817)) is connected to the receiver coil sensor output.

- Low input referred noise: 4 $nV/\sqrt{Hz}$ and 2.5 $fA/\sqrt{Hz}$.
- High input impedance: more than 500 $G\Omega$ at 1 MHz.
- 52 dB gain at 1 MHz frequency.
- Low offset voltage at the output of Op-Amp: 2 mV maximum.

The gain of this stage is simply as follows:

$$\text{Voltage gain} = \frac{V_{Out_1}}{V_{O_{Coil}}} = 1 + \frac{R_f}{R_a} \tag{5.1}$$

The noise characteristics of ADA4817 Op-Amp without considering noise of the receiver coil sensor, OP27 and resistance R_1 of the passive filter are shown in Table 5.1.

Receiver coil Sensor II at the resonance frequency presents 18 $k\Omega$ impedance. Consequently, the RMS input voltage noise and minimum detectable signal for the ADA4817 amplifier are 6.28, 8.87 μV, respectively.

Table 5.1: Noise characteristic of ADA4817.

Unity frequency (MHz)	Amplifier bandwidth (MHz)	R_f ($k\Omega$)	R_a (Ω)	Gain (dB)	Input volt. noise (RMS) (μV)	Min. detectable signal (RMS) (μV)
410	1.02	4.7	11.7	400	5.09	7.19

For output voltage V_{Out} of the coil sensor that is more than 8.87 μV (for magnetic field that is more than 10.5 pT), amplified signal of pre-stage amplifier will be accurate (quality factor of the coil is supposed 3).

5.3.1.2 Second Stage Amplifier

For the second stage, AD8332 evaluation board (which is a dual channel ultra low noise linear-in-dB variable gain amplifier from Analog Devices) is selected. Properties of this evaluation board are given below [2, 3]:

- Ultra Low Noise Amplifier
  - Input Referred Voltage Noise: 0.74 $nV/\sqrt{Hz}$
  - Input Referred Current Noise: 2.5 $pA/\sqrt{Hz}$
- 3 dB Bandwidth: 100 MHz
- Adjustable Input Impedance from 50 Ω up to 6 $k\Omega$
- Programmable Wide Gain Range amplifier
  - -4.5 dB to +43.5 dB in LO Gain Mode
  - 7.5 dB to 55.5 dB in HI Gain Mode
- Single 5 V Supply Operation

In Figures 5.6(a) and 5.6(b) the frequency response vs. gain and top view of the evaluation board of AD8332 are presented, respectively. As shown in Figure 5.6(a), at 1 MHz frequency 55.5 dB gain (plateau and stable) can be reached.

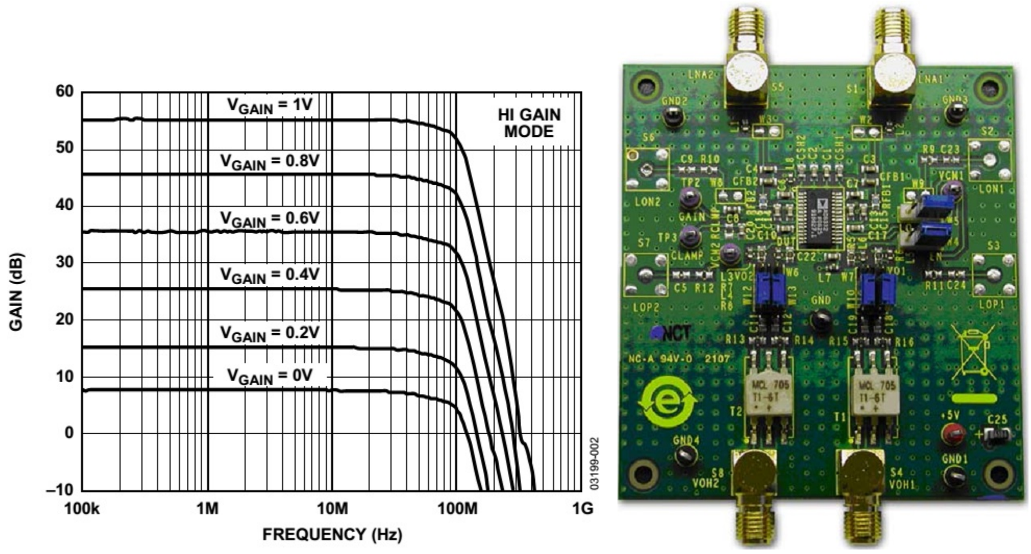

(a) (b)

Figure 5.6: Second stage amplifier. (a) The frequency response of AD8332 for different gain values [2]. (b) Top view of AD8332 evaluation board [3].

One can calculate the noise floor of amplifier as 0.6 μV (RMS) or -124.52 dB. Then, minimum detectable signal for this amplifier is -121.52 dB. Consequently, a signal of 0.84 μV (RMS) is definitely detectable by the amplifier (1.02 MHz bandwidth is supposed). Note that, the RMS output of the pre-stage amplifier (3.55 mV) is higher than the minimum detectable signal of the second stage amplifier (0.84 μV).

5.4 Phantom Properties

In this thesis study, four phantoms are prepared to mimic bodies with inhomogeneous conductivities. Preparation of these phantoms are explained below [43, 44]:

- Phantom I:

  This phantom is composed of five layers. First layer is sun flower oil whose conductivity is approximately 0 S/m. Second layer is a solder disk (2 cm diameter, height is negligible) whose conductivity and acoustic velocity are about 8 MS/m and 5120 m/s, respectively. Third layer is an agar-gelatin phantom which has a conductivity of about 0.125 S/m. Below the agar-gelatin phantom, glass beads whose conductivity is approximately zero S/m are used for absorption of ultrasound wave (fourth layer). The fifth layer is a layer of paper tissues. The dimensions of the layers are presented in Figure 5.7(a). The composition of the agar-gelatin phantom is presented in the Table 5.2. The method of phantom preparation is as follows:

– Agar, gelatin and water is mixed in glass beaker.

– Mixture is heated until 80 $°C$.

– The heated mixture is poured in a phantom tube.

– The mixture in the phantom tube becomes solid after two hours.

– Finally, the solder disk is placed on the agar-gelatin phantom

Table 5.2: Amount of materials in the agar-gelatin phantom shown in Figure 5.7(a).

Materials	Amount
Water	100 ml
Agar	1.5 gr
Gelatin	3 gr

- Phantom II:

Phantom II is made by putting graphite bar (0.5 cm diameter, 0.5 cm height) instead of solder disk in Phantom I (Figure 5.7(b)). The graphite bar's conductivity and acoustic velocity are 800-3000 S/m and 4170 m/s [45], respectively. Figure 5.7(b) shows the dimensions of the phantom.

- Phantom III:

Aim of this phantom preparation is to measure the lowest conductivity difference. This phantom is composed of two layers. First layer is sun flower oil. Sun flower oil's conductivity is about 0 S/m. Second layer is 15 $\%$ hydrochloric acid solution. The electrical conductivity of the solution approximately 70 S/m. The relative sizes of the oil and solution are presented in Figure 5.7(c).

- Phantoms IV:

  Phantom IV has a composition same as Phantom II. It is made inside of a cuboid by putting the graphite bar at the corner on the boundary (Figure 5.7(d)). This phantom is utilized when the ultrasound waves at different angles are applied. The steered ultrasound waves introduce LFEIT signals at specific angles the inhomogeneity (graphite bar) exists. Measured LFEIT signals are used to construct an image which shows the inhomogeneity in the phantom.

Phantoms properties:

Phantom I and Phantom II include solder disk and graphite bar. Solder disk and graphite bar are chosen since they have high electrical conductivities. However, they also have high acoustic impedances (higher than oil and agar-gelatin). Consequently, acoustic pressure waves do not penetrate through these materials. A material with high conductivity and low acoustic impedance is explored but can not be found in this thesis study.

5.5 LFEIT Signal Measurement from Phantom I

In the first experimental study, Phantom I is selected (Figure 5.8). Since the conductivity of the solder disk is about 8 MS/m there is no need to use amplifiers to obtain the LFEIT signals. The ultrasound transducer (16 element linear phased array IMASONIC) is driven 1000 times by an Open System transducer driver with a 10 kHz burst signal. Each burst is composed of 3 periods of sinusoidal voltage signals (100 V_{pp} at 1 MHz). The resultant pressure amplitude is 500 kPa. The distance between the surface of the transducer and solder disk is about 45 mm. Since the

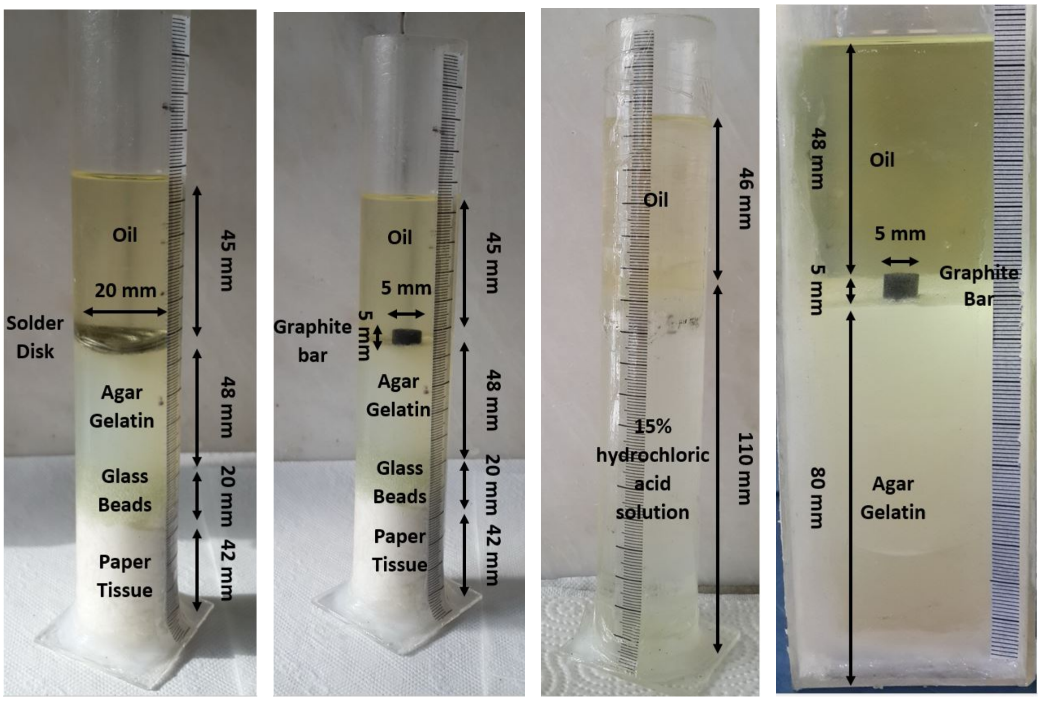

(a) (b) (c) (d)

Figure 5.7: Phantoms I, II, III and IV. (a) Phantom I including solder disk. (b) Phantom II including graphite bar. (c) Phantom III including oil and hydrochloric acid. (d) Phantom IV including one graphite bar at the center on the boundary.

sunflower oil's acoustic speed is 1453 m/s, acoustic wave is expected to reach to the interface at about 32 μs. The LFEIT signal is presented in Figure 5.9. The signal originating from the conductivity interface is starting at about 32 μs (by omitting 2 μs delay coming from the transducer). In Figure 5.9, from 2 to 6 μs, there are undesirable signals which are generated by the transducer when triggered by its driver.

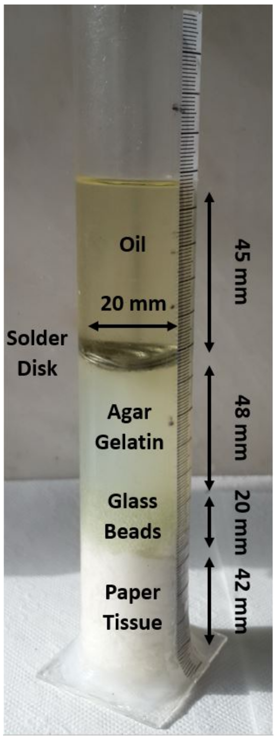

Figure 5.8: Solder disk Phantom I.

5.6 LFEIT Signal Measurement from Phantom II

In the second experiment, Phantom II is selected (Figure 5.10). Since, the conductivity of the graphite bar is between 800 and 3000 S/m, 52 dB amplification is applied to obtain the LFEIT signals. The ultrasound transducer (16 element linear phased array IMASONIC) is driven 1000 times by an Open System transducer driver with a 10 kHz burst signal. Each burst is composed of 3 periods of sinusoidal voltage signals (100 V_{pp} at 1 MHz). The resultant pressure amplitude is 500 kPa.

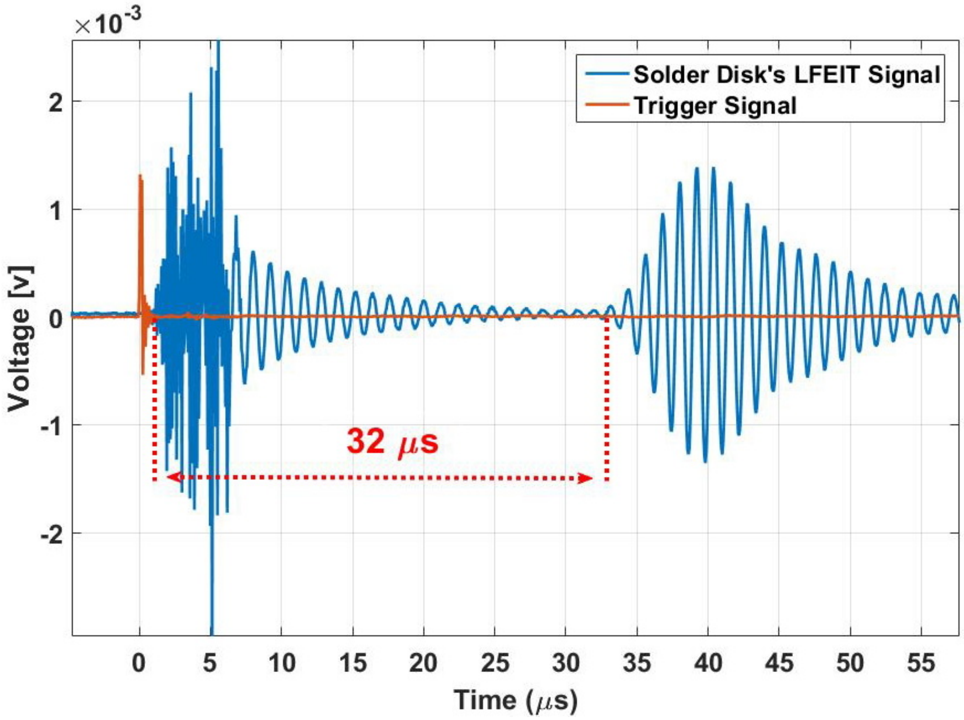

Figure 5.9: LFEIT signal from solder disk at 32 μs.

The distance between the surface of the transducer and graphite bar is about 45 mm. Acoustic wave is expected to reach to the interface at about 32 μs. The LFEIT signal is presented in Figure 5.11. The signal originating from the conductivity interface is starting at about 32 μs (by omitting 2 μs delay coming from the transducer).

5.7 LFEIT Signal Measurement from Phantom III

Considering the realized amplification circuit and coil sensors sensitivity, a minimum conductivity value of 70 S/m is detectable at this setup. For this reason, Phantom III is prepared (Figure 5.12). The ultrasound transducer (16 element linear phased array IMASONIC) is driven 1000 times by an Open System transducer driver with a 10 kHz burst signal. Each burst is composed of 5 periods of sinusoidal voltage signals (100 V_{pp} at 1 MHz). The resultant pressure amplitude is 500 kPa.

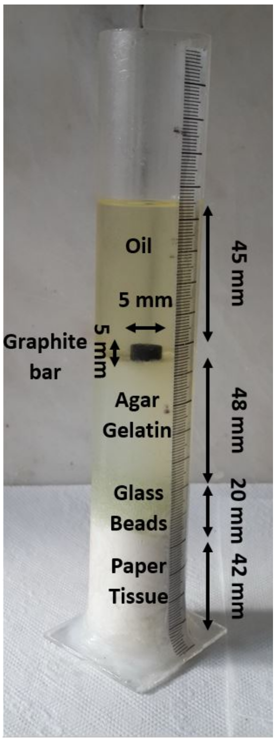

Figure 5.10: Graphite Phantom II.

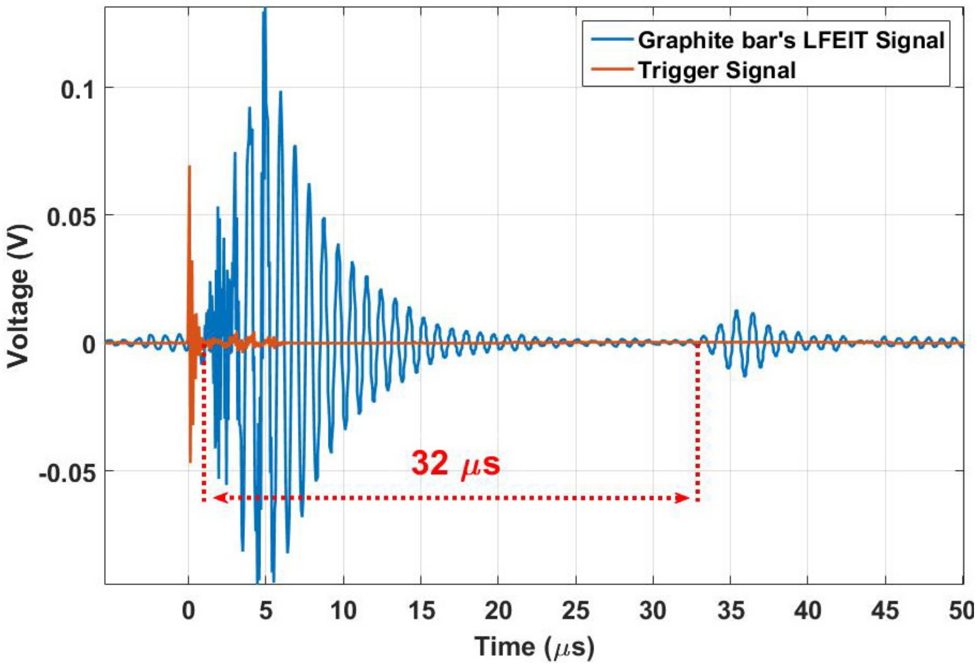

Figure 5.11: LFEIT signal from graphite bar at 32 μs.

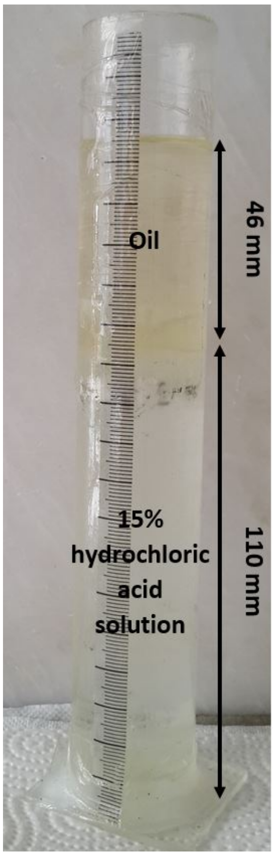

Figure 5.12: Sun flower oil (first layer from top) conductivity is about 0 S/m. Hydrochloric acid solution (second layer from top) conductivity is about 70 S/m.

The distance between the surface of the transducer and oil solution interface is about 46 mm. Acoustic wave is expected to reach to the interface at about 32 μs. The LFEIT signal after 100 dB amplification is presented in Figure 5.13. The signal originating from the conductivity interface is starting at about 32 μs (by omitting 2 μs delay coming from the transducer). In Figure 5.13, from 2 to 9.5 μs, there are undesirable signals which are generated by the transducer when triggered by its driver.

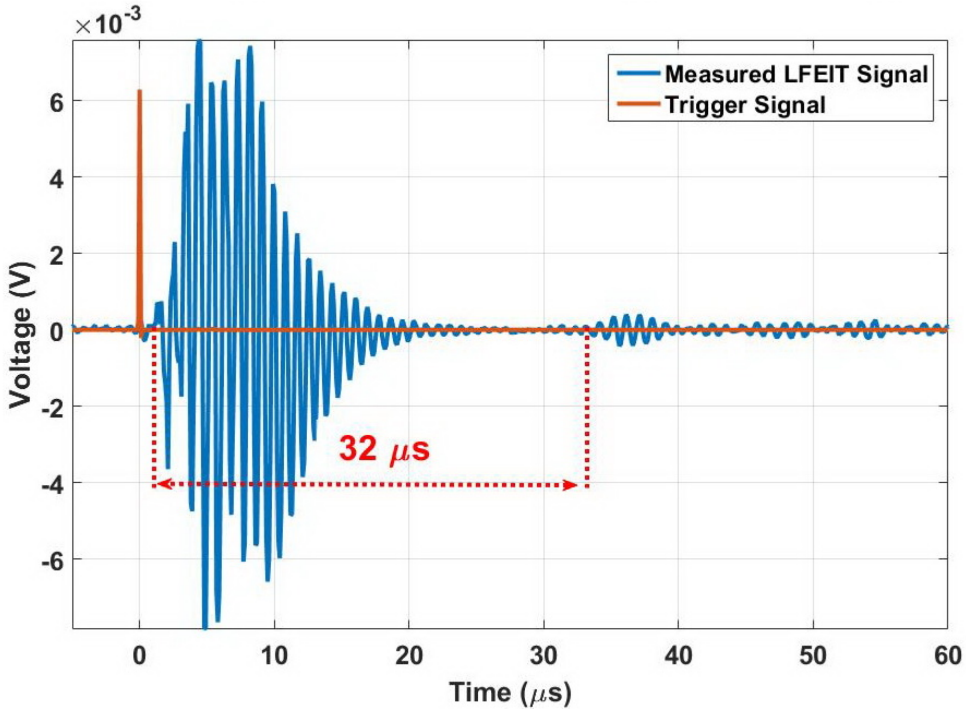

Figure 5.13: LFEIT signal $S(t)$ from oil-solution interface at 32 μs.

5.8 Fast Imaging of Measured LFEIT Signals

In the last section of experiments, Phantom IV (Figure 5.15) is selected. Acoustic pressure wavefront is steered from -20° to 20° by 1° step angle (there are 41 steps between -20° to 20°). At each step, the transducer is driven 8000 times with a 10 kHz burst signal (100 μs). That is, for each step 800 ms is required. Each burst has

5 periods of sinusoidal signals whose peak to peak voltage and frequency are 100 V_{pp} and 1 MHz, respectively. In addition, uploading data to the driver of the transducer takes 30 s. This property increases the scanning time. Once the excitation data is uploaded, the time required (t_s) to scan all specified angles is about:

$$t_s = 8000 \times 100 \times 10^{-6}\ s \times 41 = 32.8\ s$$

In order to make a smooth image, Hilbert transform of LFEIT signals ($H\{S(t)\}$) are taken. Then, absolute value of these data are calculated. The envelop of LFEIT signals are estimated by this method [46]:

$$\hat{S}(t) \triangleq S(t) + j \cdot H\{S(t)\} \tag{5.2}$$

$$\mathbb{S}(t) = Envelope\{S(t)\} = |\hat{S}(t)| = \left| S(t) + j\frac{1}{\pi}\int_{-\infty}^{+\infty} \frac{S(\tau)}{t-\tau} d\tau \right| \tag{5.3}$$

This procedure is applied on the LFEIT signals obtained from phantom IV at 0 $^\circ$ and presented in Figure 5.14.

The signals obtained for each angle, after 100 dB amplification, are displayed in column wise form using gray levels. In this way, an image is formed reflecting inhomogeneities in the body. Figure 5.16(a) shows the image of the graphite phantom obtained in this manner. It shows precisely the correct location and size of the inhomogeneity. Any blurring on the interfaces can be caused by a number of factors such as number of steering angles, measurement noise, envelope detection approach, coil sensitivity, unwanted wavefront collisions at angles near to the graphite bar, etc. The surface diameter of the graphite bar that is scanned by transducer is 5 mm. The graphite bar should approximately be detected at steering angles between -5 $^\circ$ to 1 $^\circ$ (6 $^\circ$).

In Figure 5.16(a), graphite bar's LFEIT signals are located at about the 36 μs (52.2 mm depth). Due to 2 μs delay in the transducer excitation, indeed the LFEIT signals

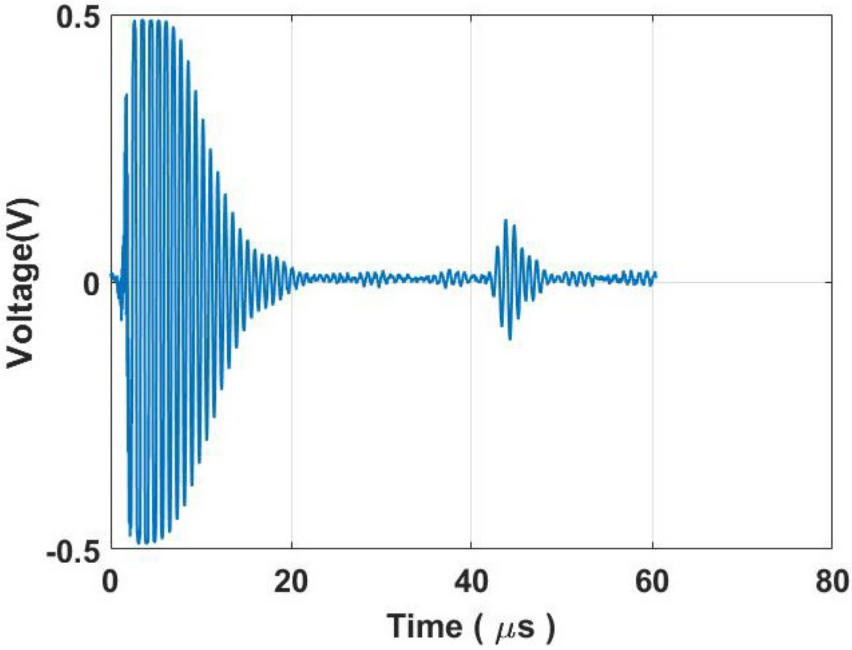

(a)

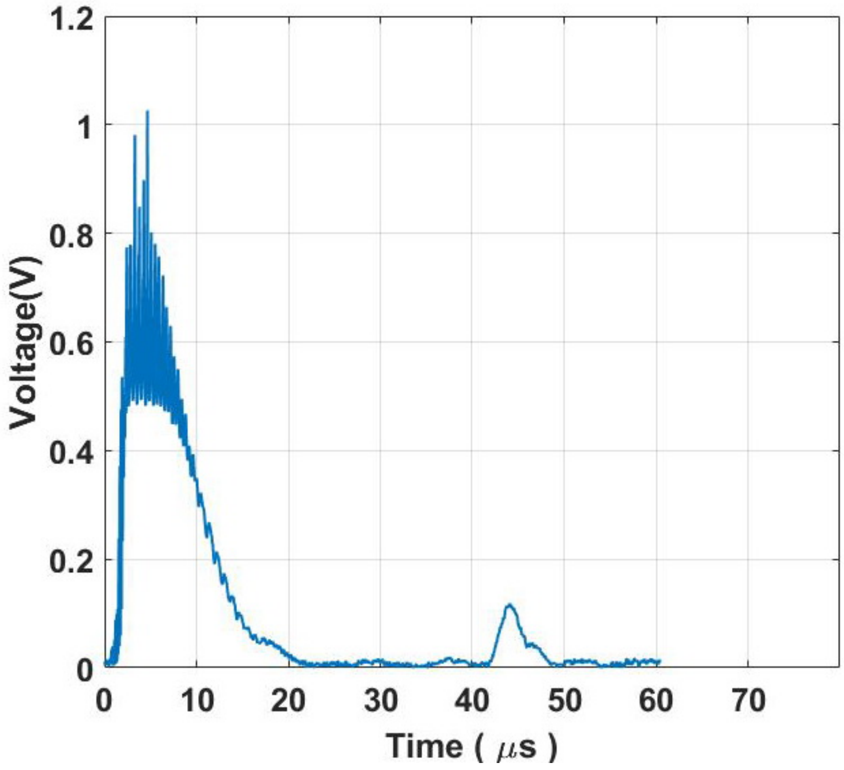

(b)

Figure 5.14: LFEIT signal from phantom IV at 0°. (a) LFEIT signal. (b) Hilbert transform of LFEIT signal.

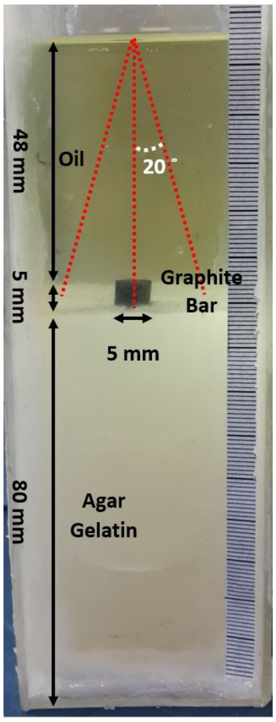

Figure 5.15: A graphite bar located at the center of phantom.

appeared at about 34 μs. That is, LFEIT signals are obtained approximately from 49.3 mm depth (2 $\mu s \times 1.45 \dfrac{mm}{\mu s} = 2.9\, mm$).

The LFEIT and B-scan ultrasound images in the polar coordinates are presented in Figures 5.17(a) and 5.17(b), respectively. In this figure, LFEIT and B-scan ultrasound signals corresponding each angle fills 1 degree space in polar coordinates. By placing signals at their corresponding degrees, Figures 5.17(a) and 5.17(b) are formed. As it presented in the figures, the LFEIT image generates comparable result in resolution to the B-scan ultrasound image.

LFEIT signals are obtained at 41 different angles. Twenty of recorded data are selected and presented in Figures 5.18 and 5.19. LFEIT signals are started and disappeared at about 5 ° and 16 °, respectively.

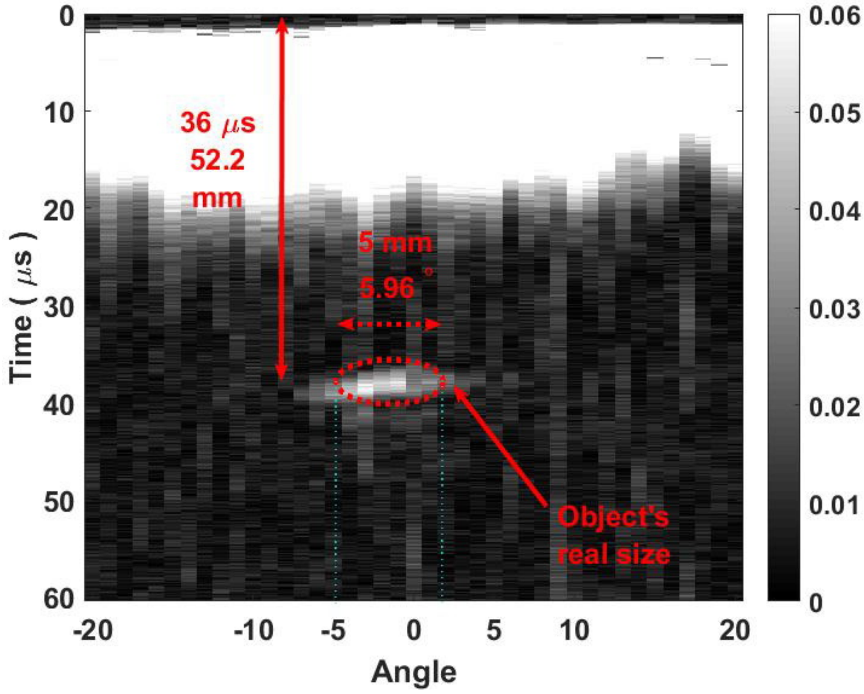

(a)

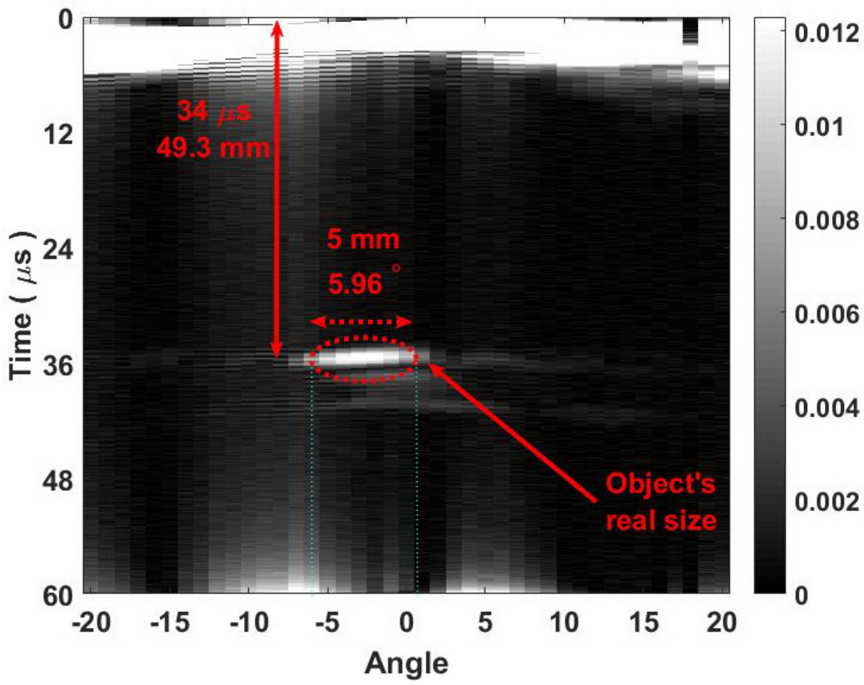

(b)

Figure 5.16: Imaging in polar coordinates. (a) LFEIT image obtained from Phantom IV. (b) Ultrasound image obtained from Phantom IV.

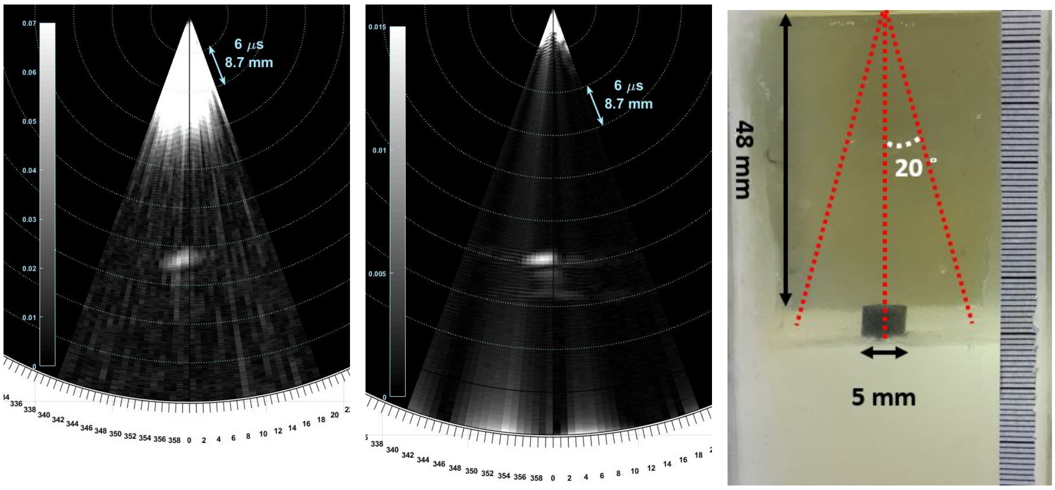

(a) (b) (c)

Figure 5.17: Imaging in polar coordinates. (a) LFEIT imaging in polar coordinates. (b) B-scan ultrasound imaging in polar coordinates. (c) Scan angle at the Phantom IV.

Conclusions:

- Ultrasound transducer steers acoustic wave front form -20 degree to 20 degree with 1 degree steps.
- Ultrasound transducer is adjusted to generate 8000, 5 periods, 1 MHz sinusoidal wave for each angle.
- In each angle, data acquisition card (DAQ card) takes average of 8000 received signals. Sample number of the signal is 6144 points.
- Each signal is placed on a column with respect to its angle accordingly. Hence a 2D matrix whose size is 6144 $\times$ 41 is obtained (column wise data profile).
- 2D polar coordinate data profiling is done by placing each signal to the related angle position.
- In both column wise and polar coordinate images, the white strip between -5 degree to 1 degrees at 36 μs represents graphite bar top surface. Actually, width of the white strip depends on width of the graphite bar.

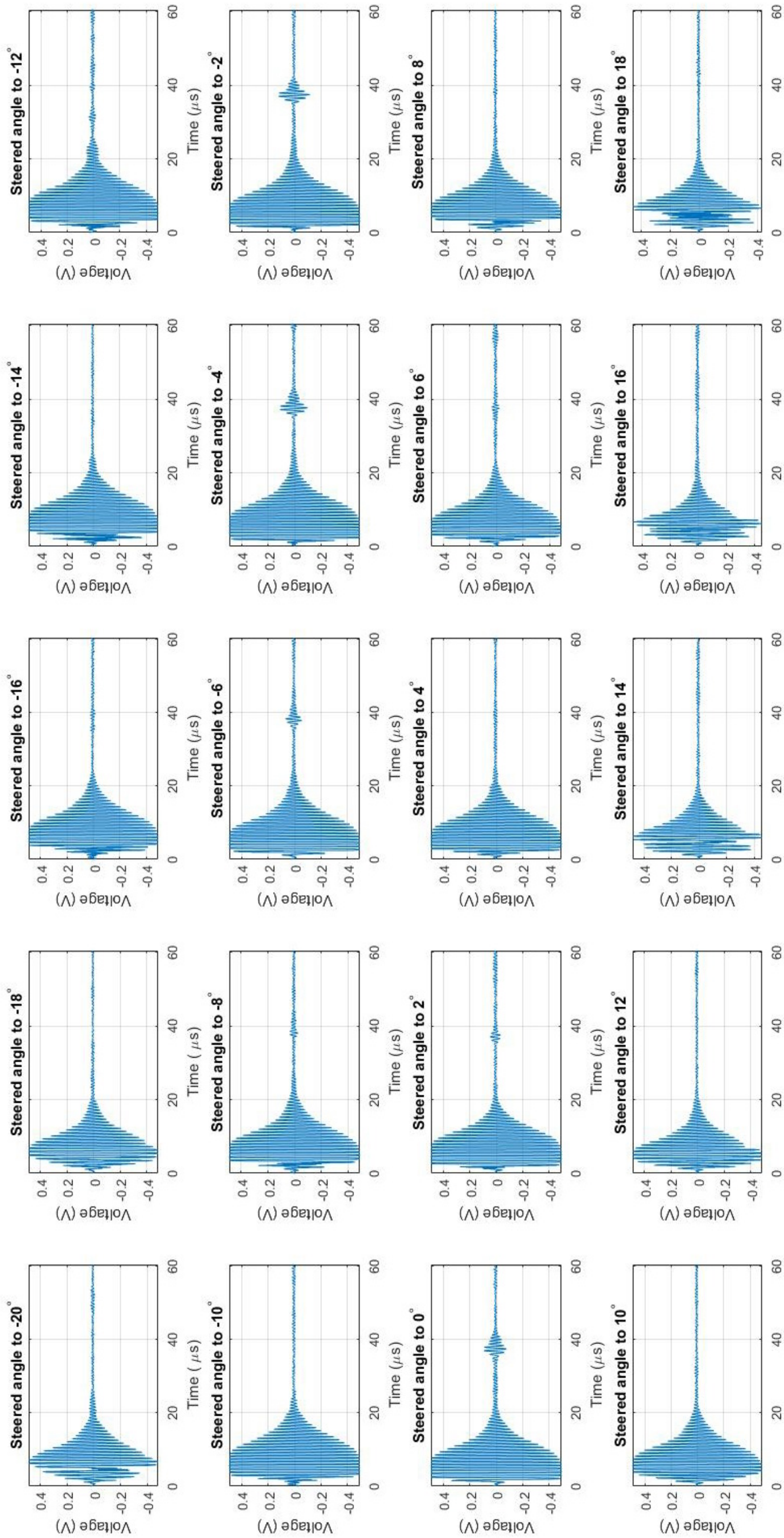

Figure 5.18: LFEIT signals at different angles.

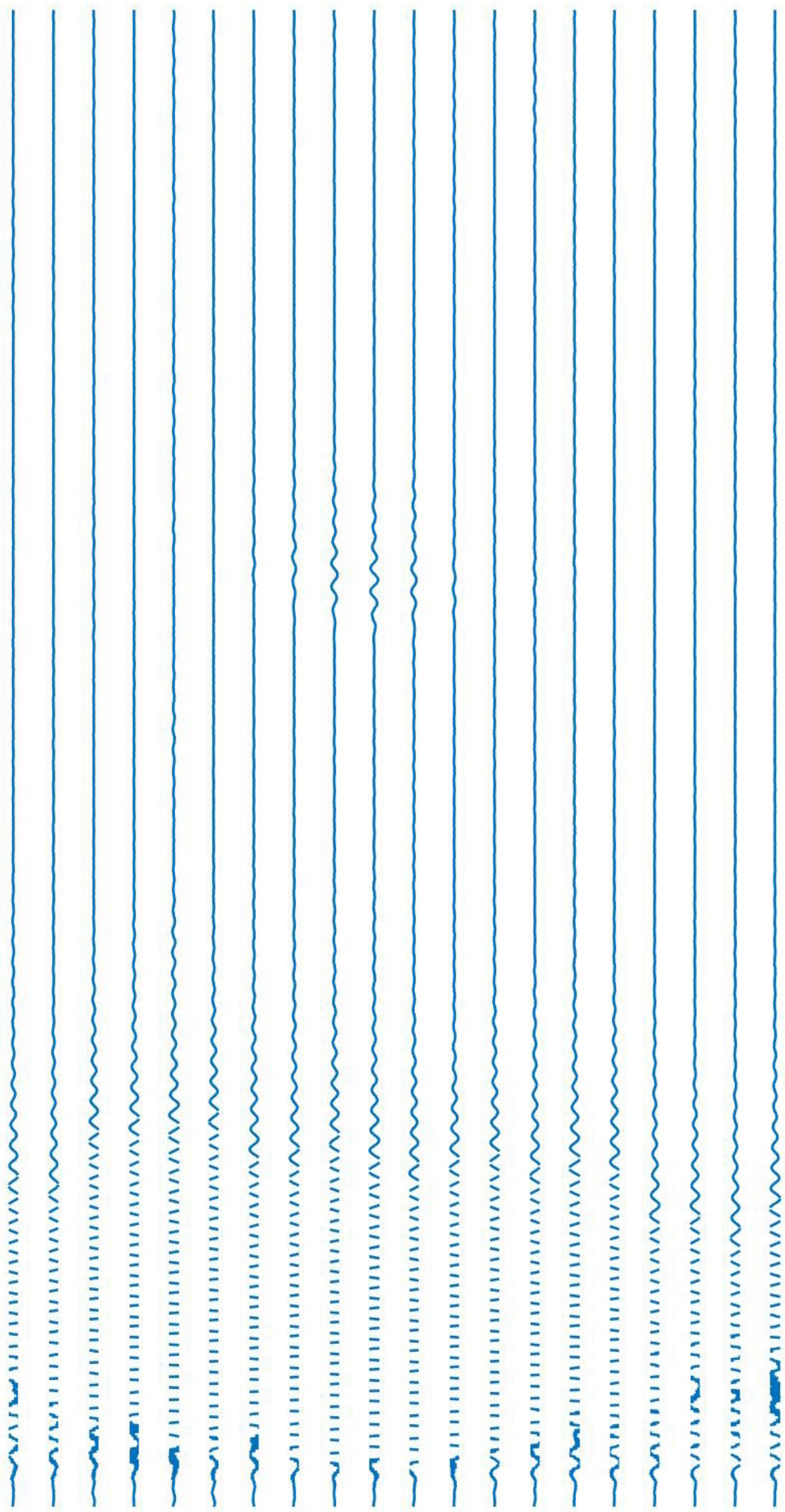

Figure 5.19: LFEIT signals at different angles.

- Depth of the white strip depends only on the number of periods transmitted by the transducer. In this image, depth of the white strip is 5 μs (compatible with transducer's excitation pulse number).

- In both LFEIT and B-scan images, bottom boundary of the graphite bar is not detected. Underlying reason is that the acoustic impedance of the graphite bar is much higher than the oil impedance and as a result, the acoustic wave is fully reflected from the top boundary of the graphite bar.

- During the excitation of the ultrasound transducer, piezoelectric crystals generate electromagnetic fields. Undesirable fields are picked up by the receiver coil sensor which causes information loss nearby the transducer.

- This work is pre-experimental study for the LFEIT project. At the next steps, gain of the amplifiers and input referred noise should be increased and decreased, respectively. In addition, quality factor of coil sensors must be optimized. Therefore, obtaining LFEIT signals from low conductivity phantoms will also be possible.

CHAPTER 6

CONCLUSIONS AND DISCUSSION

6.1 Summary and Conclusion

This thesis study is concentrated on the design of a data acquisition system to record LFEIT signals from the phantoms. The physical and electrical properties of disk multiple layer coil sensors were investigated by MATLAB simulations and experimental studies. A simulation environment is developed to design disk multiple-layer coil sensors. To measure LFEIT signals, resonance frequency of the receiver coil sensors are adjusted to the frequency of LFEIT signals.The accuracy of the magnetic field measurements by contactless sensors were found more than 90 $\%$ when the mean magnetic field strength is on the order of μT. In the experimental studies, to generate acoustic wavefront pressure, Open System transducer driver and 16 element linear phased array IMASONIC transducer were utilized. A static magnetic field of 0.56 T is generated using permanent magnets. A two stage cascaded amplifier with high input impedance and low input referred noise, was utilized. In addition, several phantoms with different conductivities were prepared. Finally, a prototype system is realized to measure LFEIT signals and the resultant data profiles were presented.

Using the experimental set up, LFEIT signals were detected from different phantoms by using coil sensors. By omitting the device artifacts (like transducer delay time after trigger signal), the inhomogeneity locations in the phantoms were correctly estimated. LFEIT signals of a phantom at a depth of 46 mm and whose conductivity was about 70 S/m were detected by the realized coil sensor.

The main advantage of the designed receiver coil sensors was the utilization of their resonance frequency. The contactless coil sensor's resonance frequency was adjusted to 1 MHz, same as the LFEIT signal's frequency. At the resonance frequency, their output voltage increased by coil sensor's quality factor (depending on number of $V_{Ind.}$ periods). In addition, in this method DC resistance of the sensors was decreased (because of few turn numbers in the wound coil sensor). This resistance was a noise source to the amplifier. The sensor was able to measure small range signals due to the improvement in the minimum detectable signal level.

In this study, the beam steering properties of linear phased array transducers are employed to steer acoustic wavefront pressures inside a phantom (from -20° to 20° by 1° step angle). For each of 41 angles, 8000 data are acquired and averaged. Therefore, average data acquisition time, scanning 41 different angles and recording 8000 data for each angle, is about 32.8 s. The data profile of the acquired signals was presented in section 5.8. By investigating the LFEIT generated images, it is observed that LFEIT provides images comparable in resolution to the ones generated by the ultrasound system.The LFEIT images show almost exact location, actual size and geometry of the objects. These images are presented for the first time in the literature.

6.2 Future Work

For the future studies, following schedule is proposed:

- Decreasing noise level of the system as much as possible in order to measure LFEIT signals with lower amplitude. This can be done by several methods such as optimizing the experimental system, using ultra low noise amplifiers, increasing amplifier's gain, using Faraday cage, etc.
- Designing optimized disk multiple layer coil sensors whose quality factor are high (narrow bandwidth).

- Designing differential receiver coils whose resonance frequency are same as LFEIT signal frequencies. With that configuration, common noise will be eliminated and SNR will be increased. Consequently, system's sensitivity to the variation of magnetic field density will be increased.
- Using at least two receiver coils in the x and y axes in order to improve LFEIT signal strength.
- Introducing a method to obtain a better estimate of the stray capacitance of disk multiple layer coils by using the physical properties of the coil.
- Optimizing the experimental system in order to obtain LFEIT signals from phantoms which mimic body tissues. In other words, doing simulations and experiments on tissue mimicking phantoms.
- Improving the static magnetic field strength.
- Applying various reconstruction techniques on the data profile of LFEIT signals to obtain enhanced images of phantoms.
- Decreasing data acquisition time as much as possible to obtain real time data profiles.
- Using time gated compensation (TGC) amplifiers.
- Implementing LFEIT experiments inside of an MRI device that has strong homogeneous static magnetic field.
- Development of the first portable LFEIT devices whose static magnetic field is mounted on the ultrasound transducer.

REFERENCES

[1] A. Ö. Tetik, E. Ghalichi, K. Kaboutari, and N. G. Gençer, "Design and assembly of a static magnetic field generator for lorentz field electrical impedance tomography," in *2016 20th National Biomedical Engineering Meeting (BIYOMUT)*, pp. 1–4, Nov 2016.

[2] D. Sheet, "Ultralow Noise VGAs with Preamplifier and Programmable R IN," 2016.

[3] A. Devices, "Dual VGA , Ultralow Noise Preamplifier , and Programmable R IN Evaluation Board," 2007.

[4] G. World Health Organization, "Breast cancer Fact Sheet." http://globocan.iarc.fr/Pages/fact_sheets_cancer.aspx, 2012. [Online; accessed 02 Jan. 2016].

[5] K. K. Shung, M. B. Smith, and B. M. Tsui, *Principles of Medical Imaging*.

[6] P. Suetens, *Fundamentals of Medical Imaging:*. Cambridge: Cambridge University Press, 2 ed., 008 2009.

[7] R. Zengin, "Electrical Impedance Tomography Using Lorentz Fields," Ph. D. Thesis, Dept. Electrical and Electronics Eng., METU, Ankara, Turkey, September 2012.

[8] H. Ammari and H. Kang, *Reconstruction of small inhomogeneities from boundary measurements*. Springer, 2004.

[9] L. F. Tanguay, H. Gagnon, and R. Guardo, "Comparison of applied and induced current electrical impedance tomography," *IEEE Transactions on Biomedical Engineering*, vol. 54, pp. 1643–1649, Sept 2007.

[10] K. Ö. Ozkan and N. G. Gencer, "Low-frequency magnetic subsurface imaging: Reconstructing conductivity images of biological tissues via magnetic measurements," *IEEE Transactions on Medical Imaging*, vol. 28, pp. 564–570, April 2009.

[11] B. U. Karbeyaz and N. G. Gencer, "Electrical conductivity imaging via contactless measurements: an experimental study," *IEEE Transactions on Medical Imaging*, vol. 22, pp. 627–635, May 2003.

[12] N. G. Gençer and M. N. Tek, "Forward problem solution for electrical conductivity imaging via contactless measurements," *Physics in medicine and biology*, vol. 44, no. 4, p. 927, 1999.

[13] H. Zhang and L. V. Wang, "Acousto-electric tomography," 2004.

[14] R. Xia, X. Li, and B. He*, "Comparison study of three different image reconstruction algorithms for mat-mi," *IEEE Transactions on Biomedical Engineering*, vol. 57, pp. 708–713, March 2010.

[15] H. Wen, J. Shah, and R. S. Balaban, "Hall effect imaging," *IEEE Transactions on Biomedical Engineering*, vol. 45, pp. 119–124, Jan 1998.

[16] R. Zengin and N. G. Gençer, "Lorentz force electrical impedance tomography using magnetic field measurements," *Physics in Medicine and Biology*, vol. 61, no. 16, p. 5887, 2016.

[17] L. Guo, G. Liu, and H. Xia, "Magneto-acousto-electrical tomography with magnetic induction for conductivity reconstruction," *IEEE Transactions on Biomedical Engineering*, vol. 62, pp. 2114–2124, Sept 2015.

[18] C. Xuan-Ze, M. Qing-Yu, Z. Feng, S. Xiao-Dong, and C. Hao-Chuan, "Theoretical studies on ultrasound induced hall voltage and its application in hall effect imaging," *Chinese Physics Letters*, vol. 29, no. 9, p. 097203, 2012.

[19] H. Wen, "Feasibility of biomedical applications of hall effect imaging," *Ultrasonic Imaging*, vol. 22, no. 2, pp. 123–136, 2000. PMID: 11061463.

[20] H. Wen, E. Bennett, J. Shah, and R. S. Balaban, "An imaging method using the interaction between ultrasound and magnetic field," in *Ultrasonics Symposium, 1997. Proceedings., 1997 IEEE*, vol. 2, pp. 1407–1410, IEEE, 1997.

[21] M. Soner Gözü, "2D Simulation Studies and Initial Experimental Results for Hall Effect Imaging," Master of Science Thesis, Dept. Electrical and Electronics Eng., METU, Ankara, Turkey, September 2014.

[22] M. Karadaş, "2D Simulations Based on the General Time Dependent Reciprocal Relation and Initial Experiments for LFEIT," M. Sc. Thesis, Dept. Electrical and Electronics Eng., METU, Ankara, Turkey, September 2014.

[23] T. Widlak and O. Scherzer, "Hybrid tomography for conductivity imaging," vol. 2, pp. 1–32, 2011.

[24] C. M. Falco and I. H. Schuller, "Squids and their sensitivity for geophysical applications," pp. 13–18, 1980.

[25] J. Clarke, *Squid Fundamentals, Fabrication and Applications*, pp. 1–62. Dordrecht: Springer Netherlands, 1996.

[26] T. Slawomir, "Induction coil sensors - a review," *Measurement Science and Technology*, vol. 18, no. 3, p. R31, 2007.

[27] W. Gopel, J. Hesse, and N. Zemel, "Sensors, A Comprehensive Survey, Volume 5, Magnetic Sensors," 1989.

[28] "P. Ripka, "Magnetic sensors and magnetometers", Artech House on Demand, 2001."

[29] a. Massarini, M. Kazimierczuk, and G. Grandi, "Lumped parameter models for single- and multiple-layer inductors," *PESC Record. 27th Annual IEEE Power Electronics Specialists Conference*, vol. 1, pp. 295–301, 1996.

[30] F. Ag, “Temperature coefficient of resistivity,” vol. 3.

[31] G. Grandi, M. K. Kazimierczuk, S. Member, A. Massarini, and U. Reggiani, “Stray Capacitances of Single-Layer Solenoid Air-Core Inductors,” vol. 35, no. 5, 1999.

[32] H. Wheeler, “Formulas for the Skin Effect,” *Proceedings of the IRE*, vol. 30, no. 9, pp. 299–311, 1942.

[33] A. Reatti and M. K. Kazimierczuk, “Comparison of various methods for calculating the AC resistance of inductors,” *IEEE Transactions on Magnetics*, vol. 38, no. 3, pp. 1512–1518, 2002.

[34] J. Ferreira, “Improved analytical modeling of conductive losses in magnetic components,” *IEEE Transactions on Power Electronics*, vol. 9, no. 1, pp. 127–131, 1994.

[35] G. N. Watson, *A treatise on the theory of Bessel functions*. Cambridge university press, 1995.

[36] H. Wheeler, “Simple Inductance Formulas for Radio Coils,” *Proceedings of the Institute of Radio Engineers*, vol. 16, no. 10, pp. 1398–1400, 1928.

[37] K. V. Cartwright and E. Joseph, “Finding the Exact Maximum Impedance Resonant Frequency of a Practical Parallel Resonant Circuit without Calculus,” vol. 11, no. 1, 2010.

[38] C. K. Alexander and M. N. O. Sadiku, *Fundamentals of Electric Circuits*.

[39] J. Choma, “Scattering Parameters : Concept , Theory , and Applications,” no. November 2002, 2009.

[40] N. Sokal and a.D. Sokal *IEEE Journal of Solid-State Circuits*, vol. 10, no. 3, pp. 168–176, 1975.

[41] D. Sheet, “Low Noise , Precision Operational Amplifier OP27 * Product Page Quick Links,” 2015.

[42] M. Slew and H. Low, “Low Noise , 1 GHz FastFET Op Amps,” 2016.

[43] C. J. Trujillo, A. Vera, and L. Leija, “An Agarose Based Phantom Embedded in an In Vitro Liver Tissue to Simulate Tumors : First Experience,” pp. 1–4.

[44] J. R. Cook, R. R. Bouchard, and S. Y. Emelianov, “Tissue-mimicking phantoms for photoacoustic and ultrasonic imaging,” vol. 2, no. 11, pp. 2243–2254, 2011.

[45] “THE ULTRASONIC PROPERTIES OF IMPREGNATED GR4F’HITE J. F. Muratore and H. R. Carleton College of Engineering and Applied Sciences State University of New York, Stony Brook, New York 11794,” pp. 940–944, 1981.

[46] H. Azhari, *Basics of Biomedical Ultrasound for Engineers*. A JOHN WILEY & SONS, INC., PUBLICATION, 2010.

[47] U. C. İnan, “Design and Implementation of Magnetic Field Sensors for Biomedical Applications,” METU, M.Sc. Thesis, February 2015.

[48] D. K. Cheng, *Field and Wave Electromagnetics*. Pearson Education, Limited, 2013.

APPENDIX A

SIMULATION PROGRAMS

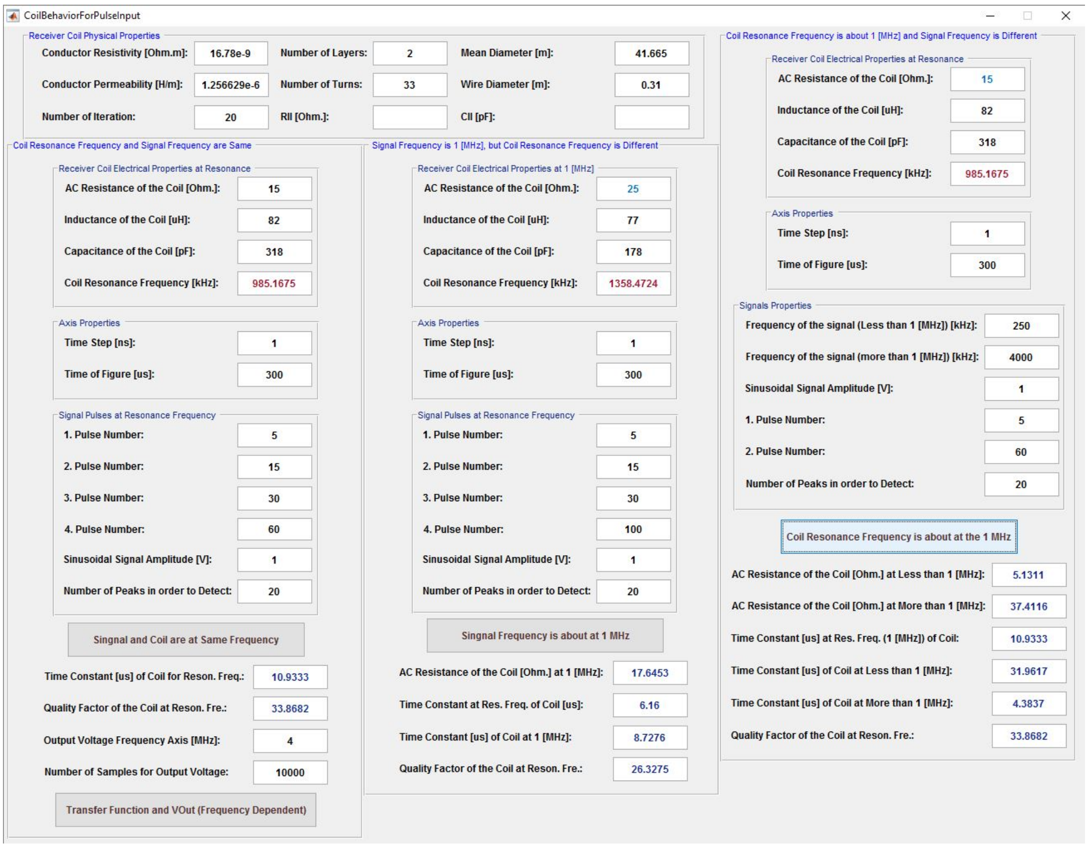

Figure A.1: Ringing effect simulation at the on and off resonance frequency for a receiver coil sensor.

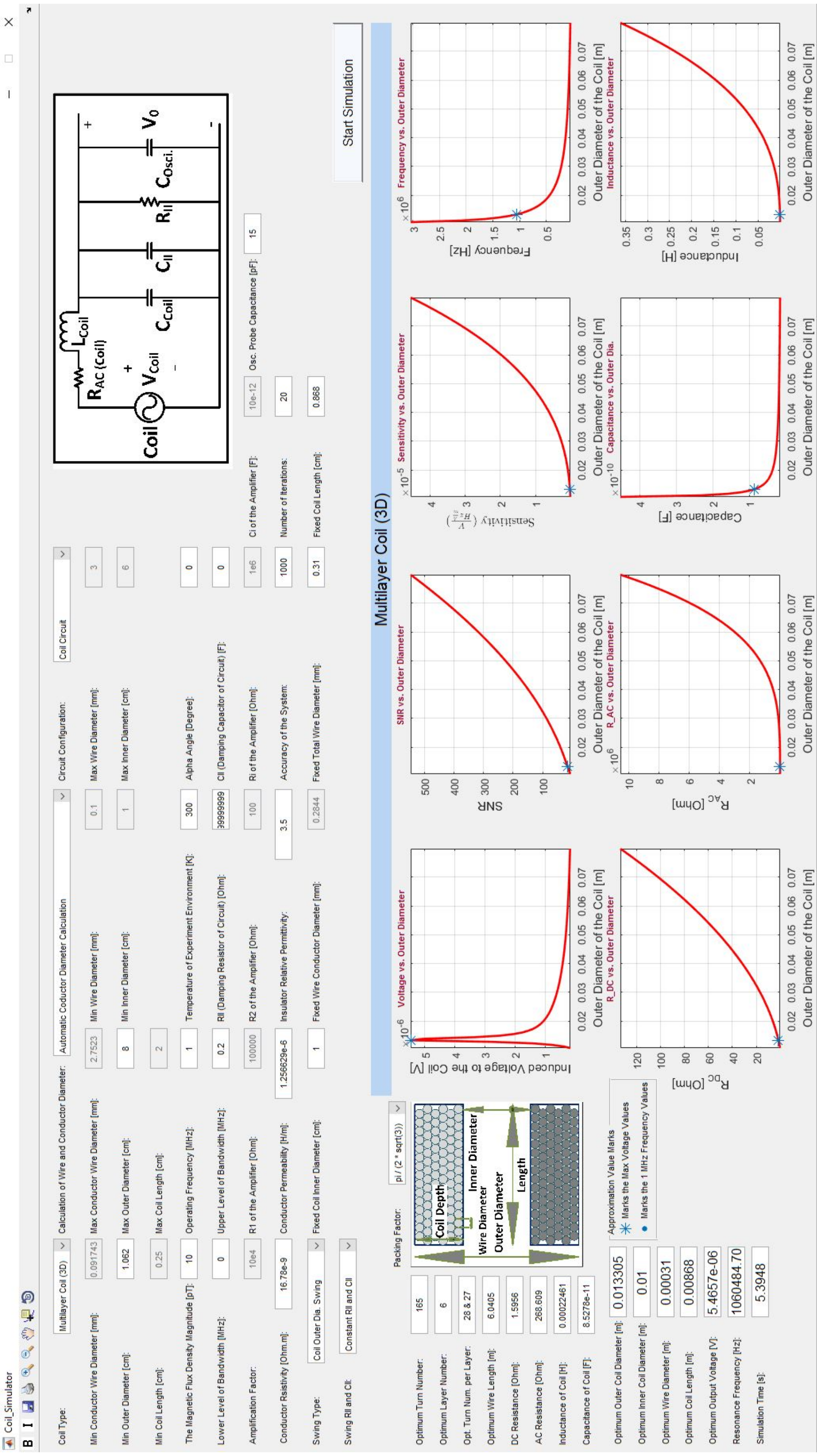

Figure A.2: Simulator of coil sensor's electrical properties.

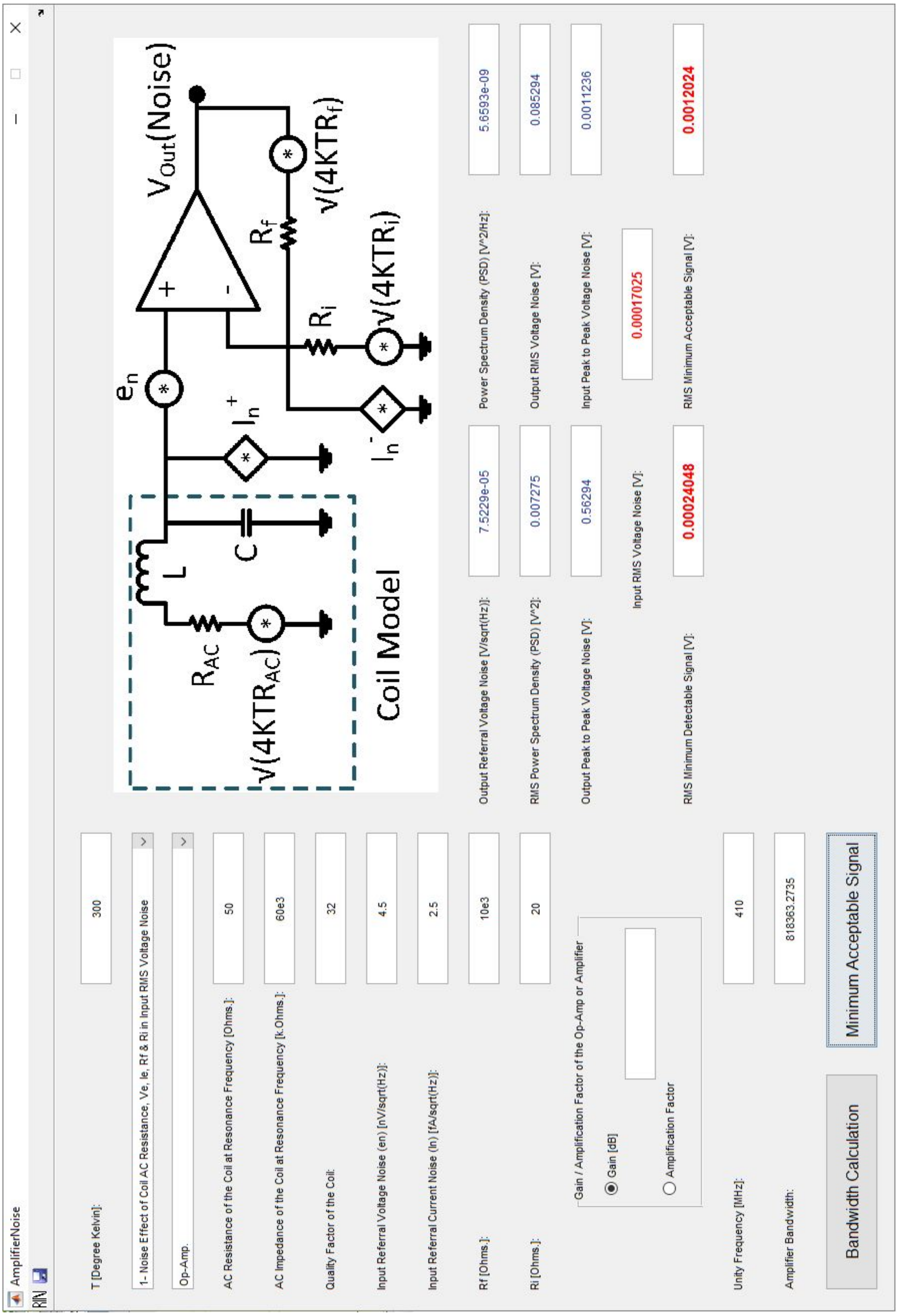

Figure A.3: Simulator of minimum detectable signal estimation at resonance frequency of a coil sensor.

Figure A.4: Simulator of coil sensor's electrical properties at resonance frequency.

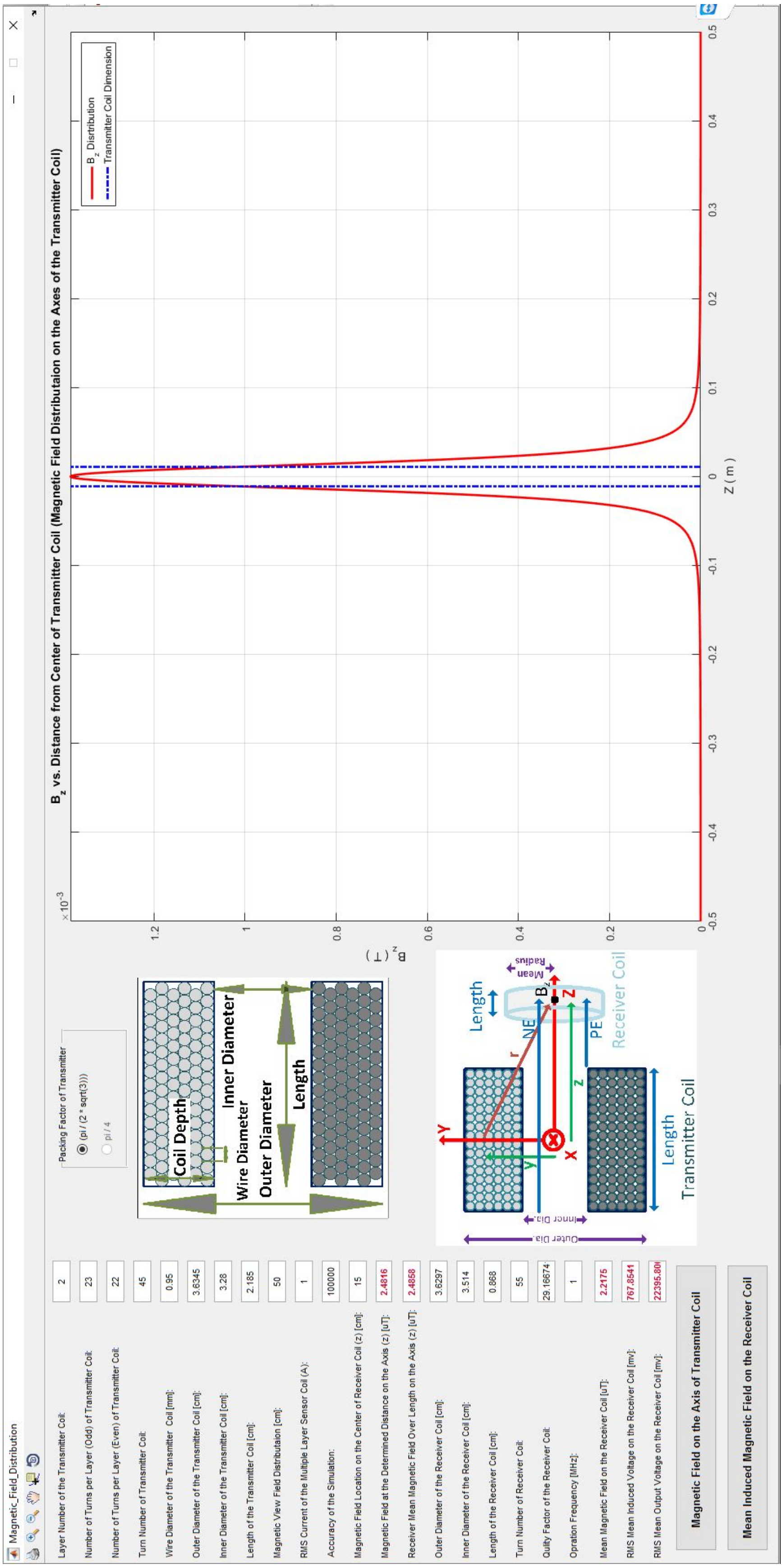

Figure A.5: Simulator of coil sensor's magnetic field distribution.

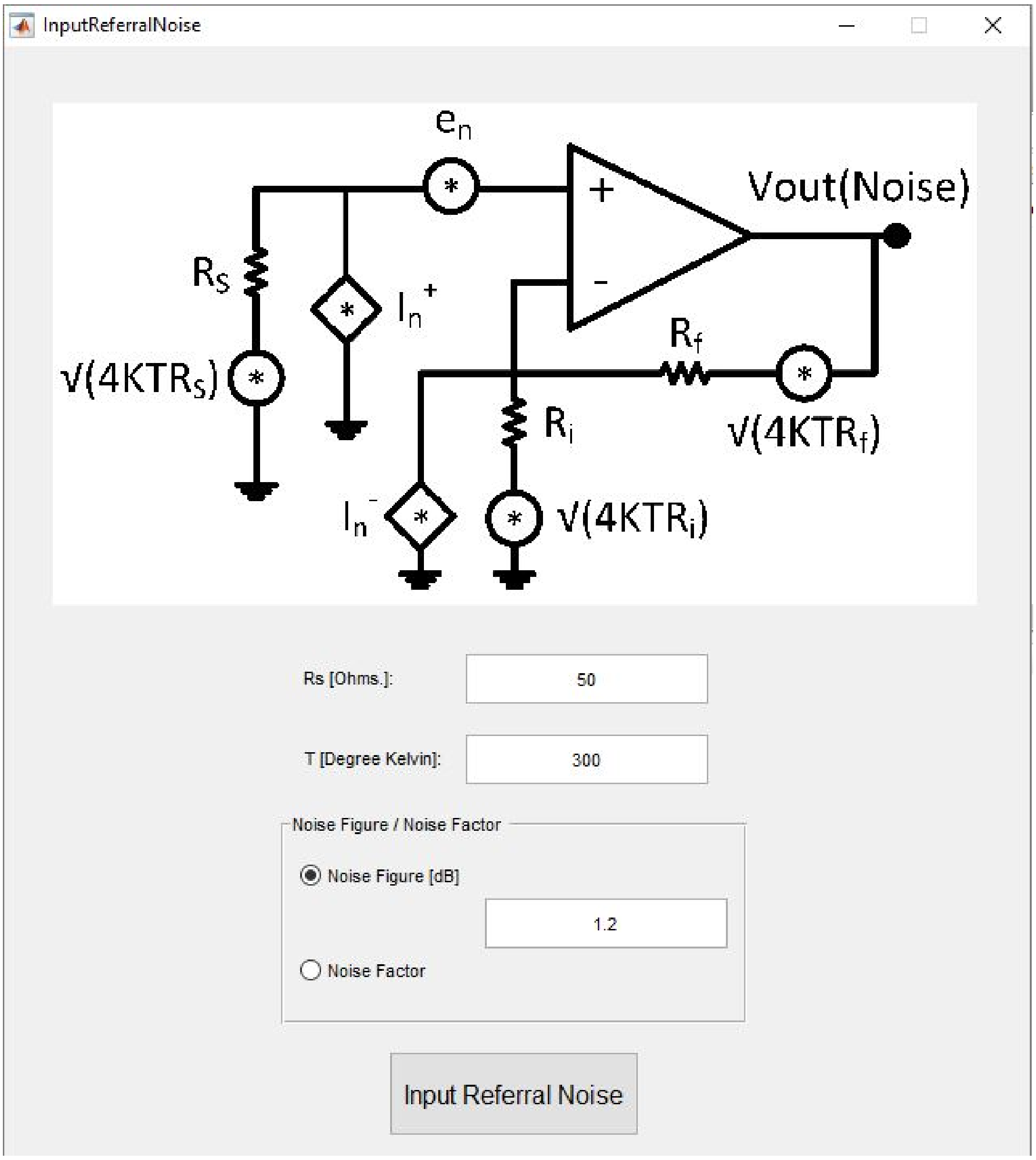

Figure A.6: Simulator of Op-Amp/Amplifier's input referred noise.

APPENDIX B

KELVIN'S FUNCTIONS

$J_\upsilon(x)$ is a bessel function of the first kind with the oreder of υ [35]:

$$J_\upsilon(\sqrt{i^3}x) = ber_\upsilon(x) + ibei_\upsilon(x)$$

$$J_0(\sqrt{i^3}x) = ber(x) + ibei(x)$$

$$J_\upsilon(x) = \left(\frac{x}{2}\right)^\upsilon \sum_{k=0}^{\infty} \frac{\left(\frac{-x^2}{4}\right)^k}{k!\Gamma(\upsilon + k + 1)}$$

$$\Gamma(\upsilon + k + 1) = (\upsilon + k)!$$

$$ber_\upsilon(x) = \Re(J_\upsilon(\sqrt{i^3}x)) = \left(\frac{x}{2}\right)^\upsilon \sum_{k=0}^{\infty} \frac{\frac{\cos[(\frac{3\upsilon}{4}+\frac{k}{2})\pi]}{4}}{k!\Gamma(\upsilon + k + 1)} \left(\frac{x^2}{4}\right)^k$$

$$bei_\upsilon(x) = \Im(J_\upsilon(\sqrt{i^3}x)) = \left(\frac{x}{2}\right)^\upsilon \sum_{k=0}^{\infty} \frac{\frac{\sin[(\frac{3\upsilon}{4}+\frac{k}{2})\pi]}{4}}{k!\Gamma(\upsilon + k + 1)} \left(\frac{x^2}{4}\right)^k$$

where $ber'_\upsilon(x)$ and $bei'_\upsilon(x)$ are first order derivative of $ber_\upsilon(x)$ and $bei_\upsilon(x)$, respectively.

APPENDIX C

MAGNETIC FLUX DENSITY ESTIMATION

In the LFEIT experiments, AC magnetic field is measured by coils sensors. To assess the accuracy in measurements, the measured AC magnetic field must be comparable to the true field value at particular locations. For this purpose, we shall assume a disk multiple layer transmitter coil with predetermined physical properties. Then one can estimate produced magnetic field by each turn of the supposed transmitter coil at the inside of a receiver coil with certain length and mean diameter (determinant volume). Sum of all magnetic fields give the mean magnetic field which receiver coil measures (Figure C.3).

C.1 The Magnetic Field on the Axis of a Disk Multiple Layer Coil

For the case of multiple layer coil (Figure C.1), the magnitude of magnetic field density along the coil axis can be calculated using the following formula [47]:

$$\begin{aligned} |\vec{B_z}| = \frac{\mu_0 \cdot TN \cdot I}{2(R - R_i)Len}(NE \cdot \ln(\frac{R + \sqrt{R^2 + NE^2}}{R_i + \sqrt{R_i^2 + NE^2}}) \\ -PE \cdot \ln(\frac{R + \sqrt{R^2 + PE^2}}{R_i + \sqrt{R_i^2 + PE^2}})) \end{aligned} \tag{C.1}$$

where R and R_i are the outer and inner coil radius, TN denotes the turn number, Len represents the coil length, I and μ_0 indicate the current and free space permeability, respectively. Here NE and PE denote the distance to field point from the distant edge and nearby edge of the coil (Figure C.1).

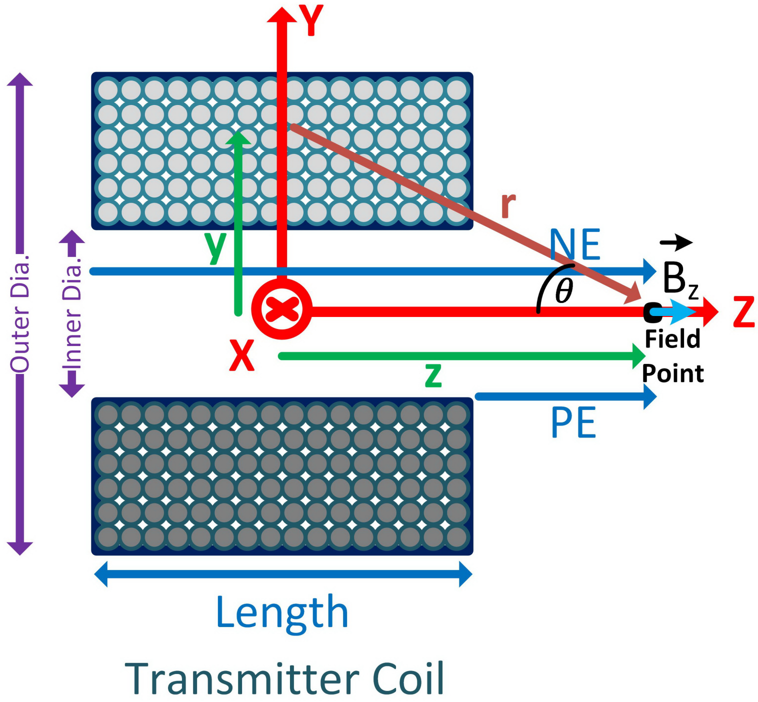

Figure C.1: Magnetic field on the axis of a multiple layer coil.

C.2 Method of Magnetic Field Estimation at the Inside of a Disk Multiple Layer Coil Sensor

As shown in Figures C.2 and C.3, centers of the current loop and surface S_1 are on the z axis while they are parallel to each other. The strength of magnetic field generated by a current loop on infinitesimal ring surface element dS_1 on surface S_1 is constant (equation C.2 [48]).

$$\vec{B} = \frac{\mu_0 I R^2}{4r'^3}(\frac{3}{2}\cos(2\theta) + \frac{1}{2})\vec{a_z} \tag{C.2}$$

Infinitesimal magnetic flux $d\phi_1$ is equal to multiplication of magnetic field by infinitesimal ring surface element dS_1. Total magnetic flux ϕ_1 is obtained by integrating $d\phi_1$ over surface S_1. Then, average magnetic field for S_1 is found by dividing total magnetic flux ϕ_1 to the surface S_1. For the multiple layer transmitter coil case which has n turns, one can estimate magnetic field on surface S_1 (inside the receiver coil) which is generated by each turn. Estimated total magnetic field over S_1 is sum of magnetic fields generated by all turns. The receiver coil in the z axis direction (receiver coil length) is divided to n surface elements (covert a volume to n infinitesimal surfaces). By taking average of the estimated magnetic fields for all surfaces, the mean magnetic field which receiver coil measures can be calculate.

In order to estimate the magnetic field inside a receiver coil with predetermined physical dimensions, it's necessary to note some facts and assumptions:

- Magnetic field of all points at x and y axes cancel out each other (except z axis direction).
- By increasing center to center distance between transmitter and receiver coils on the z axis, magnetic field is decreasing. Therefore, inside of the receiver coil, in the coil length direction, magnetic field is not constant.
- By increasing distance on the xy plane from center of the coil (on the mean radius of multiple layer coil sensor), the magnetic field starts to decrease. Therefore, magnetic field is not constant at the inside of receiver coil in the receiver coil radial direction.

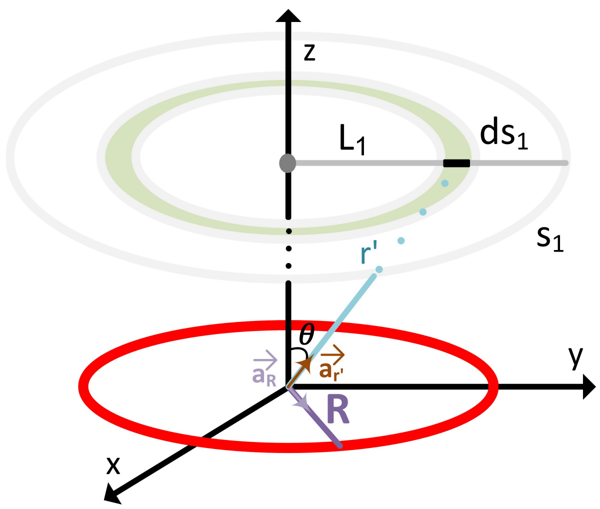

Figure C.2: Magnetic field at infinitesimal ring of a current loop.

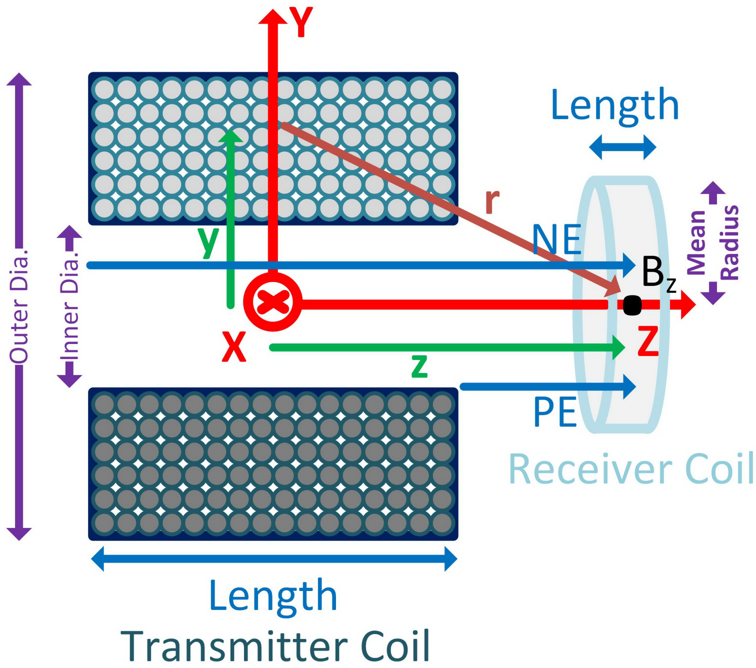

Figure C.3: Magnetic field inside a receiver coil generated by a disk multiple layer transmitter coil.

APPENDIX D

OP-AMP/AMPLIFIER'S NOISE CONNECTED TO THE COIL SENSORS

There are several noise sources that affect the input signals of the Op-Amp/amplifiers. Some of which are caused by the feedback's resistors, existent noise on the measured signals, self internal noise of the device itself and etc. In this section, the effect of each noise source on the Op-Amp/amplifiers will be investigated (Figure D.1).

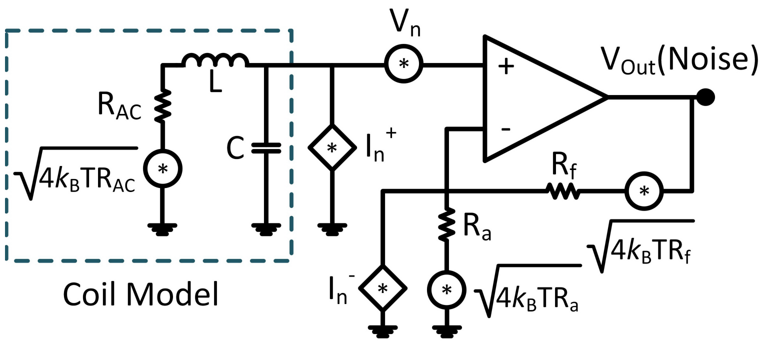

Figure D.1: Noise elements of amplification circuit.

For this case:

$$V^2_{In,Noise} = 4k_BT(R_a \parallel R_f) + {I_n^-}^2(R_a \parallel R_f)^2 + V_n^2 + {I_n^+}^2 Z^2 + 4k_BTR_{AC}Q \quad \text{(D.1)}$$

where Q is the quality factor of the coil sensor.

The following can be concluded from equation D.1:

- Effect of V_n to the noise is more dominant compared to I_n ($V_n^2 >> I_n^2$).
- R_{AC} and Q of the coil sensor have considerable effect on the noise.
- Effect of the coil sensor impedance Z to the noise is small (since I_n^+ is very small).
- Effect of R_a on the noise is bigger than that of R_f. But it is noteworthy to see that by changing one of them, gain and bandwidth of the Op-Amp/amplifier changes. Increasing gain or bandwidth of the Op-Amp/amplifier, increases noise at the output. Therefore, this relation is complicated to analyze.

Conference Publications:

1. Kaboutari K., Tetik A. Ö., Ghalichi E., Gözü M. S., Zengin R. and Gençer N. G., "An Experimental Study for Magneto-Acousto Electrical Impedance Tomography using Magnetic Field Measurements," 18th International Conference on Biomedical Applications of Electrical Impedance Tomography (accepted), 2017.

2. A. Ö. Tetik and E. Ghalichi and K. Kaboutari and N. G. Gençer, "Design and assembly of a static magnetic field generator for Lorentz Field Electrical Impedance Tomography," in 2016 20th National Biomedical Engineering Meeting (BIYOMUT), pp. 1-4, Nov 2016.

Grants:

2014: Research Grant and Scholarship: "Electrical Impedance Imaging Using Lorentz Fields and Magnetic Field Measurements," 114E184, Cost Action BM1309 (EMF-MED), The Scientific and Technological Research Council of Turkey (TÜBİTAK).